Imperial College of Science Technology and Medicine
Department of Electrical and Electronic Engineering
Optical and Semiconductor Devices Group

Investigation of passive electromagnetic components with metamaterials

by

Stergios Papantonis

Dipl.–Ing. Electrical and Computer Engineer

A dissertation submitted in partial fulfillment of the requirements for the degree of Doctor of Philosophy of Imperial College London and the Diploma of Imperial College London

June 2014

«Πέτρην κοιλαίνει ῥανὶς ὕδατος ἐνδελεχείη.»
Χοιρίλος ο Σάμιος – Επικός ποιητής (5ος αι. π.Χ.)

"A persistent drop of water bores in rock."
Choerilus of Samos – Epic poet (5th c. BC)

«Περὶ ἡδονάς γὰρ καὶ λύπας ἐστὶν ἡ ἠθικὴ ἀρετή· διὰ μὲν γὰρ τὴν ἡδονὴν πράττομεν τὰ φαῦλα, διὰ δὲ τὴν λύπην ἀπεχόμεθα τῶν καλῶν. Διὸ δεῖ ἦχθαί πως εὐθὺς ἐκ νέων, ὡς ὁ Πλάτων φησίν, ὥστε χαίρειν τε καὶ λυπεῖσθαι οἷς δεῖ· αὕτη γὰρ ἐστὶν ἡ ὀρθὴ παιδεία.»
Ἀριστοτέλης – Ἠθικὰ Νικομάχεια (4ος αι. π.Χ.)

"Moral excellence is concerned with pleasure and pain; because of pleasure we do bad things and for fear of pain we avoid noble ones. For this reason we ought to be trained from youth, as Plato says: to find pleasure and pain where we ought; this is the purpose of education."
Aristotle – Nicomachean Ethics (4th c. BC)

Copyright ©

The copyright of this thesis rests with the author and is made available under a Creative Commons Attribution Non-Commercial No Derivatives license. Researchers are free to copy, distribute or transmit the thesis on the condition that they attribute it, that they do not use it for commercial purposes and that they do not alter, transform or build upon it. For any reuse or redistribution, must make clear to others the license terms of this work.

Declaration of Originality

I hereby certify that I am the sole author of this dissertation and that, to the best of my knowledge, this thesis does not infringe upon any copyright or proprietary rights and any material from other resources that has been used is appropriately acknowledged.

Table of Contents

Acknowledgments xi
Abstract xiii
List of Figures xv
List of Tables xxi
List of Abbreviations xxiii

Chapter 1: Introduction **23**
1.1 Maxwell's Equations 23
1.2 Constitutive Equations 25
1.3 Models for the Polarization 26
1.4 Brillouin Zones 29
1.5 Surface Plasmon Polaritons 30
1.6 Metamaterials Applications 35
References 37

Chapter 2: The "Fakir's Bed of Nails" Metamaterial **39**
2.1 Introduction 39
2.2 Additional Boundary Conditions 42
2.3 Equivalent Surface Impedance 46
2.4 Applications 48
2.5 Conclusion 50
References 50

Chapter 3: Propagation Characteristics in Fakir's Bed of Nails Metamaterial Waveguides **57**
3.1 Introduction 57
3.2 Analytical Formulation 58
3.2.1 Plain Fakir's Bed of Nails 58
3.2.2 Fakir's Bed of Nails Parallel-Plate Waveguide 58
3.3 Transmission Line Model 66
3.4 Discussion and Conclusion 68

References . . . 68

Chapter 4: Coupling-induced Red-shifted Plasmonic Resonances on Infinite Chains of Nanopins 71

4.1 Introduction . . . 71
4.2 Description of the Structures and Numerical Approach . . . 72
4.3 Symmetry Considerations and Resonances . . . 73
4.4 Electric Field Patterns . . . 76
4.5 Explanation in Terms of Coupled Surface Plasmons . . . 77
4.6 Conclusion . . . 81
References . . . 81

Chapter 5: Reconfigurable Waveguide Components Using Metamaterials 85

5.1 Introduction . . . 85
5.2 Filter Design . . . 87
5.2.1 Band Pass Filter . . . 89
5.2.2 Band Stop Filter . . . 90
5.3 Manufactured Proof-of-Concept Demonstrators . . . 91
5.3.1 Band Pass Filter . . . 91
5.3.2 Band Stop Filter . . . 94
5.3.3 Single Resonator . . . 94
5.4 Extraction of Attenuation Constant . . . 96
5.5 Discussion . . . 97
5.6 Conclusion . . . 97
References . . . 97

Chapter 6: Reconfigurable "Voodoo" Waveguide for Single Element Vector Network Analyzer Verification 101

6.1 Introduction . . . 101
6.2 Reconfigurable Voodoo-Waveguide Structure . . . 102
6.3 Experimental Validation . . . 104
6.3.1 Dimensional Measurements . . . 104
6.3.2 Microwave Measurements Methodology . . . 105
6.3.3 Microwave Measurements . . . 106
6.3.4 Calibration Verification Proof-of-Concept . . . 109
6.4 WR-10 Waveguide Design . . . 110
6.5 Discussion and Conclusion . . . 110
References . . . 111

Chapter 7: Lossy Spherical Cavity Resonators for Stress-testing Eigenmode Solvers 115

7.1 Introduction 115
7.2 Analytical Formulation 116
7.3 Modeling Approaches Results and Discussion 120
7.3.1 Exact Analytical Results 120
7.3.2 Analytical Plane-wave Approximation 122
7.3.3 Plane-wave Approximation and FCB/LIB Results 123
7.3.4 Exact Analytical and IB Results 124
7.4 Equivalent Circuit Modeling 126
7.5 Conclusion 128
References 129

Chapter 8: Conclusions and Future Work **133**

Acknowledgments

I would like to thank my supervisors, Dr Stepan Lucyszyn and Prof. Ekaterina Shamonina for giving me the chance to work on such an interesting area. Their help and support are very much appreciated. Stepan's office door was always open and, when this was not possible, his instant response to e-mails made things easier. He was always there with numerous ideas for exploration and his multifaceted contributions made the time during this thesis very productive. Katya was also there to trigger new ideas and creative thinking and to make this journey as smooth as possible. She was always by my side and our discussions were valuable to me. My deepest gratitude goes to Nick M. Ridler from the UK's National Physical Laboratory (NPL). His contribution is manifold; from providing access to NPL's equipment (and being an excellent host) to suggesting new research avenues and being actively involved and hunting and providing funding for my work. Without his help and support, this work would not have been completed. Also, I would like to acknowledge the staff from level 1, namely, May Tang, Victor Boddy and Michael Harbour. They were more than happy to help, always with a big smile on their faces. Of course, a big thanks goes to all the people of the optical and semiconductor devices group and in particular, special thanks to Dr Oleksiy Sydoruk for many fruitful discussions and suggestions. Moreover, the 2012 ARFTG Student Fellowship Award and the Leverhulme Trust are gratefully acknowledged for partially funding this work.

Finally, and more importantly, my wholehearted gratitude goes to my family who were always supporting me, in all possible ways, in every step I took. Their contribution to this work may be behind the scenes but is truly invaluable; they made the realization of this work possible. Last, but not least, there are no words to express my thankfulness to Elpida. On the one hand, our long discussions and her comments were a great asset for this work to reach its current level. This work is as much mine as hers. On the other hand, she was on my side from start, with a remarkable ability to clear away even the most difficult moments. Her love and unconditional support made this experience very special.

Abstract

The main goal of this work is the design and analysis of passive components employing metamaterial structures and in particular the wire medium metamaterial. Although there has been a lot of research interest in the physics of such metamaterial structures, there are not many resources available describing the behaviour of classical components, such as waveguides and cavity resonators, that are formed by metamaterials. Therefore, the aforementioned widely used devices, are realized with the deployment of the "Fakirs bed of nails" and their performance is analyzed. Our motivation is to expand existing analytical models and their applications to commonly used passive electromagnetic components, with a view to explore potentially new applications. As a means of study analytical techniques together with numerical simulations and measurements were used. This thesis is structured in the following chapters.

The first chapter is an introduction to the basic principles of electromagnetics and their use on the framework of metamaterials; as illustrations some state of the art applications are presented.

The next chapter is a literature review covering the work that has been done in the area of our main research interest (i.e., the Fakir's bed of nails as a metamaterial). An overview of the mathematics describing its behaviour is given as well as applications of the proposed structure. Attention has been paid on the latest studies because they provide complete physical insight. Some results from this chapter are used later as background knowledge for the analysis of passive components. This chapter is intended to lay the foundations for the reader to continue reading the rest of this work without the need to look in the literature.

Chapter three investigates the dispersion effects in parallel-plate waveguides with both plates being realized by the Fakir's bed of nails. This chapter serves as an example as to how the Fakir's bed of nails can be used to form components. An analytical solution describing the behaviour of the waveguide is presented and compared against full wave numerical simulations.

Chapter four presents a theoretical study of the resonant behaviour of metallic nanorods. A clear analogy between the coupled rods and the split rings/split squares is shown. The decline in the resonant frequency as the gap decreases, previously described in terms of self-capacitance, is interpreted by surface plasmons coupled across the gap.

Chapter five presents a new enabling technology for implementing tunable rectangular waveguide components and circuits with the use of 2D and 3D metamaterials; a holey metal surface and wire media, respectively. As proof of concepts, results for tunable rectangular waveguide filters are presented with the use of pin block inductive irises and capacitive posts. Furthermore, by adapting the traditional metal-pipe rectangular waveguide for tunability, regions of the solid metal walls are replaced by holey metasurfaces. Prototype tunable structures were measured for verification and good agreement is achieved between full-wave numerical simulations and measurements.

Chapter six analyzes a radically new design of waveguide verification device, suitable for measuring instruments such as Vector Network Analyzers. The device is designed to enable its properties to be changed, by known amounts, after the device has been connected to the system that requires verification. The performance of the device is based on introducing relative changes in the transmitted and reflected signals and so is insensitive to errors introduced by waveguide flange imperfections. This makes the technique, in principle, ideally suited for waveguide VNAs operating at millimeter- and submillimeter-wave frequencies where these flange errors can dominate the measurements. A verification device is designed, simulated and tested in WR-15 waveguide (50–75 GHz).

The last part of this thesis presents a rigorous analysis of lossy spherical cavity resonators starting from first principles. The electromagnetic field inside the spherical cavity is expanded in normal waveguide modes and the eigenfrequencies of the cavity resonator are obtained analytically by enforcing the appropriate boundary conditions at the cavity wall. Unlike perturbation techniques,

used when low losses are present, there are no inherent limitations in the presented analysis and, therefore, its applicability range is much broader. Exact analytical results, acting as a benchmark reference standard, are compared to those generated independently by two commercial full-wave simulation software packages (HFSS^{TM} and COMSOL). When the wall transforms from being a perfect electrical conductor to free space, as its intrinsic conductivity decreases from infinity to zero, it is found that the eigenmode solvers with both software packages increasingly fail. With both software packages, all possible modeling strategies have been investigated and their associated limitations identified. Moreover, a plane-wave approximation model is proposed that accurately predicts the numerical simulation results.

List of Figures

1.1 An arbitrary volume in space as bound by a surface. 24
1.2 Boundary conditions for Maxwell's equations. 25
1.3 Oscillator model of the atom describing electronic polarization effects. 27
1.4 Construction of the Brillouin zones with a square lattice. (a) The periodic structure in the physical space (direct lattice) with primitive lattice vectors (**a**, **b**). (b) The first three Brillouin zones in the reciprocal space (**k**-space) and (c) the irreducible Brillouin zone. 30
1.5 Illustration of plane wave impinging at an interface between two media. The electric field orientation for both polarizations (TE and TM) is also shown. 31
1.6 Illustration of a TM polarized wave impinging on a slab. The field profiles at the interfaces are also shown. 32
1.7 Dispersion diagram for a 10 nm gold slab. The surface plasmon resonance is $\omega_{\mathrm{s}} = \frac{\omega_{\mathrm{p}}}{\sqrt{2}}$ is indicated with a dashed line and the dispersion curve for a single interface is also shown for comparison. 33
1.8 Two commonly used surface plasmon resonance excitation configurations. (a) Kretschmann-Raether configuration where the SPP is excited at the rear interface and (b) Otto configuration where the SPP is excited at the front interface. . . . 34
1.9 Amplitude of the reflection coefficient for a TM incoming wave. The total internal reflection angle θ_{c} and resonance angle θ_{r} are also indicated. 34
1.10 A weakly focused Gaussian beam impinging on a dielectric slab with (a) $\varepsilon_{\mathrm{r}} = -2$ and $\mu_{\mathrm{r}} = -1$ and (b) $\varepsilon_{\mathrm{r}} = 2$ and $\mu_{\mathrm{r}} = 1$. The direction of propagation can be determined by the left/right hand rule as shown at the top. 35
1.11 Superlens with sub-wavelength resolution realized by (a) a silver slab and (b) a stack of silver slabs. The thickness of the slab(s) is 10 nm. Poynting vector streamlines are also shown. 36
1.12 Electric field profile for the lens shown in Fig. 1.11(a). 36
1.13 A weakly focused Gaussian beam impinging on an invisibility cloak. (a) 2D view and (b) 3D view. The power flow is also shown with lines. 37

2.1 Geometry of the proposed Fakir's bed of nails. (a), Perspective view, (b) side view and (c) top view. It is formed by metallic pins arranged periodically in a square lattice (with periodicity a). They are embedded in a host dielectric substrate and their bottom ends are connected to a ground plane. 40
2.2 Geometry of a unit cell. The Fakir's bed of nails is periodic along the plane Ω_{T}. . . 44
2.3 Field distributions for a TM and TE polarized incoming wave. (a) H_x and (b) **E** distributions for TM polarization. (c) E_x and (d) **H** distributions for TE polarization. The parameters are: $r_0/a = 0.01$, $L = a$, $\theta = 45^{\circ}$ and $k_0 a = 1.05$. 46
2.4 Imaging device realized by the wire medium [31]. The field patterns correspond to the frequency at which highest resolution is obtained (30 THz). 49
2.5 Internal imaging using the Fakir's bed of nails. 49

2.6 The ridge gap parallel plate waveguide. (a) Perspective view and (b) fabricated prototype. The quasi-TEM mode is confined and propagates along the ridge. 49
2.7 Parallel-plate waveguide terminated with a thin layer of ε near zero material. (a) Power flow and (b) transmission (blue curve) and reflection (red curve) characteristics. 50

3.1 (a) Real part of k_z for the Fakir's bed of nails benchmark structure with $L = 7.5$ mm, $r_0 = 0.5$ mm and $a = 2$ mm. Solid lines: analytical model [9]. Discrete symbols: full-wave numerical simulation results obtained using HFSS™. The light line is plotted with a dashed line. (b) and (c) Electric field distributions at the pins for $k_z a = \pi$ in the first and second mode, respectively. (d) Electric field E_y at the center of the pins along the air gap. Blue curves correspond to the first mode and red curves to the second mode. 58
3.2 Fakir's bed of nails parallel-plate waveguide. (a) Perspective view and (b) side view. 59
3.3 Real part of k_z for $L = L_1 = L_2 = 7.5$ mm, $r_0 = 0.5$ mm $a = 2$ mm and and $h = 1$ mm. Solid lines: analytical model. Discrete symbols: full-wave numerical simulation results using CST MWS. The light line is plotted with a dashed line. Inset shows that the second mode has a small but non-zero group velocity. (b) and (c) Electric field distributions at the pins for $k_z a = \pi$ in the first and second mode, respectively. (d) Electric field E_y at the center of the pins along the air gap. Blue curves correspond to the first mode and red curves to the second mode. 62
3.4 Real part of k_z for $L_1 = 7.5$ mm, $L_1 = 2L_2$, $r_0 = 0.5$ mm, $a = 2$ mm and $h = 1$ mm. Solid lines: analytical model. Discrete symbols: full-wave numerical simulation results obtained using CST MWS. The light line is plotted with a dashed line. (b) and (c) Electric field distributions at the pins for $k_z a = \pi$ in the first and second mode,respectively. (d) Electric field E_y at the center of the pins along the air gap. Blue curves correspond to the first mode and red curves to the second mode. 62
3.5 Real part of k_z for the benchmark structure with $L_1 = 7.5$ mm, $L_2 = 0$, $r_0 = 0.5$ mm, $a = 2$ mm and $h = 1$ mm. Solid lines: analytical model [10]. Discrete symbols: full-wave numerical simulation results obtained using CST MWS. The light line is plotted with a dashed line. (b) and (c) Electric field distributions at the pins for $k_z a = \pi$ in the first and second mode, respectively. (d) Electric field E_y at the center of the pins along the air gap. Blue curves correspond to the first mode and red curves to the second mode. 63
3.6 Simulation setup for the (a) bed of nails with HFSS™ and (b) waveguide with CST MWS. The parameters used are: periodicity of the lattice $a = 2$ mm, air gap $h = 1$ mm and pin radius $r_0 = 0.5$ mm. 64
3.7 Real part of k_z for various (L_1,L_2) combinations when $L_1 + h + L_2 = 16$ mm. The rest of the parameters are given in Fig. 3.6. Lower and upper families of curves correspond to the first and second mode, respectively. 64
3.8 Real part of k_z for various gap sizes h when $L_1 = L_2 = 7.5$ mm. The rest of the parameters are given in Fig. 3.6. Lower and upper families of curves correspond to the first and second mode, respectively. 65
3.9 Real part of k_z for various gap sizes h when $L_1 = 2L_2 = 7.5$ mm. The rest of the parameters are given in Fig. 3.6. Lower and upper families of curves correspond to the first and second mode, respectively. 65
3.10 Real part of k_z for various gap sizes h when $t = h + 2L = 16$ mm. The rest of the parameters are given in Fig. 3.6. Lower and upper families of curves correspond to the first and second mode, respectively. 66

3.11 Real part of k_z for various radius sizes r_0/a when $L_1 = 2L_2 = 7.5$ mm. The rest of the parameters are given in Fig. 3.6. Lower and upper families of curves correspond to the first and second mode, respectively. 66
3.12 Equivalent transmission line model for the structure shown in Fig. 3.2 having both the top and bottom implemented using Fakir's bed of nails with arbitrary pin lengths. 67

4.1 The four nanostructures under study. (a) Split ring (SR), (b) split square (SS), (c) free pin (FP) and (d) infinite chain of coupled pins (CP). Possible symmetry planes for the electric field are also shown in red and gray. 73
4.2 Normalized electric field as a function of frequency for the various nanostructures. The structures have a gap of 10 nm and all of them have a total length of 270 nm. . 74
4.3 Comparison of the electric field patterns at the lowest resonance for the (a) SR, (b) SS, (c) FP and (d) CP. The field strength is plotted on a logarithmic scale normalized to the field maximum. 75
4.4 Comparison of the x and y components of the electric field distribution along the gap of the square structure with the gap of 30 nm (blue line) and along the coupled pin (red line). 76
4.5 Comparison of the resonant frequencies of the nanostructures with varying gap size. The structure length is always $\ell + g = 280$ nm. 77
4.6 Resonant frequency for the infinite chain of coupled nanopins with varying gap size. The resonance of the free pin is also shown with dashed line. The length of the structure is $\ell = 260$ nm. 78
4.7 Resonant frequency for the infinite chain of coupled nanopins with varying structure length. The resonance of the free pin is also shown for comparison. 79
4.8 Dispersion diagram for the infinite chain of coupled nanopins. The curves for a free pin, a slab and a single interface are also plotted as reference structures. 79
4.9 Normalized E_x field component along the chain of nanopins at (a) 820 THz and (b) 1049 THz. 80
4.10 Normalized frequency detuning for the first resonance for the infinite chain of coupled nanopins with varying length size. 80

5.1 Concept illustrations of tunable/reconfigurable waveguide components. (a) short-circuit tuning stub, (b) variable delay line, (c) programmable directional coupler, (d) programmable power splitter, (e) SP3T switch and (f) adjustable H-plane horn antenna. The red sections in (a) and (b) represent moveable pin block. The dashed lines in (c)-(f) represent possible post wall pin configurations. 86
5.2 Proposed filter geometry. (a) Perspective view and (b) plan view. 87
5.3 Numerical simulation results of transmission (blue curves) and reflection (red curves) power loss characteristics for a tunable filter using the parameters given in Table 5.1, having its center frequency tuned for (a) 8.4 GHz, (b) 9.2 GHz and (c) 10.6 GHz. 88
5.4 Ideal lumped-element equivalent circuit model for the 2-pole filter demonstrator. . . 88
5.5 (a) Numerical simulation results of normalized magnitude of E_y in the pass band at 9.2 GHz (solid curves) and outside the pass band at 9.5 GHz (dashed curves) and (b) corresponding contour plots of Ey in the pass band (top) and outside the pass band (bottom), respectively. 89
5.6 Numerical simulation results of transmission (blue curves) and reflection (red curves) power loss characteristics for various parametric studies. Thick lines correspond to the values shown in Table 5.1: (e) $d_1 = 5.17$ mm, $d_2 = 7.12$ mm and (f) $d_1 = 6.47$ mm, $d_2 = 8.42$ mm. 91

5.7 Left: Numerical simulation results of transmission (blue curves) and reflection (red curves) power loss characteristics for various penetration ratio values. Right: Cross-sectional view. 92
5.8 (a) Above: modified WR-90 dielectric filler (used as a temporary former) and below: flat 20×10 cm^2 perforated aluminum sheet (before assembly), (b) underside of the prototype filter (where the aluminum tape, protruding pins and standard WR-90 flanges can be seen) and (c) transverse view through the filter (showing the pin blocks and metasurfaces on all four walls running along the entire length of the 20 cm long rectangular waveguide). 92
5.9 Left: Chebyshev filter responses. Solid lines: measured results. Dashed lines: full-wave numerical simulation results using CST MWS. Right: individual pin arrangement with $L = L_1 = L_2 = 14.5$ mm. 93
5.10 Left: Butterworth filter responses. Solid lines: measured results. Dashed lines: full-wave numerical simulation results using CST MWS. Right: individual pin arrangement with $L = L_1 = L_2 = 14.8$ mm. 94
5.11 Left: Single capacitive post pin band stop filter responses. Solid lines: measured results. Dashed lines: full-wave numerical simulation results using CST MWS. Right: single pin having a penetration ratio $h/b = 0.59$ and 3.7 mm offset from center. . . . 94
5.12 Left: Cavity resonator insertion loss responses. Solid lines: measured results. Dashed lines: full-wave numerical simulation results using CST MWS. Right: pin arrangement with internal spatial dimensions of $a \times b \times L = 23 \times 10 \times 15.3$ mm^3. 95
5.13 Numerical simulation results of attenuation per guided wavelength in X-band for a conventional aluminum ($\sigma_0 = 3.56 \cdot 10^7$ S/m) WR-90 rectangular waveguide and one whose top wall is replaced by the proposed holey metasurface having dimensions given in Table 5.1. 96

6.1 Reconfigurable voodoo-waveguide structure. (a) Design plan view. The shaded areas represent the position of the holes (nominal dimensions are $L = 50$ mm, $d_1 = 1$ mm, $d_2 = 0.5$ mm, $\ell_1 = 1.5$ mm and $r = 0.25$ mm). (b) Machined structure with no pins inserted and (c) machined structure with two pins inserted all the way through. . . 103
6.2 Reflection (blue curve) and transmission (red curve) characteristics for the reconfigurable voodoo-waveguide structure with pins filling the holes (a) h_1 and h_2, and (b) h_1 and h_5. 104
6.3 Experimental setup for determining the hole positions. 105
6.4 Experimental setup for measuring the frequency response of the reconfigurable voodoo-waveguide structure. 106
6.5 Amplitude of reflection coefficient for various pins configurations. Solid lines represent the simulated response and dashed lines the measured response. 107
6.6 Amplitude of transmission coefficient for various pins configurations. Solid lines represent the simulated response and dashed lines the measured response. 107
6.7 Phase difference between numerical simulations and measurements of reflection coefficient for various pin configurations. 108
6.8 Phase difference between numerical simulations and measurements of transmission coefficient for various pin configurations. 108
6.9 Measured responses for a well-matched load standard (blue curve) and a poorly-matched load standard (red curve). 109

6.10 Reflection (blue curve) and transmission (red) characteristics when (a) a good SOLT calibration is performed and (b) when a poor SOLT calibration is performed (i.e., using an "ill-conditioned" matched load). The plots correspond to the case where h_1 and h_2 are filled with pins. 110
6.11 Illustration of the proposed WR-10 verification device. The shaded areas represent the position of the holes. The nominal dimensions are: $d_1 = d_2 = 750$ µm, $d_3 = 250$ µm, $d_4 = 650$ µm, $\ell = 750$ µm, $2r = 500$ µm 110
6.12 Reflection (blue curve) and transmission (red curve) response in the WR-10 waveguide band (75 to 110 GHz) when (a) h_2, (b) h_4 (c) h_1 and h_2 and (d) h_2 and h_3 are filled with pins. 111

7.1 Wave impedance for the fundamental TM_{011} mode for an air-filled spherical cavity having a 150 µm radius with various wall conductivities: (a) real part and (b) imaginary part. 120
7.2 (a) Eigenfrequency for the fundamental TM_{011} mode for an air-filled spherical cavity having a 150 µm radius and (b) associated unloaded quality factors. Solid lines: Exact analytical results. Discrete symbols: numerical results obtained from commercial full-wave solvers (circles: HFSS™ and stars: COMSOL). 120
7.3 Normalized field patterns for the TM_{011} mode for an air-filled spherical cavity having a 150 µm radius in the ideal case where $\sigma_0 \to \infty$. Electric field in (a) x-y, (b) x-z and (c) y-z plane. Magnetic field in (d) x-y, (e) x-z and (f) y-z plane. 121
7.4 Normalized field patterns for the TM_{011} mode for an air-filled spherical cavity having a 150 µm radius with $\sigma_0 = 100$ S/m. Electric field in (a) x-y, (b) x-z and (c) y-z plane. Magnetic field in (d) x-y, (e) x-z and (f) y-z plane. 121
7.5 Resonant frequency for the fundamental TM_{011} mode for an air-filled spherical cavity having a 150 µm radius using $Z_s = R_0(1+j)$. Solid lines: Analytical results. Discrete symbols: Numerical results obtained with a full-wave solver (circles: HFSS™ and stars: COMSOL). The results from perturbation method are also shown with dashed lines. 124
7.6 Percentage errors for eigenfrequencies using the FCB condition (circles: HFSS™ and stars: COMSOL). The error from perturbation method is also shown with dashed lines. 124
7.7 Resonant frequency for the fundamental TM_{011} mode for an air-filled spherical cavity having a 150 µm radius using $Z_s = R_s + jX_s$. Solid lines: Analytical results. Discrete symbols: Numerical results obtained with a full-wave solver (circles: HFSS™ and stars: COMSOL). The results from perturbation method are also shown with dashed lines. 125
7.8 Percentage errors for eigenfrequencies using the LIB condition (circles: HFSS™ and stars: COMSOL). The error from perturbation method is also shown with dashed lines. 125
7.9 Unloaded quality factor $Q_u(\omega_0')$ for the fundamental TM_{011} mode for an air-filled spherical cavity having a 150 µm radiususing $Z_s = R_0(1+j)$ (red) and $Z_s = R_s + jX_s$ (blue), respectively. Solid lines: Analytical results. Discrete symbols: Numerical results obtained with a full-wave solver (circles: HFSS™ and stars: COMSOL). The results from perturbation method are also shown with dashed lines. 126
7.10 Lumped element RLC equivalent circuit models for the fundamental TM_{011} mode. (a) Elementary resonant circuit with complex effective inductance and capacitance, (b) resonant circuit after replacing the complex effective components with equivalent real components, (c) driven RLC circuit and (d) undriven RLC circuit. 127

8.1 Fabricated cavity resonator realized by the Fakir's bed of nails. (a) Side view illustration, (b) a single cavity wall, (c) top view of the assembled resonator, (d) feeding probe of the cavity and (e) fully assembled resonator. 134
8.2 Measured return loss for the iron maiden cavity shown in Fig. 8.1. 135

List of Tables

4.1 Comparison of the resonant frequency of four different nanostructures. The structures have a total lenght of 270 nm and a gap of 10 nm. 74

5.1 Spatial dimensions (in mm) of the proposed filter corresponding to triangular lattice hole/pin positions. 89
5.2 Loaded and unloaded quality factors for the cavity shown in Fig. 5.12. 95

6.1 Hole locations (in mm) with respect to the origin of CS2. 105
6.2 Average error in reflection and transmission coefficients for good/poor calibration. . 109

7.1 Relaxation frequencies for various conducting wall materials at room temperature [16, 17] with the exact results. 122

List of Abbreviations

TM	Transverse Magnetic
TE	Transverse Electric
TEM	Transverse Electric and Magnetic
SPP	Surface Plasmon Polariton
ENZ	Epsilon Near Zero
TA	Transverse Average
MPRWG	Metal-Pipe Rectangular Waveguide
PEC	Perfect Electric Conductor
PMC	Perfect Magnetic Conductor
THz	Terahertz
HFSS	High Frequency Stucture Simulator
CST	Computer Simulation Technology
SR	Split-Ring
SS	Split-Square
FP	Free Pin
CP	Coupled Pins
MDM	Metal-Dielectric-Metal
SP3T	Single-Pole Three-Throw
VNA	Vector Network Analyzer
CMM	Coordinate Measuring Machine
UPMC	Universal Precision Measuring Machine
CS	Coordinate System
PNA	Performance Network Analyzer
TRL	Thru/Reflect/Line
SOLT	Short/Offset-short/Line/Thru
PIMMS	Primary Impedance Microwave Measurement System
NPL	National Physical Laboratory

Chapter 1

Introduction

In this thesis, the implementation of passive electromagnetic components with the use of the "Fakir's bed of nails" metamaterial is studied by means of analytical techniques, full-wave simulations and experimental verification. Existing analytical models are expanded to describe the behaviour of more complicated practical devices and potentially new applications are investigated with emphasis given on exploring the advantages of reconfigurable architectures.

Specifically, the dispersion effects in parallel-plate waveguides with both plates being realized by the Fakir's bed of nails are studied in detail. The proposed analytical model can be used as a starting point to describe more complicated components such as cavity resonators with bed of nails walls. Also, the response at optical frequencies of an infinite chain of nanopins (aligned along their axis) is described in terms of coupled surface plasmon polaritons. This structure can be regarded as a modification of the "Fakir's bed of nails" where the pins are aligned along their axis to form a 1D periodic structure. Furthermore, the implementation of reconfigurable waveguide components employing the "Fakir's bed of nails" is demonstrated with the realization of tunable waveguide filters and cavity resonators. Based on this approach, a new technique to verify waveguide measuring systems is proposed with the use of a single reconfigurable device. Finally, given the importance of full-wave simulation software, particularly for studying metamaterials, a stress-testing analysis of commercial solvers is undertaken with lossy spherical cavity resonators acting as benchmark reference structures.

In this chapter a brief overview of the basic electromagnetic theory is presented to enable an easier transition to the more advanced material presented in the main body of this thesis. As a result, little previous experience in this area is required. However, for a thorough analysis of these introductory concepts one has to study extensive literature. First, Maxwell's equations together with the constitutive equations are reviewed since they are the starting point for the electromagnetic analysis of all the structures presented in this work. Moreover, the electronic polarization associated with metals at optical frequencies is discussed. Next, an introduction to the Brillouin zones as a means to study periodic structures is presented followed by an analysis on surface plasmon polaritons where the dispersion characteristics of a metal slab are derived. Finally, some illustrative state-of-the-art practical applications are also presented to demonstrate how the aforementioned analytical models can be used to engineer structures with desired unusual electromagnetic properties.

1.1 Maxwell's Equations

The macroscopic electromagnetic behaviour of an arbitrary structure or system is described, as is well-known for over a century, by Maxwell's equations. The integral form of these equations,

following Minkowski's notation, can be written as

$$\left.\begin{aligned}
&\oint_{l(S)} \mathbf{E}\cdot d\mathbf{l} = -\frac{\partial}{\partial t}\iint_{S(l)} \mathbf{B}\cdot d\mathbf{S}\\
&\oint_{l(S)} \mathbf{H}\cdot d\mathbf{l} = -\iint_{S(l)} \left(\mathbf{J}_{\mathrm{f}} + \frac{\partial \mathbf{D}}{\partial t}\right)\cdot d\mathbf{S}\\
&\oiint_{S(V)} \mathbf{B}\cdot d\mathbf{S} = \iiint_{V(S)} \varrho^{\mathrm{m}}_{\mathrm{v,f}} dV\\
&\oiint_{S(V)} \mathbf{D}\cdot d\mathbf{S} = \iiint_{V(S)} \varrho^{\mathrm{e}}_{\mathrm{v,f}} dV
\end{aligned}\right\} \Longrightarrow \begin{aligned}
&\oint_{l(S)} \begin{bmatrix}\mathbf{E}\\ \mathbf{H}\end{bmatrix}\cdot d\mathbf{l} = \iint_{S(l)} \begin{bmatrix}-\dfrac{\partial \mathbf{B}}{\partial t}\\ \mathbf{J}_{\mathrm{f}} + \dfrac{\partial \mathbf{D}}{\partial t}\end{bmatrix} dV\\
&\oiint_{S(V)} \begin{bmatrix}\mathbf{B}\\ \mathbf{D}\end{bmatrix}\cdot d\mathbf{S} = \iiint_{V(S)} \begin{bmatrix}\varrho^{\mathrm{m}}_{\mathrm{v,f}}\\ \varrho^{\mathrm{e}}_{\mathrm{v,f}}\end{bmatrix} dV
\end{aligned} \tag{1.1}$$

where $\mathbf{E}$, $\mathbf{H}$, $\mathbf{D}$ and $\mathbf{B}$ are the electric field, magnetic field, electric flux density (displacement vector) and magnetic flux density, respectively. Moreover, $\varrho^{\mathrm{m}}_{\mathrm{v,f}}$, $\varrho^{\mathrm{e}}_{\mathrm{v,f}}$ and $\mathbf{J}_{\mathrm{f}}$ are the magnetic volume charge density, electric volume charge density and current density due to free charges, respectively. However, $\varrho^{\mathrm{m}}_{\mathrm{v,f}} = 0$ since there are not magnetic monopoles; this term helps restore symmetry in Maxwell's equations. Here, $V(S)$ and $S(V)$ represent a volume V bound by a surface S and vice versa, as shown in Fig. 1.1. It should be noted that the previous set of equations (1.1) is valid only when the boundaries are standing still (i.e., Gaussian surfaces) and describes the electromagnetic behaviour within spatial regions.

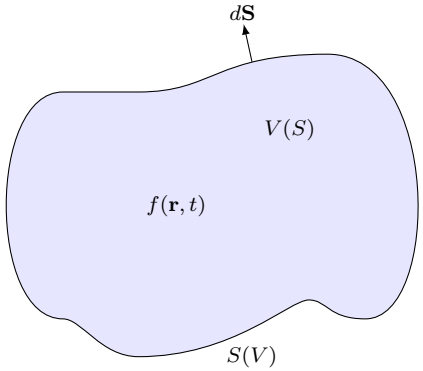


Figure 1.1: An arbitrary volume in space as bound by a surface.

However, in many cases it is convenient to solve differential equations instead of integral ones. Therefore, (1.1) can be written as

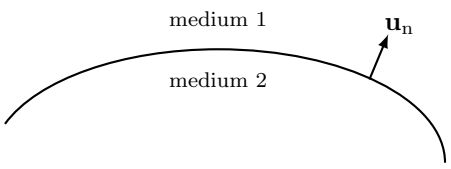
$$\nabla\times\mathbf{E} = -\frac{\partial \mathbf{B}}{\partial t} \tag{1.2}$$

$$\nabla\times\mathbf{H} = \mathbf{J}_{\mathrm{f}} + \frac{\partial \mathbf{D}}{\partial t} \tag{1.3}$$

$$\nabla\cdot\mathbf{B} = 0 \tag{1.4}$$

$$\nabla\cdot\mathbf{D} = \varrho^{\mathrm{e}}_{\mathrm{s,f}} \tag{1.5}$$

subject to the boundary conditions (1.6). In contrast to (1.1), (1.2)-(1.5) describe the electromagnetic behaviour at each point in space except for the points that lie on the boundaries. At the boundaries, the fields are given by the boundary conditions (1.6). The previous set of equations can be re-written



$$\begin{aligned}
&\mathbf{u}_\mathrm{n}\cdot\Big(\mathbf{D}_1-\mathbf{D}_2\Big)=\varrho_{\mathrm{s,f}}\\
&\mathbf{u}_\mathrm{n}\times\Big(\mathbf{E}_1-\mathbf{E}_2\Big)=0\\
&\mathbf{u}_\mathrm{n}\cdot\Big(\mathbf{B}_1-\mathbf{B}_2\Big)=0\\
&\mathbf{u}_\mathrm{n}\times\Big(\mathbf{H}_1-\mathbf{H}_2\Big)=\mathbf{J}_{\mathrm{s,f}}
\end{aligned}\tag{1.6}$$

Figure 1.2: Boundary conditions for Maxwell's equations.

so that the fields are formulated in terms of their free-space expressions (this is usually the preferred notation by physicists). However, before proceeding, some useful concepts have to be introduced first. For example, the polarization vector $\mathbf{P}$ describes the presence of matter whereas the electric field $\mathbf{E}$ is the field quantity that is induced by external (impressed) current sources and sources inside the medium. The same concept also holds for the magnetization vector $\mathbf{M}$ and the magnetic field $\mathbf{H}$. Thus, the polarization and magnetization vectors characterize an arbitrary medium. On the other hand, the displacement vector $\mathbf{D}$ and magnetic flux vector $\mathbf{B}$ are hybrid quantities that combine the presence of matter with the existence of any type of sources (external and internal). For non-singular charge distributions, after plugging the constitutive equations $\mathbf{D}=\varepsilon_0\mathbf{E}+\mathbf{P}$ and $\mathbf{B}=\mu_0\big(\mathbf{H}+\mathbf{M}\big)$ into (1.2)-(1.5), Maxwell's equations can be written in differential form as follows

$$\nabla\times\mathbf{E}=-\frac{\partial\mathbf{B}}{\partial t}\tag{1.7}$$

$$\nabla\times\mathbf{B}=\mu_0\left(\mathbf{J}_\mathrm{f}+\nabla\times\mathbf{M}+\varepsilon_0\frac{\partial\mathbf{E}}{\partial t}+\frac{\partial\mathbf{P}}{\partial t}\right)\tag{1.8}$$

$$\nabla\cdot\mathbf{B}=0\tag{1.9}$$

$$\nabla\cdot\mathbf{E}=\frac{\varrho^{\mathrm{e}}_{\mathrm{v,f}}}{\varepsilon_0}-\frac{\nabla\cdot\mathbf{P}}{\varepsilon_0}\tag{1.10}$$

1.2 Constitutive Equations

Maxwell's equations consist a set of eight equations; two vector and two scalar equations. Given that $\mathbf{J}_\mathrm{f}$ and $\varrho^{\mathrm{e}}_{\mathrm{v,f}}$ are related to each other with the equation of charge conservation $\oiint_S\mathbf{J}_\mathrm{f}\cdot d\mathbf{S}+\iiint_{V(S)}\frac{\partial\varrho^{\mathrm{e}}_{\mathrm{v,f}}}{\partial t}dV=0$ (which is external to Maxwell's equations i.e., it describes a different physical law), the number of the independent equations is reduced by one. Furthermore, Gauss law for the magnetic field can be derived from Faraday's law, thus there are six independent equations relating twelve field quantities (i.e., $\mathbf{E}$, $\mathbf{D}$, $\mathbf{H}$ and $\mathbf{B}$) to each other. Hence, six more equations are needed in order to solve Maxwell's equations unambiguously. These equations, whenever is possible to be expressed in closed form, are referred to as constitutive equations. However, it should be underlined that the quantities $\mathbf{J}_\mathrm{f}$ and $\varrho^{\mathrm{e}}_{\mathrm{v,f}}$ are external to Maxwell's equations which means the they require an additional physical model on top of Maxwell's equations in order to be calculated.

The constitutive equations must obey the principal of causality since they describe natural media. This means that there is a delay between the cause and its effect. In our case, we assume that the fields $\mathbf{E}$ and $\mathbf{H}$ are causing the polarization and magnetization effects, respectively. For

example, the polarization can be expressed by the following convolution integrals

$$\begin{aligned}\mathbf{P}_i(\mathbf{r},t) =&\varepsilon_0 \sum_{j=1}^{3} \int_V \int_{-\infty}^{t} \bar{\bar{\chi}}_{ij}^{(1)}(\mathbf{r}',t';\mathbf{r},t)E_j(\mathbf{r}',t')dV'dt'+\\ &\varepsilon_0 \sum_{j=1}^{3}\sum_{k=1}^{3} \int_V \int_V \int_{-\infty}^{t} \int_{-\infty}^{t} \bar{\bar{\chi}}_{ijk}^{(2)}(\mathbf{r}'',t'';\mathbf{r}',t';\mathbf{r},t)E_j(\mathbf{r}'',t'')E_k(\mathbf{r}',t')dV'dV''dt'dt''+\\ &\cdots\end{aligned} \tag{1.11}$$

where $i=(j,k,l)$ represents the axis of the coordinate system. As can been seen the relationship between $\mathbf{P}$ and $\mathbf{E}$ does not have to be linear necessarily. In (1.11) the spatial integration is over the entire volume occupied by the material whereas the temporal integration is over all past times (i.e., $t \leqslant t'$) which reflects hysterisis phenomena between $\mathbf{P}$ and $\mathbf{E}$. It is interesting to note that the dyadic (second order tensor) $\bar{\bar{\chi}}^{(1)}$ is a 3×3 matrix which means that different components of the electric field have a different effect on each component of the polarization. Similarly, for the magnetization one can write a relationship of the form

$$\begin{aligned}\mathbf{M}_i(\mathbf{r},t) =&\mu_0 \sum_{j=1}^{3} \int_V \int_{-\infty}^{t} \bar{\bar{\chi}}_{\mathrm{m}_{ij}}^{(1)}(\mathbf{r}',t';\mathbf{r},t)H_j(\mathbf{r}',t')dV'dt'+\\ &\mu_0 \sum_{j=1}^{3}\sum_{k=1}^{3} \int_V \int_V \int_{-\infty}^{t} \int_{-\infty}^{t} \bar{\bar{\chi}}_{\mathrm{m}_{ijk}}^{(2)}(\mathbf{r}'',t'';\mathbf{r}',t';\mathbf{r},t)H_j(\mathbf{r}'',t'')H_k(\mathbf{r}',t')dV'dV''dt'dt''+\\ &\cdots\end{aligned} \tag{1.12}$$

which is the dual relationship of (1.11). As a result, the constitutive equations can be written as

$$\mathbf{D}=\varepsilon_0\mathbf{E}+\mathbf{P}=\bar{\bar{\varepsilon}}*\mathbf{E}\equiv\bar{\bar{\varepsilon}}_{\mathrm{L}}*\mathbf{E}+\mathbf{N}(\mathbf{E})\equiv\varepsilon_0\left(\bar{\bar{I}}+\bar{\bar{\chi}}^{(1)}*\right)\mathbf{E}+\mathbf{N}(\mathbf{E})\equiv\varepsilon_0\bar{\bar{\varepsilon}}_{\mathrm{r}}*\mathbf{E}+\mathbf{N}(\mathbf{E}) \tag{1.13}$$

$$\mathbf{B}=\mu_0(\mathbf{H}+\mathbf{M})\bar{\bar{\mu}}*\mathbf{H}\equiv\bar{\bar{\mu}}_{\mathrm{L}}*\mathbf{H}+\mathbf{N}(\mathbf{H})\equiv\mu_0\left(\bar{\bar{I}}+\bar{\bar{\chi}}_{\mathrm{m}}^{(1)}*\right)\mathbf{H}+\mathbf{N}(\mathbf{H})\equiv\mu_0\bar{\bar{\mu}}_{\mathrm{r}}\mathbf{H}+\mathbf{N}(\mathbf{H}) \tag{1.14}$$

where $\mathbf{N}(\mathbf{E})$ and $\mathbf{N}(\mathbf{H})$ correspond to the non-linear terms in the polarization and magnetization, respectively. However, (1.13) and (1.14) are valid for materials that do not have coupling between the polarization and magnetization. In the presence of coupling, the previous equations are modified to

$$\left.\begin{aligned}\mathbf{D}&=\bar{\bar{\varepsilon}}*\mathbf{E}+\bar{\bar{\xi}}*\mathbf{H}\\ \mathbf{B}&=\bar{\bar{\zeta}}*\mathbf{E}+\bar{\bar{\mu}}*\mathbf{H}\end{aligned}\right\}\Longrightarrow\begin{bmatrix}\mathbf{D}\\ \mathbf{B}\end{bmatrix}=\bar{\bar{C}}*\begin{bmatrix}\mathbf{E}\\ \mathbf{H}\end{bmatrix} \tag{1.15}$$

where $\bar{\bar{C}}$ is a 6×6 matrix, to include such magnetoelectric coupling.

1.3 Models for the Polarization

With natural materials various polarization mechanisms occur at different frquency regions. For example, at GHz frequencies the main polarization effect (usually found in liquids) is due to the orientation of the dipolar molecules, whereas at higher frequencies (i.e., higher than 1 THz) with

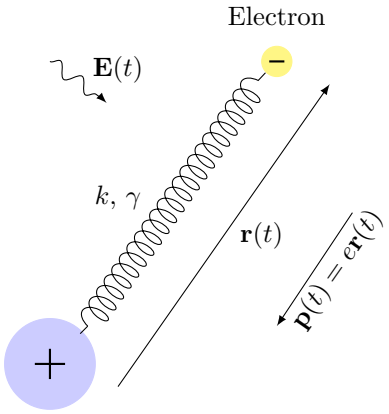


Figure 1.3: Oscillator model of the atom describing electronic polarization effects.

molecules consisting of more than one kind of atoms, the polarization is mainly due to the atomic displacement (i.e., atomic polarization). At optical frequencies, the main polarization effect is due to the relative displacement of the electrons (i.e., electronic polarization). In this section we will focus on the latter polarization mechanism as this is found with metals at optical frequencies and will be used later in Chapter 4.

The dielectric properties of matter can be described by the simplified model of an oscillator, as shown in Fig. 1.3, where the electron is assumed to be bound to the nucleus and oscillating due to an applied electric field $\mathbf{E}(\mathbf{t})$. Thus, a dipole moment $\mathbf{p}(t)$ (in microscopic level) is created because the electron under the existence of the electric field moves away from the nucleus. The macroscopic dipole moment can be obtained by spatial averaging of the microscopic dipole moment over the material's volume. Specifically, if $\mathbf{r}(t)$ is the displacement at the equilibrium state of an electron having a mass of m_e then the inertia force is given by Newton's law $m_e \dfrac{d^2\mathbf{r}(t)}{dt^2}$ and the restoring force can be approximated by the linear term $-k\mathbf{r}(t)$ (in analogy to the spring-mass system in mechanics), where k is a positive constant characteristic of the bond. Here, we assume that the motion of the electron is affected by the fields created by neighbouring atoms that are oscillating due to thermal energy. Thus, the collisions of the electron with neighbouring atoms can be seen as a form of friction that can be described by the term $-m_e\gamma \dfrac{d\mathbf{r}(t)}{dt}$ (proportional to the velocity), where γ is a positive constant. Hence, the equation of motion of the electron can be formulated as

$$\sum \mathbf{F} = m_e\mathbf{a} \Rightarrow m_e \frac{d^2\mathbf{r}(t)}{dt^2} + m_e\gamma\frac{d\mathbf{r}(t)}{dt} + k\mathbf{r}(t) = \underbrace{e\left(\mathbf{E}(t) + \frac{d\mathbf{r}(t)}{dt} \times \mathbf{B}\right)}_{\mathbf{F}_{\text{Lorentz}}} \tag{1.16}$$

where the electron is subject to the Lorentz force $\mathbf{F}_{\text{Lorentz}}$. In the case where $\mathbf{B} = 0$ or practically when $\left|\dfrac{d\mathbf{r}(t)}{dt} \times \mathbf{B}\right| \ll |\mathbf{E}|$, (1.16) reduces to

$$m_e \frac{d^2\mathbf{r}(t)}{dt^2} + m_e\gamma\frac{d\mathbf{r}(t)}{dt} + k\mathbf{r}(t) = e\mathbf{E}(t) \tag{1.17}$$

Equation (1.17) can be transformed in the frequency domain by substituting the phasors $\mathbf{r}(t) = \Re\{\mathbf{r}(\omega)e^{j\omega t}\}$ and $\mathbf{E}(t) = \Re\{\mathbf{E}(\omega)e^{j\omega t}\}$ into (1.17), resulting in

$$-m_e\omega^2\mathbf{r}(\omega) + j\omega m_e\gamma\mathbf{r}(\omega) + k\mathbf{r}(\omega) = e\mathbf{E}(\omega) \tag{1.18}$$

Thus, the displacement can be expressed as:

$$r(\omega) = \frac{-e}{m_e\omega^2 - j\omega m_e\gamma - k}E(\omega) = \frac{-e/m_e}{\omega^2 - \omega_0^2 - j\omega\gamma}E(\omega) \tag{1.19}$$

where $\omega_0 = \sqrt{\dfrac{k}{m_\mathrm{e}}}$ is the eigenfrequency. Writing (1.19) in the time domain one gets

$$r(t) = \Re\left\{\frac{-e/m_\mathrm{e}}{\omega^2 - \omega_0^2 - j\omega\gamma}E(\omega)e^{j\omega t}\right\} \tag{1.20}$$

Now, assuming that there are N such dipoles the polarization can be written as follows

$$P(t) = -\Re\left\{\frac{Ne^2/m_\mathrm{e}}{\omega^2 - \omega_0^2 - j\omega\gamma}E(\omega)e^{j\omega t}\right\} \tag{1.21}$$

Here, the assumption that the dipoles are independent is made, since any dependence between them has been taken into account in (1.17) by the friction term. Therefore, (1.21) can be written in the frequency domain as

$$P(\omega) = \varepsilon_0\frac{\omega_\mathrm{p}^2}{\omega_0^2 - \omega^2 + j\omega\gamma}E(\omega) \tag{1.22}$$

where $\omega_\mathrm{p}^2 = \dfrac{Ne^2}{\varepsilon_0 m_\mathrm{e}}$ is the plasma angular frequency. The displacement vector can then be expressed as

$$\mathbf{D}(\omega) = \varepsilon_0\mathbf{E}(\omega) + \mathbf{P}(\omega) = \varepsilon_0\left(1 + \underbrace{\frac{\omega_\mathrm{p}^2}{\omega_0^2 - \omega^2 + j\omega\gamma}}_{\chi(\omega)}\right)E(\omega) \equiv \varepsilon_0\varepsilon_\mathrm{r}(\omega)E(\omega) \tag{1.23}$$

where $\varepsilon_\mathrm{r} = 1 + \dfrac{\omega_\mathrm{p}^2}{\omega_0^2 - \omega^2 + j\omega\gamma} \equiv \varepsilon_\mathrm{r}'(\omega) - j\varepsilon_\mathrm{r}''(\omega)$ with $\varepsilon_\mathrm{r}'(\omega) = 1 + \underbrace{\dfrac{\omega_\mathrm{p}^2\left(\omega_0^2 - \omega^2\right)}{\left(\omega_0^2 - \omega^2\right)^2 + \omega^2\gamma^2}}_{\chi'(\omega)}$ and $\varepsilon_\mathrm{r}''(\omega) = \dfrac{\omega_\mathrm{p}^2\omega\gamma}{\left(\omega_0^2 - \omega^2\right)^2 + \omega^2\gamma^2} = \chi''(\omega)$. This frequency dispersion model is usually referred to as the Lorentz dispersion model. However, natural materials very often exhibit many Lorentz type resonances (i.e., due to different polarization mechanisms) resulting in a dielectric function of the form [1, 2]

$$\varepsilon(\omega) = \varepsilon_0\left(1 + \sum_i \frac{N_i e^2/m_i\varepsilon_0}{\omega_{0i}^2 - \omega^2 + j\omega\gamma_i}\right)^1 \tag{1.24}$$

It is important to note that different mechanisms have different values for the parameters ω_{0i} and γ_i. Starting from (1.23), one can investigate various limit cases of great practical interest. For example, $\lim\limits_{\gamma\to 0}\chi(\omega)$ gives the susceptibility of a lossless dielectric (i.e., there are no collisions). Thus, following from (1.23) the susceptibility can be written as

$$\begin{aligned}\chi(\omega) &= \lim_{\gamma\to 0^+}\frac{\left(\omega_0^2 - \omega^2\right)^2}{\left(\omega_0^2 - \omega^2\right)^2 + \omega^2\gamma}\frac{\omega_\mathrm{p}^2}{\left(\omega_0^2 - \omega^2\right)^2} - j\lim_{\gamma\to 0^+}\frac{\omega_\mathrm{p}^2\omega\gamma}{\left(\omega_0^2 - \omega^2\right)^2 + \omega^2\gamma} \\ &= \frac{\omega_\mathrm{p}^2}{\omega_0^2 - \omega^2} - j\frac{\pi\omega_\mathrm{p}^2}{\omega}\lim_{\gamma\to 0^+}\frac{1}{\pi}\frac{\gamma}{\left(\dfrac{\omega_0^2 - \omega^2}{\omega}\right)^2 + \gamma^2} = \frac{\omega_\mathrm{p}^2}{\omega_0^2 - \omega^2} - j\frac{\pi\omega_\mathrm{p}^2}{\omega}\delta\left(\frac{\omega_0^2 - \omega^2}{\omega}\right)\end{aligned} \tag{1.25}$$

[1]This expression can also be interpreted using a quantum-mechanical approach as

$$\varepsilon(\omega) = \varepsilon_0\left(1 + \sum_{j>i}\frac{f_{ji}(N_i - N_j)e^2/m\varepsilon_0}{\omega_{0ji}^2 - \omega^2 + j\omega\gamma_{ji}}\right)$$

where $\omega_{0ji} = \dfrac{E_j - E_i}{\hbar}$ and N_j, N_i are the populations of the energy levels E_j and E_i, respectively. Here, f_{ji} are called "oscillator strengths" and they obey the rule $\sum f_{ji} = Z$ with Z being the atomic number.

After some algebraic manipulations and using the properties of the Dirac's delta function, (1.25) is written as

$$\chi(\omega) = \frac{\omega_{\mathrm{p}}^2}{\omega_0^2 - \omega^2} - j\frac{\pi\omega_{\mathrm{p}}^2}{2\omega}\Big[\delta(\omega-\omega_0) + \delta(\omega+\omega_0)\Big] = \frac{\omega_{\mathrm{p}}^2}{\omega_0^2 - \omega^2} - j\frac{\pi\omega_{\mathrm{p}}^2}{2\omega_0}\Big[\delta(\omega-\omega_0) - \delta(\omega+\omega_0)\Big] \quad (1.26)$$

Similarly, the susceptibility of lossy plasma media (i.e., $\omega_0 \to 0$ and $\gamma \neq 0$) is given by

$$\begin{aligned}\chi(\omega) &= \omega_{\mathrm{p}}^2 \lim_{\omega_0\to 0^+} \frac{1}{j\omega(\gamma+j\omega)+\omega_0^2} = \frac{\omega_{\mathrm{p}}^2}{\gamma+j\omega}\lim_{\omega_0\to 0^+}\frac{1}{j\omega + \dfrac{\omega_0^2}{\gamma+j\omega}} = \frac{\omega_{\mathrm{p}}^2}{\gamma+j\omega}U(\omega) \\ &= \frac{\omega_{\mathrm{p}}^2}{\gamma+j\omega}\left(\frac{1}{j\omega} + \pi\delta(\omega)\right) = \frac{\omega_{\mathrm{p}}^2}{j\omega(\gamma+j\omega)} + \frac{\pi\omega_{\mathrm{p}}^2\delta(\omega)}{\gamma+j\omega} = \frac{\omega_{\mathrm{p}}^2}{j\omega(\gamma+j\omega)} + \frac{\pi\omega_{\mathrm{p}}^2\delta(\omega)}{\gamma} \end{aligned} \quad (1.27)$$

which in the case of collisionless (i.e., lossless) plasma ($\omega_0 \to 0$ and $\gamma \to 0$) reduces to

$$\chi(\omega) = -\frac{\omega_{\mathrm{p}}^2}{\omega^2} \quad (1.28)$$

Usually dispersion within metals is also of great practical interest. Within metals conduction electrons can move freely. This means that the simple polarization model presented in Fig. 1.3 is still valid with the modification that the restoring force is zero. Thus, (1.17) reduces to

$$m_{\mathrm{e}}\frac{d^2\mathbf{r}(t)}{dt^2} + m_{\mathrm{e}}\gamma\frac{d\mathbf{r}(t)}{dt} = e\mathbf{E}(t) \quad (1.29)$$

$$m_{\mathrm{e}}\frac{d\mathbf{v}(t)}{dt} + m_{\mathrm{e}}\gamma\mathbf{v}(t) = e\mathbf{E}(t) \overset{\mathbf{J}=-Ne\mathbf{v}}{\Longrightarrow} \quad (1.30)$$

$$\frac{d\mathbf{J}(t)}{dt} + \gamma\mathbf{J}(t) = \frac{Ne^2}{m_{\mathrm{e}}}\mathbf{E}(t) \quad (1.31)$$

Solving for the current density, one can obtain the frequency domain relationship

$$\mathbf{J}(\omega) = \frac{\dfrac{Ne^2}{m_{\mathrm{e}}}}{1+\dfrac{j\omega}{\gamma}}\mathbf{E}(\omega) = \frac{\sigma_0}{1+j\omega\tau}\mathbf{E}(\omega) \quad (1.32)$$

where $\sigma_0 = \dfrac{Ne^2}{m_{\mathrm{e}}\gamma} = \omega_{\mathrm{p}}^2\varepsilon_0\tau$, corresponding to the well-known Drude dispersion model. In the more general case of an anisotropic material the conductivity becomes a tensor and $\mathbf{J}(\omega) = \bar{\bar{\sigma}}(\omega)\cdot\mathbf{E}(\omega)$.

The short analysis presented here on the material parameters is of great importance when undertaking full-wave numerical simulations since it helps to avoid erroneous results that may be latent [3].

1.4 Brillouin Zones

In this section, a brief overview of the analysis of periodic structures is presented. This approach is used in Chapter 3 to study the electromagnetic behaviour of metamaterial waveguides. Generally, periodic structures of infinite extent (see Fig. 1.4(a)) can be studied by calculating their electromagnetic behaviour within a unit cell of their lattice. This makes the analysis of such structures possible because geometric periodicity results in periodic field distributions. According to Floquet-Bloch

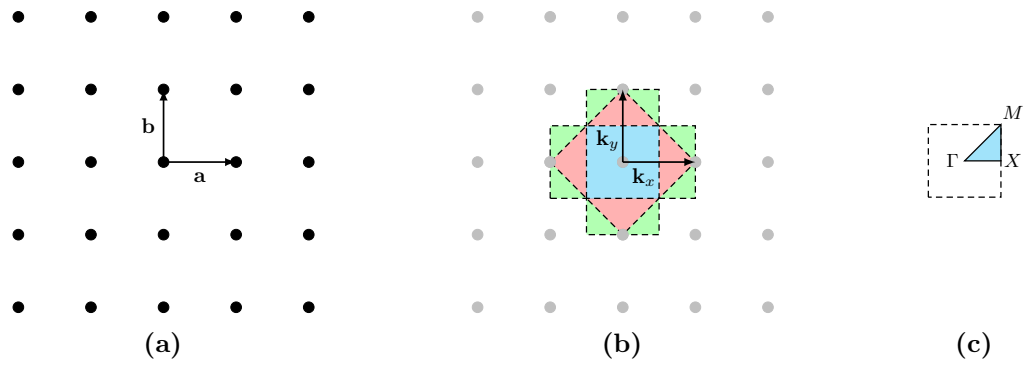


Figure 1.4: Construction of the Brillouin zones with a square lattice. (a) The periodic structure in the physical space (direct lattice) with primitive lattice vectors (**a**, **b**). (b) The first three Brillouin zones in the reciprocal space (**k**-space) and (c) the irreducible Brillouin zone.

theorem the electromagnetic fields in a periodic structure can be expanded into Fourier series with each term corresponding to a spatial Floquet harmonic [4]. Therefore, it is sufficient to describe the wave propagation within a single unit cell since the behaviour at any other lattice point is associated with the behaviour at a point within the first Brillouin zone. In other words, once the fields are obtained at every point within a unit cell, they can then be calculated at a generic point in the structure because they share the same periodicity with the lattice.

A quick way to determine the Brillouin zones is as follows. Starting from a fixed point (i.e., origin), lines to the nearest neighbours are drawn with orthogonal lines crossing them in the middle (the latter lines are called Bragg planes). The points in the reciprocal space (including the origin) that are bound by the Bragg planes form the first Brillouin zone. Similarly, lines from the origin to the next nearest neighbours are drawn with perpendicular lines drawn in the middle (Bragg planes). The points between the first Brillouin zone and the Bragg planes form the second Brillouin zone. Following this approach, the next Brillouin zones can be constructed, as shown in Fig. 1.4(b). The first Brillouin zone can be further simplified by considering only the high symmetry points (Γ, X, M) that form the so-called irreducible Brillouin zone, as shown in Fig. 1.4(c). This is possible because infinite structures have specific symmetry properties and are invariant under translation, rotation and mirror operations. Hence, the irreducible Brillouin zone can be deducted from the first Brillouin zone and vice versa the first Brillouin zone can be reconstructed from the irreducible Brillouin zone, by applying the previous symmetry rules. Therefore, the fields at a generic lattice point can be mapped onto an equivalent point within the irreducible Brillouin zone.

1.5 Surface Plasmon Polaritons

The concept of surface waves is of paramount importance in optics and specifically in plasmonics. Although surface waves can be found with various names, i.e. ground waves, Zenneck waves, Sommerfeld waves, they are usually referred to as surface plasmon polaritons (SPPs) in plasmonics. Physically, SPPs are collective oscillations of electrons at the surface. However, SPPs are just surface waves at a metal-dielectric interface [5]. With a conventional metal-dielectric interface, SPPs can be excited only for a parallel polarized (also referred to as transverse magnetic TM or P-polarized) incoming wave because a normal to the interface electric field component is required to interact with the surface charges. As shown in Fig. 1.5, a parallel polarized (TM) incoming wave has its electric field vector on the plane of incidence, whereas a perpendicular polarized (also referred to as

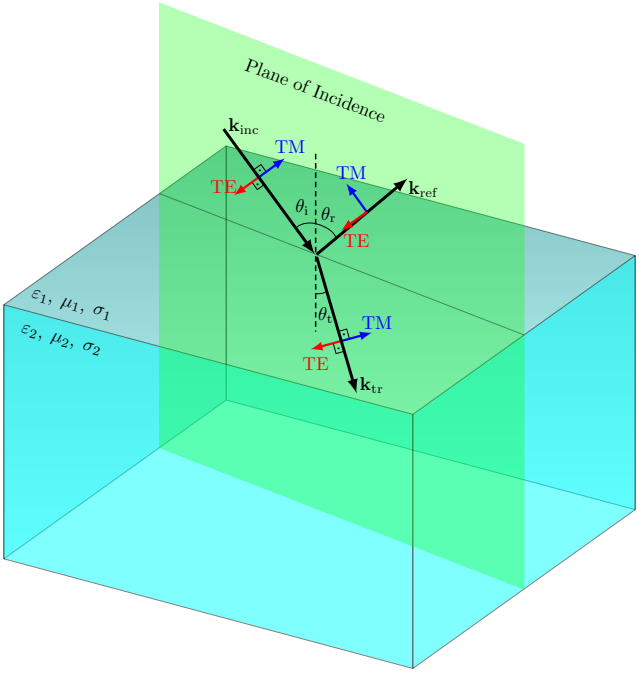


Figure 1.5: Illustration of plane wave impinging at an interface between two media. The electric field orientation for both polarizations (TE and TM) is also shown.

transverse electric TE or S-Polarized) wave has its electric field vector orthogonal to the plane of incidence.

The electromagnetic behaviour of an infinite metal slab when illuminated by a TM polarized wave (Fig. 1.6) can be studied analytically to provide further physical insight in the propagation of surface plasmon polaritons and a solid background for the study presented in Chapter 4. In this type of problems, the dispersion relationship is of great importance since it describes the characteristics of all the modes supported by a structure.

From (1.2)-(1.3) in a source-free region, considering a steady state plane wave solution of the form $\mathbf{E}$, $\mathbf{H} \propto e^{j(\omega t - \mathbf{k}\cdot\mathbf{r})}$ where $\mathbf{k} = (k_x, k_y, k_z)$ and $\mathbf{r} = (x, y, z)$, the magnetic field for a TM polarized incoming wave, with a N-layer structure, can be written as (the time dependence $e^{j\omega t}$ is omitted)

$$H_y = \begin{cases} A_i e^{-j\mathbf{k}_{\text{inc}}\cdot\mathbf{r}} + B_i e^{-j\mathbf{k}_{\text{ref}}\cdot\mathbf{r}} & \text{for } 1 \leqslant i \leqslant N-1 \\ A_i e^{-j\mathbf{k}_{\text{tr}}\cdot\mathbf{r}} & \text{for } i = N \end{cases} \tag{1.33}$$

where A_i and B_i are the amplitudes of the incident wave and reflected wave, respectively, $\mathbf{k}_{\text{inc}} = (k_x, 0, k_{zi})$ is the wavevector of the incident wave, $\mathbf{k}_{\text{ref}} = (k_x, 0, -k_{zi})$ is the wavevector of the reflected wave and $\mathbf{k}_{\text{tr}} = (k_x, 0, k_{zN})$ is the wavevector of the transmitted wave. As can be seen, the magnetic field in each of the first $N-1$ layers is the superposition of an incident wave and a reflected wave. On the other hand, in the N^{th} layer there is only an incident wave since this layer is semi-infinitely thick in the z-direction and hence, there are no reflections. Limiting our study to a 3-layer structure,

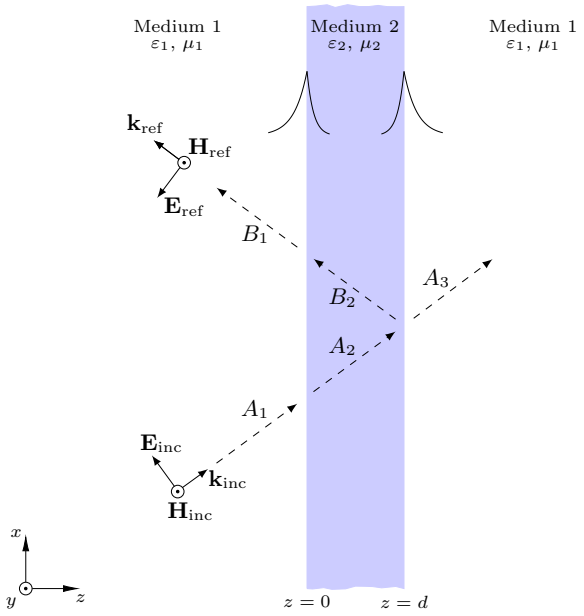


Figure 1.6: Illustration of a TM polarized wave impinging on a slab. The field profiles at the interfaces are also shown.

as shown in Fig. 1.6, (1.33) can be re-written as

$$H_y(x,z) = \begin{cases} \left(A_1 e^{-jk_{z1}z} + B_1 e^{jk_{z1}z}\right) e^{-jk_x x} & \text{for } z \leqslant 0 \\ \left(A_2 e^{-jk_{z2}z} + B_2 e^{jk_{z2}z}\right) e^{-jk_x x} & \text{for } 0 < z < d \\ \left(A_3 e^{-jk_{z1}(z-d)}\right) e^{-jk_x x} & \text{for } z \geqslant d \end{cases} \tag{1.34}$$

$$E_x(x,z) = \begin{cases} \dfrac{k_{z1}}{\omega\varepsilon_1}\left(A_1 e^{-jk_{z1}z} - B_1 e^{jk_{z1}z}\right) e^{-jk_x x} & \text{for } z \leqslant 0 \\ \dfrac{k_{z2}}{\omega\varepsilon_2}\left(A_2 e^{-jk_{z2}z} - B_1 e^{jk_{z2}z}\right) e^{-jk_x x} & \text{for } 0 < z < d \\ \dfrac{k_{z1}}{\omega\varepsilon_1} A_3 e^{-jk_{z1}(z-d)} e^{-jk_x x} & \text{for } z \geqslant d \end{cases} \tag{1.35}$$

$$E_z(x,z) = \begin{cases} -\dfrac{k_x}{\omega\varepsilon_1}\left(A_1 e^{-jk_{z1}z} + B_1 e^{jk_{z1}z}\right) e^{-jk_x x} & \text{for } z \leqslant 0 \\ -\dfrac{k_x}{\omega\varepsilon_2}\left(A_2 e^{-jk_{z2}z} + B_2 e^{jk_{z2}z}\right) e^{-jk_x x} & \text{for } 0 < z < d \\ -\dfrac{k_x}{\omega\varepsilon_1} A_3 e^{-jk_{z1}(z-d)} e^{-jk_x x} & \text{for } z \geqslant d \end{cases} \tag{1.36}$$

where k_{z1} and k_{z2} are the z-component of the wavevector in medium 1 and 2, respectively. Now, enforcing the appropriate boundary conditions at the interfaces at $z = 0$ and $z = d$ (i.e., continuity

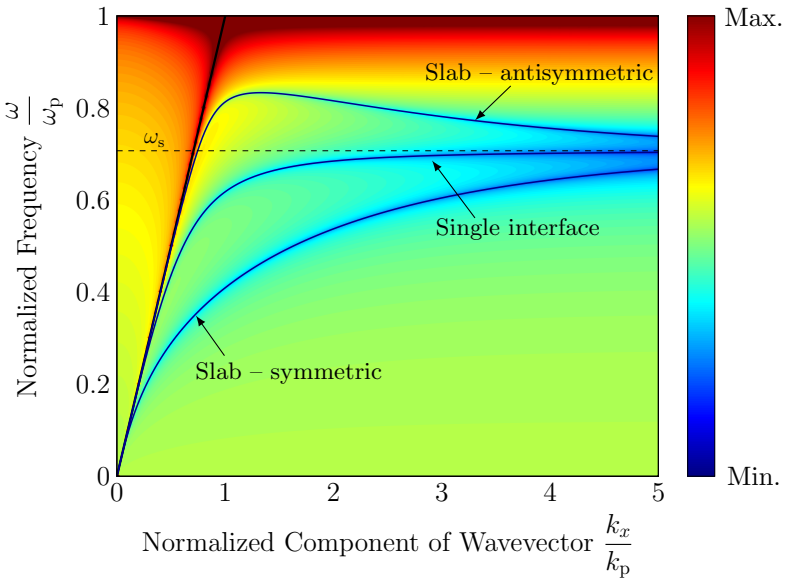


Figure 1.7: Dispersion diagram for a 10 nm gold slab. The surface plasmon resonance is $\omega_s = \frac{\omega_p}{\sqrt{2}}$ is indicated with a dashed line and the dispersion curve for a single interface is also shown for comparison.

of the tangential field components) the following set of equations is obtained.

$$\begin{bmatrix} 1 & 1 & -1 & -1 & 0 \\ 1 & -1 & -\frac{k_{z2}\varepsilon_1}{k_{z1}\varepsilon_2} & \frac{k_{z2}\varepsilon_1}{k_{z1}\varepsilon_2} & 0 \\ 0 & 0 & e^{-jk_{z2}d} & e^{jk_{z2}d} & -1 \\ 0 & 0 & \frac{k_{z2}\varepsilon_1}{k_{z1}\varepsilon_2}e^{-jk_{z2}d} & -\frac{k_{z2}\varepsilon_1}{k_{z1}\varepsilon_2}e^{jk_{z2}d} & -1 \end{bmatrix} \begin{bmatrix} A_1 \\ B_1 \\ A_2 \\ B_2 \\ A_3 \end{bmatrix} = \begin{bmatrix} 0 \\ 0 \\ 0 \\ 0 \end{bmatrix} \tag{1.37}$$

It is interesting to note that there are 5 unknowns and only 4 equations and thus, an unambiguous solution cannot be obtained. However, A_1 can be chosen arbitrarily since it corresponds to the amplitude of the incident field and thus, is known a priori. Therefore, the rest of the unknowns can be expressed as functions of A_1 to obtain an unambiguous solution. Moreover, the reflection and transmission coefficients R and T, respectively can be defined as

$$R = \frac{B_1}{A_1} = \frac{2\left(e^{-j2k_{z2}d} - 1\right)\left[\left(\frac{k_{z2}\varepsilon_1}{k_{z1}\varepsilon_2}\right)^2 - 1\right]}{\left[\frac{k_{z2}\varepsilon_1}{k_{z1}\varepsilon_2} + 1\right]^2 - e^{-j2k_{z2}d}\left[\frac{k_{z2}\varepsilon_1}{k_{z1}\varepsilon_2} - 1\right]^2} \tag{1.38}$$

$$T = \frac{A_3}{A_1} = \frac{4\frac{k_{z2}\varepsilon_1}{k_{z1}\varepsilon_2}e^{-jk_{z2}d}}{\left[\frac{k_{z2}\varepsilon_1}{k_{z1}\varepsilon_2} + 1\right]^2 - e^{-j2k_{z2}d}\left[\frac{k_{z2}\varepsilon_1}{k_{z1}\varepsilon_2} - 1\right]^2} \tag{1.39}$$

The dispersion relation can be obtained from the poles of the reflection coefficient since this corresponds to $A_1 = 0$ and hence, the eigenmodes of the structure can be obtained as

$$k_{z2}\varepsilon_1 - jk_{z1}\varepsilon_2 \cot\left(\frac{k_{z2}d}{2}\right) = 0 \tag{1.40}$$

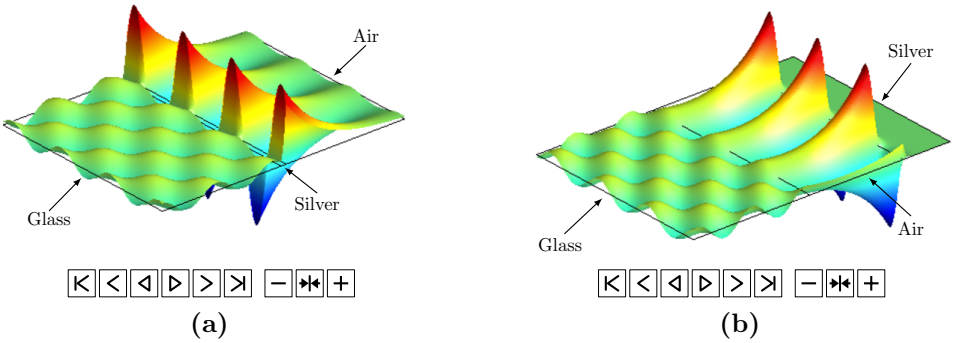


Figure 1.8: Two commonly used surface plasmon resonance excitation configurations. (a) Kretschmann-Raether configuration where the SPP is excited at the rear interface and (b) Otto configuration where the SPP is excited at the front interface.

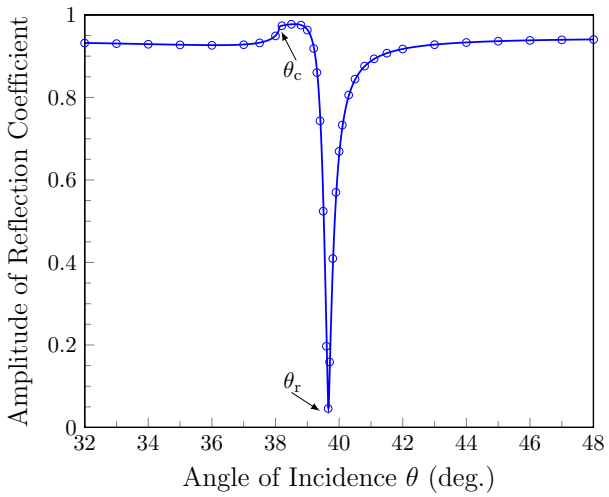
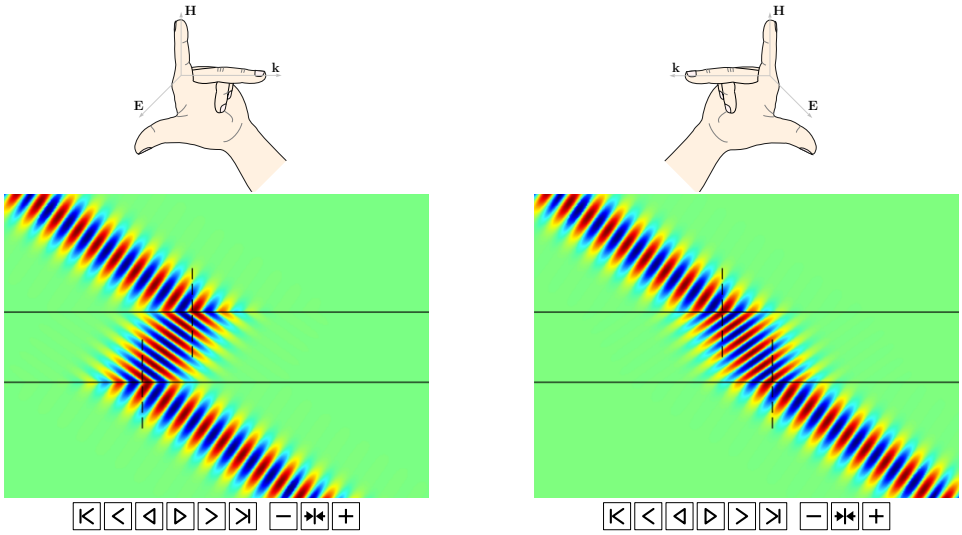


Figure 1.9: Amplitude of the reflection coefficient for a TM incoming wave. The total internal reflection angle θ_c and resonance angle θ_r are also indicated.

$$k_{z2}\varepsilon_1 + jk_{z1}\varepsilon_2 \tan\left(\frac{k_{z2}d}{2}\right) = 0 \tag{1.41}$$

As can be seen, there are two distinct modes with the lowest branch corresponding to a symmetric E_x distribution across the slab and the upper branch corresponding to an antisymmetric E_x distribution. In Fig. 1.7, the dispersion diagram for a 10 nm thick gold slab with $\varepsilon_2 = \varepsilon_0\left(1 - \frac{\omega_p^2}{\omega^2}\right)$ and $\mu_2 = \mu_0$ is shown, where the dispersion curve for a single interface ($N = 2$) is also plotted for comparison.

Usually, SPPs cannot be excited by a wave traveling in free-space and hence special configurations are required. This can be seen in Fig. 1.7 where the light line does not cross the dispersion curves and hence, there is no k_x that can excite the SPPs. For this reason, special structures are required with two well-known excitation configurations shown in Fig. 1.8, where a prism is used to excite the SPPs. In order to excite a SPP, the incoming wave must impinge on the interface at an angle θ_r greater than the critical angle θ_c corresponding to total internal reflection, as shown in Fig. 1.9.



(a) (b)

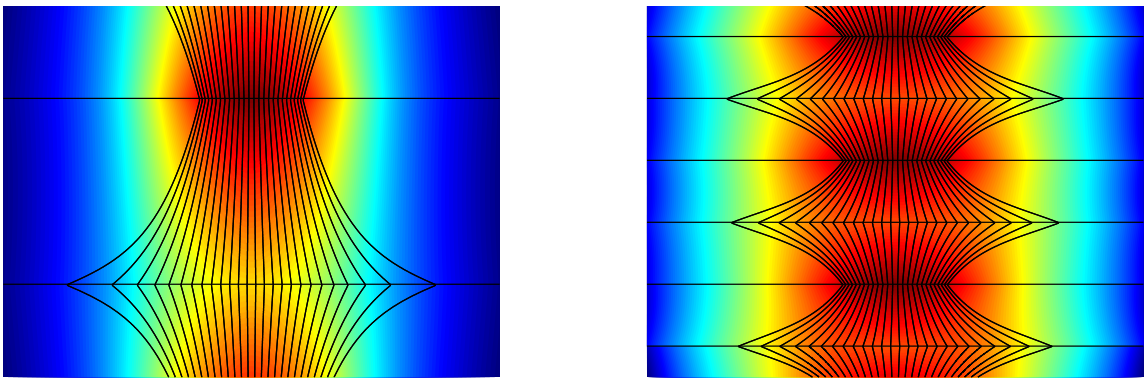
Figure 1.10: A weakly focused Gaussian beam impinging on a dielectric slab with (a) $\varepsilon_{\mathrm{r}} = -2$ and $\mu_{\mathrm{r}} = -1$ and (b) $\varepsilon_{\mathrm{r}} = 2$ and $\mu_{\mathrm{r}} = 1$. The direction of propagation can be determined by the left/right hand rule as shown at the top.

1.6 Metamaterials Applications

In this section, based on the previous analysis, some illustrative applications are presented in order to demonstrate how practical devices with desired unusual electromagnetic properties can be realized and some of the opportunities offered by metamaterials are discussed. The story of metamaterials is considered as a relatively new research field since the term "metamaterial" was first introduced two decades ago to describe engineered materials with unusual electromagnetic behaviour resulting from their structure. These materials usually have inclusions much smaller than the operation wavelength and hence, they can be characterized using homogenization techniques by effective material parameters. For example, negative index media is one of the most popular classes of metamaterials. However, the first report of negative refraction was at the beginning of the previous century and very few works had been published until the beginning of the 21$^{\mathrm{st}}$ century where an explosion of interest took place with numerous works.

One of the first highlights of metamaterials was the implementation of negative refraction media (media having negative permittivity and permeability simultaneously). As seen in Fig. 1.10(a), where a slab with negative refractive index is illuminated by a weakly focused Gaussian beam, the phase velocity and the propagation direction are antiparallel within the slab and the beam bends away from the normal when incident at the top interface. This is in contrast to conventional media, as shown in Fig. 1.10(b), where the beam bends toward the normal when propagating from air to a denser medium and the phase velocity and propagation direction are always parallel. Further insight in the response of a negative index slab can be obtained from the analysis presented in Section 1.5 by setting $\varepsilon_{2\mathrm{r}} = \mu_{2\mathrm{r}} = -1$. It is interesting to note that such a slab is matched to free-space impedance (i.e., $R = 0$) and that the propagating waves (with k_z real) undergo negative refraction whereas the evanescent waves (with k_z imaginary) undergo amplitude amplification. The latter is a key property of a negative index media and allows the realization of flat lenses with super-resolution.

One of the challenges for many years was the implementation of imaging devices with sub-wavelength resolution. Metamaterials revealed various ways to realize such devices. As mentioned previously, negative refractive index media is only one way to implement a flat superlens [5, 7].



(a) (b)

Figure 1.11: Superlens with sub-wavelength resolution realized by (a) a silver slab and (b) a stack of silver slabs. The thickness of the slab(s) is 10 nm. Poynting vector streamlines are also shown.

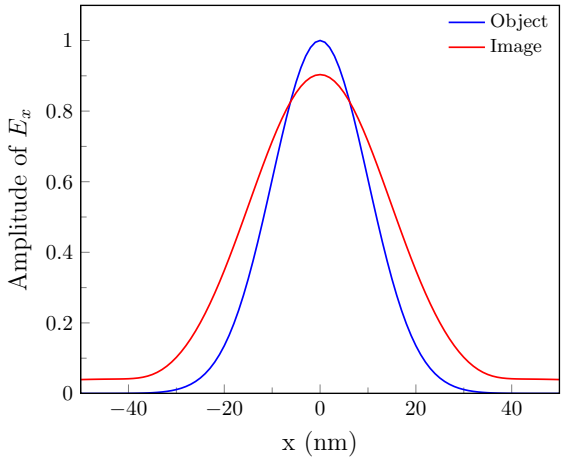
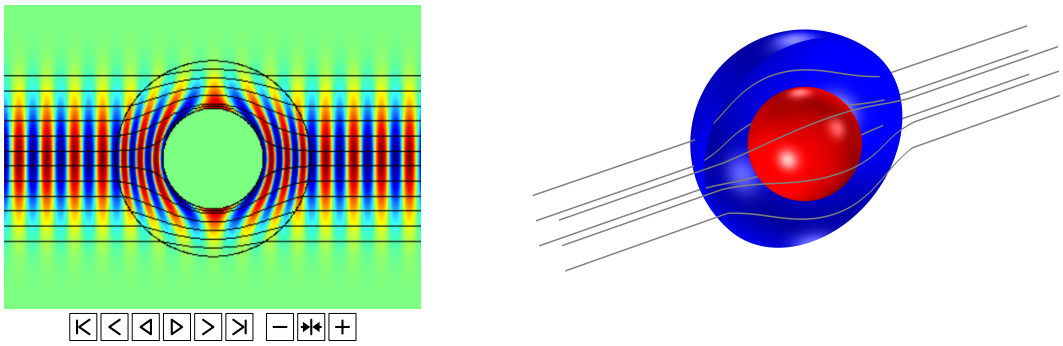


Figure 1.12: Electric field profile for the lens shown in Fig. 1.11(a).

However, a slab with negative permittivity can also be used for sub-wavelength resolution. As is well-known, the concept of sub-wavelength imaging requires the excitation of coupled SPPs at the two interfaces across the slab. The imaging properties of the slab can be studied by decomposing the object field into its k_x-spectrum (for 1D imaging) using the Fourier Transform and the contributions of all k_x components are then added to obtain the field distribution at any point in space. The super-resolution is obtained due to the amplification of the amplitude of the evanescent field components (containing the high-resolution information) within the slab. As shown in Fig. 1.11(a), a silver slab can be employed to realize a superlens (for TM polarization) at optical frequencies –at microwave and millimeter-wave frequencies, the use of metamaterials is needed to provide a negative permittivity material. Also, with the use of metamaterials it is possible to realize a lens with super-resolution for TE polarization by controlling the permeability. This lens offers sub-wavelength resolution by reconstructing the near-field evanescent waves and therefore, for most practical applications several layers need to be stacked so that the image can be translated to larger distances, as shown in Fig. 1.11(b).

Fig. 1.11 shows the electric field profile at the object and image planes for the single slab lens shown in Fig. 1.10(a). The object represented by a Gaussian field distribution is transferred to the image plane with similar form although its peak is lower and bandwidth broader.



(a) **(b)**

Figure 1.13: A weakly focused Gaussian beam impinging on an invisibility cloak. (a) 2D view and (b) 3D view. The power flow is also shown with lines.

Another application that has drawn much attention is the so-called invisibility cloak. One way to implement such a cloak is with a material that is able to divert electromagnetic waves so that they bypass around an object surrounded by the cloak [6]. The material forming the cloak is usually realized by employing anisotropy in both the permittivity and permeability. As shown in Fig. 1.13, when a beam impinges on the cloak the object placed in the interior is hidden since it does not cause any perturbation to the incident beam i.e., there is no scattering due to the object. Thus, any objects surrounded by the cloak are invisible to an observer located outside the cloak. The implementation of such a device requires a highly anisotropic material that enables different levels of divergence to the incident wave (the rays closer to the center of the cloak deflect stronger). For example, the cloak shown in Fig. 1.13 has the following material dyadics [8].

$$\bar{\bar{\varepsilon}}_{\mathrm{r}} = \bar{\bar{\mu}}_{\mathrm{r}} = \begin{bmatrix} \dfrac{r-R_1}{r}\cos^2\phi + \dfrac{r}{r-R_1}\sin^2\phi & \left(\dfrac{r-R_1}{r} - \dfrac{r}{r-R_1}\right)\sin\phi\cos\phi & 0 \\ \left(\dfrac{r-R_1}{r} - \dfrac{r}{r-R_1}\right)\sin\phi\cos\phi & \dfrac{r-R_1}{r}\sin^2\phi + \dfrac{r}{r-R_1}\cos^2\phi & 0 \\ 0 & 0 & \left(\dfrac{R_2}{R_2-R_1}\right)^2\dfrac{r-R_1}{r} \end{bmatrix} \tag{1.42}$$

where R_1 and R_2 are the radii of the inner and outer shells, respectively.

As is clear, metamaterials offer the opportunity to realize devices with extraordinary characteristics and therefore, it is natural to attract significant research interest from across many disciplines as they can be employed in a diverse range of applications.

References

[1] J. D. Jackson, "Classical electrodynamics", 3rd ed., *Wiley*, 1998

[2] S. J. Orfanidis, "Electromagnetic waves and antennas", Available online: http://www.ece.rutgers.edu/ orfanidi/ewa/, 2008

[3] E. Episkopou, S. Papantonis, W. J. Otter and S. Lucyszyn, "Defining material parameters in commercial EM solvers for arbitrary metal-based THz structures", *IEEE Trans. Terahertz Sci. Technol.*, vol. 2, no. 5 pp. 513-524, Sep. 2012

[4] L. Brillouin, "Wave propagation in periodic structures", *Dover Publications Inc.*, 1953

[5] L. Solymar and E. Shamonina, "Waves in metamaterials", *Oxford University Press*, 2009

[6] D. Schurig, J. J. Mock, B. J. Justice, S. A. Cummer, J. B. Pendry, A. F. Starr, D. R. Smith, "Metamaterial electromagnetic cloak at microwave frequencies", *Science*, vol. 314, no. 5801, pp. 977-980, Oct. 2006

[7] J. B. Pendry, "Negative refraction makes a perfect lens", *Phys. Rev. Lett.*, vol. 85, no. 18, pp. 3966-3969, Oct. 2000

[8] S. A. Cummer, B. I. Popa, D. Schurig, D. R. Smith and J. B. Pendry, "Full-wave simulations of electromagnetic cloaking structures", *Phys. Rev. E*, vol. 74, p. 036621, Sep. 2006

Chapter 2

The "Fakir's Bed of Nails" Metamaterial

In this chapter, a detailed study of the "Fakir's bed of nails" metamaterial is presented. Its properties are derived from first principles using homogenization techniques and emphasis is given on the strong spatial dispersion associated with the wire medium structure. The dispersion characteristics are obtained analytically for both polarizations (TE and TM) and additional boundary conditions (necessary with spatially dispersive media) are introduced in order to describe the propagation effects in the "Fakir's bed of nails". Moreover, simplified models appropriate for densely packed pins are presented and practical applications of the "Fakir's bed of nails" metamaterial are also discussed.

2.1 Introduction

Over the last decade, from across many disciplines, there has been a great deal of activity in the area of metamaterials that brought to light opportunities to engineer devices with superior performance and unusual characteristics. One of the most thoroughly studied classes of metamaterials is the so-called wire medium, which was first introduced in 1953 as a dielectric with permittivity below unity that could be used for microwave lenses [1–5]. Some years later, it was also used to emulate a medium with plasma properties [6], whereas in 1983 an array of metal pins attached to a ground plane, as shown in Fig. 2.1, was introduced in order to implement a surface reactance [7].

However, spatial dispersion effects were neglected at that time. Thirty years later, it was shown that the wire medium possesses strong spatial dispersion characteristics, even at low frequencies, which cannot be neglected [8, 9]. In addition to the transverse electromagnetic (TEM) mode, an additional transverse magnetic (TM) mode is supported within the wire medium, as shown by its amplitude $A_{\mathrm{TM}}^{\pm}$ in Fig. 2.1. As a result, a rigorous study of such metamaterials was then undertaken in [10–19], where accurate analytical models were derived using additional boundary conditions and/or quasi-static approximations, to eliminate the additional degree of freedom due to spatial dispersion. However, when the spacing between adjacent pins is small compared to the wavelength of the incident electromagnetic wave, the surface impedance does not depend on the incident angle. In a case like this, the pins act as transmission lines that are short-circuited at the one end (ground plane) and hence, the TEM mode is supported [9, 20].

To accurately predict the electromagnetic behaviour of this microstructured material the permittivity dyadic needs to be non-local because of the charge accumulation along the pins. This means that for plane waves the permittivity of the wire medium depends not only on the frequency but also on the components of the wave vector. In this case the relative permittivity dyadic $\overline{\overline{\varepsilon}}_{\mathrm{r}}$ of

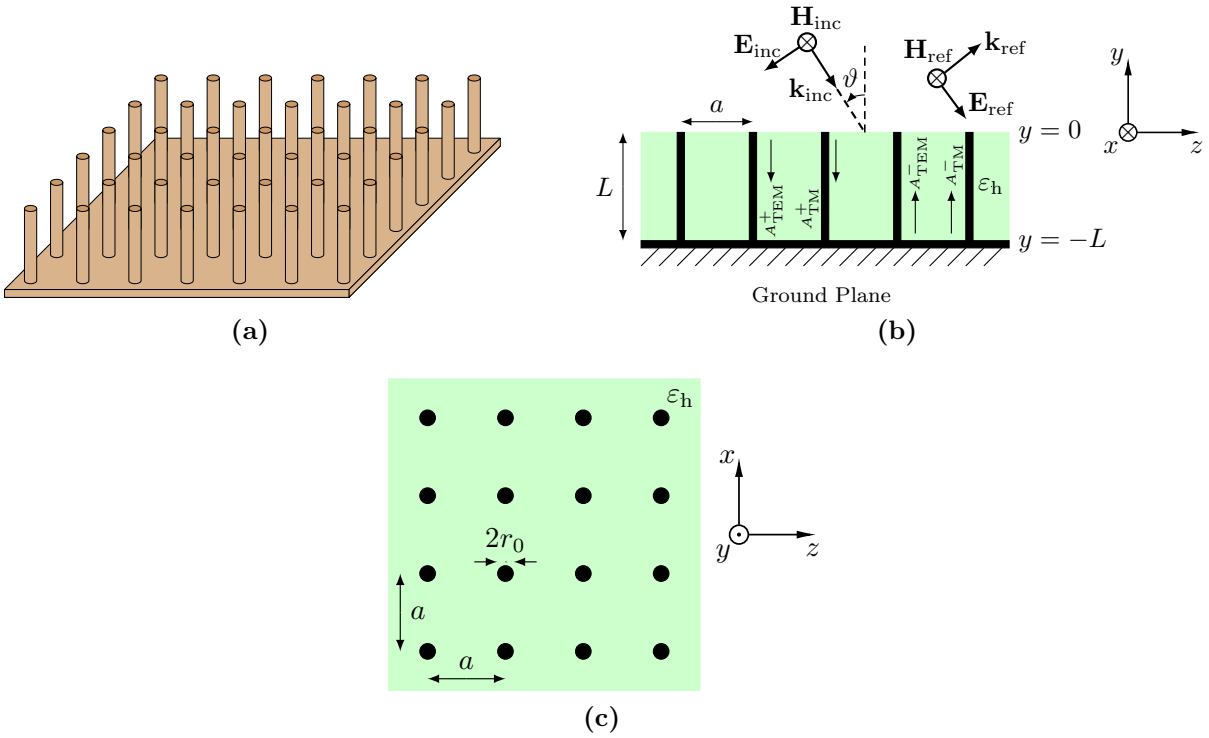


Figure 2.1: Geometry of the proposed Fakir's bed of nails. (a), Perspective view, (b) side view and (c) top view. It is formed by metallic pins arranged periodically in a square lattice (with periodicity a). They are embedded in a host dielectric substrate and their bottom ends are connected to a ground plane.

the medium can be written in the form [9]

$$\bar{\bar{\varepsilon}}_{\text{r}} = \varepsilon_{\text{h}} \left(\mathbf{u}_x \mathbf{u}_x + \varepsilon_{yy} \mathbf{u}_y \mathbf{u}_y + \mathbf{u}_z \mathbf{u}_z \right) \quad \text{where} \quad \varepsilon_{yy} = 1 - \frac{k_{\text{p}}^2}{k_{\text{h}}^2 - k_y^2} \tag{2.1}$$

and for square lattices $k_{\text{p}}^2 = \dfrac{2\pi/a^2}{\ln\left(\dfrac{a}{2\pi r_0}\right) + 0.5275}$ [9, 20]. Also, a is the periodicity of the lattice, r_0 is the radius of the pins ($r_0 \ll \lambda$ where λ is the wavelength of operation), $k_{\text{h}} = k_0\sqrt{\varepsilon_{\text{h}}}$ is the wavenumber in the host medium, $k_0 = \omega/c$ is the free-space wavenumber, ε_h is the relative permittivity of the dielectric host medium and k_y is the component of the wave vector along the y-direction (axis of the pins). By inspection of (2.1), it is clear that the wire medium is described by an anisotropic permittivity that is equal to the permittivity of free space in the transverse to the pins plane (x-z plane) and has a Drude-like response along the pins. This is expected to some extent since the pins limit the electrons to move only along the y-direction. Specifically, the dependence of ε_{yy} on k_y means that permittivity depends on spatial derivative with respect to y and thus, is spatially dispersive. As can be seen from (2.1) the pins are assumed to be very thin so that the permittivity in the x-z plane is that of free space (ε_0). Furthermore, equation (2.1) suggests that the wire medium can be treated as a uniaxial medium with the optical axis along the y-direction.

The dispersion equation can be derived directly starting from the Maxwell's equations. Assuming plane waves of the form $\mathbf{E}(\mathbf{r}) = \mathbf{E}_0 e^{-j\mathbf{k}\cdot\mathbf{r}}$ and $\mathbf{H}(\mathbf{r}) = \mathbf{H}_0 e^{-j\mathbf{k}\cdot\mathbf{r}}$ the Maxwell's equations in the $(\omega, \mathbf{k})$ domain can be written in the following form

$$\mathbf{k} \times \mathbf{E}_0 = k_0 \eta_0 \bar{\bar{\mu}}_{\text{r}} \cdot \mathbf{H}_0 \tag{2.2}$$

$$\mathbf{k}\times\mathbf{H}_0=-\frac{k_0}{\eta_0}\bar{\bar{\varepsilon}}_{\mathrm{r}}\cdot\mathbf{E}_0 \tag{2.3}$$

where $\eta_0=\sqrt{\dfrac{\mu_0}{\varepsilon_0}}$ is the free-space impedance and in our case $\bar{\bar{\mu}}_{\mathrm{r}}=\bar{\bar{I}}$ because the wire medium does not have any magnetic materials. After some calculations the fields inside the medium can be decomposed into TE^y and TM^y waves and hence, the dispersion equation for each one of them obtained separately, as shown in what follows.

$$\left.\begin{aligned}\mathbf{k}\times\mathbf{E}_0=k_0\eta_0\bar{\bar{\mu}}_{\mathrm{r}}\cdot\mathbf{H}_0 &\overset{(\varepsilon_{\mathrm{t}}\mathbf{E}_0)\cdot}{\Longrightarrow}\ \varepsilon_{\mathrm{t}}\mathbf{E}_0\cdot\big(\mathbf{k}\times\mathbf{E}_0\big)=k_0\eta_0\varepsilon_{\mathrm{t}}\mathbf{E}_0\cdot\bar{\bar{\mu}}_{\mathrm{r}}\cdot\mathbf{H}_0\\ \mathbf{k}\times\mathbf{H}_0=-\frac{k_0}{\eta_0}\bar{\bar{\varepsilon}}_{\mathrm{r}}\cdot\mathbf{E}_0 &\overset{(\mu_{\mathrm{t}}\mathbf{H}_0)\cdot}{\Longrightarrow}\ \mu_{\mathrm{t}}\mathbf{H}_0\cdot\big(\mathbf{k}\times\mathbf{H}_0\big)=-\frac{k_0}{\eta_0}\mu_{\mathrm{t}}\mathbf{H}_0\cdot\bar{\bar{\varepsilon}}_{\mathrm{r}}\cdot\mathbf{E}_0\end{aligned}\right\}\Longrightarrow \tag{2.4}$$

$$\left.\begin{aligned}\mathbf{E}_0\cdot\big(\varepsilon_{\mathrm{t}}\bar{\bar{\mu}}_{\mathrm{r}}\big)\cdot\mathbf{H}_0=0\\ -\mathbf{E}_0\cdot\big(\mu_{\mathrm{t}}\bar{\bar{\varepsilon}}_{\mathrm{r}}\big)\cdot\mathbf{H}_0=0\end{aligned}\right\}\overset{(+)}{\Rightarrow}\mathbf{E}_0\cdot\big(\varepsilon_{\mathrm{t}}\bar{\bar{\mu}}_{\mathrm{r}}-\mu_{\mathrm{t}}\bar{\bar{\varepsilon}}_{\mathrm{r}}\big)\cdot\mathbf{H}_0=\big(\varepsilon_{\mathrm{t}}\mu_{yy}-\mu_{\mathrm{t}}\varepsilon_{yy}\big)\underbrace{\overbrace{\big(\mathbf{E}_0\cdot\mathbf{u}_y\big)}^{E_y=0}}_{\text{TE mode}}\underbrace{\overbrace{\big(\mathbf{H}_0\cdot\mathbf{u}_y\big)}^{H_y=0}}_{\text{TM mode}}=0 \tag{2.5}$$

where μ_{t} and ε_{t} are the relative permeability and permittivity, respectively in the x-z plane. As is well-known, for a TE^y wave the following two conditions hold; $\mathbf{k}\cdot\mathbf{E}=0$ and $\mathbf{u}_y\cdot\mathbf{E}=0$. Similarly, for a TM^y wave $\mathbf{k}\cdot\mathbf{H}=0$ and $\mathbf{u}_y\cdot\mathbf{H}=0$. So the fields can be written as [21, 22]

$$\mathbf{E}_{\mathrm{TE}}\big(\mathbf{r}\big)=\frac{\mathbf{u}_y\times\mathbf{k}}{|\mathbf{u}_y\times\mathbf{k}|}E_0e^{-j\mathbf{k}\cdot\mathbf{r}} \tag{2.6}$$

$$\mathbf{H}_{\mathrm{TM}}\big(\mathbf{r}\big)=\frac{\mathbf{u}_y\times\mathbf{k}}{|\mathbf{u}_y\times\mathbf{k}|}H_0e^{-j\mathbf{k}\cdot\mathbf{r}} \tag{2.7}$$

Substituting equations (2.6) into (2.2) and (2.7) into (2.3) we get

$$\mathbf{E}_{\mathrm{TM}}\big(\mathbf{r}\big)=-\frac{\eta_0}{k_0|\mathbf{u}_y\times\mathbf{k}|}\bar{\bar{\varepsilon}}_{\mathrm{r}}^{-1}\cdot\mathbf{k}\times\big(\mathbf{u}_y\times\mathbf{k}\big)H_0e^{-j\mathbf{k}\cdot\mathbf{r}} \tag{2.8}$$

$$\mathbf{H}_{\mathrm{TE}}\big(\mathbf{r}\big)=\frac{1}{k_0|\mathbf{u}_y\times\mathbf{k}|}\bar{\bar{\mu}}_{\mathrm{r}}^{-1}\cdot\mathbf{k}\times\big(\mathbf{u}_y\times\mathbf{k}\big)E_0e^{-j\mathbf{k}\cdot\mathbf{r}} \tag{2.9}$$

The dispersion equation for the TM^y polarization can be found by inserting (2.8) into (2.3) as shown below.

$$\begin{aligned}\mathbf{k}\times\left(\bar{\bar{\varepsilon}}_{\mathrm{r}}^{-1}\cdot\Big[\mathbf{k}\times\big(\mathbf{u}_y\times\mathbf{k}\big)\Big]\right)+k_0^2\bar{\bar{\mu}}_{\mathrm{r}}\cdot\big(\mathbf{u}_y\times\mathbf{k}\big)=0\\ (k_x\mathbf{u}_z-k_z\mathbf{u}_x)\Big[\varepsilon_{\mathrm{t}}\big(k_x^2+k_z^2\big)+k_y^2\varepsilon_{\mathrm{yy}}-\varepsilon_{yy}\varepsilon_{\mathrm{t}}\mu_{\mathrm{t}}k_0^2\Big]=0\\ \varepsilon_{\mathrm{t}}\big[(\mathbf{u}_x\cdot\mathbf{k})(\mathbf{u}_x\cdot\mathbf{k})+(\mathbf{u}_z\cdot\mathbf{k})(\mathbf{u}_z\cdot\mathbf{k})\big]+\varepsilon_{yy}(\mathbf{u}_y\cdot\mathbf{k})(\mathbf{u}_y\cdot\mathbf{k})-\varepsilon_{yy}\varepsilon_{\mathrm{t}}\mu_{\mathrm{t}}k_0^2=0\end{aligned} \tag{2.10}$$

which can be written in a more compact form as [21]

$$\bar{\bar{\varepsilon}}_{\mathrm{r}}\colon\mathbf{kk}-\varepsilon_{yy}\varepsilon_{\mathrm{t}}\mu_{\mathrm{t}}k_0^2=0 \tag{2.11}$$

where ″: ″stands for the double dot product [23]. Following the same procedure the dispersion equation for the TE^y wave can be written as

$$\bar{\bar{\mu}}_{\mathrm{r}}\colon\mathbf{kk}-\mu_{yy}\mu_{\mathrm{t}}\varepsilon_{\mathrm{t}}k_0^2=0 \tag{2.12}$$

In our case, where the Fakir's bed of nails consists of non-magnetic materials and the permittivity is given by (2.1), the dispersion equations (2.11), (2.12) reduce to [9, 14]

$$k_x^2+k_z^2=\varepsilon_{yy}\big(k_{\mathrm{h}}^2-k_y^2\big)\Rightarrow k^2=k_{\mathrm{h}}^2-k_{\mathrm{p}}^2\qquad\mathrm{TM}^y\ \text{mode} \tag{2.13}$$

$$k^2=k_{\mathrm{h}}^2\qquad\mathrm{TE}^y\ \text{mode} \tag{2.14}$$

where $k^2=\mathbf{k}\cdot\mathbf{k}$

2.2 Additional Boundary Conditions

Let us now assume that a plane wave with wavevector $\mathbf{k}_{\text{inc}} = \mathbf{k}_{\parallel} + k_y \mathbf{u}_y$, where $\mathbf{k}_{\parallel} = (k_x, 0, k_z)$ lies on the x-z plane and is the component of the wavevector that is parallel with respect to the interface of the textured surface, impinges on the wire medium. For a propagating wave, as shown in Fig. 2.1(b), $\mathbf{k}_{\parallel}$ can be expressed as $k_{\parallel} = k_0 \sin\vartheta$, where $k_0 = \omega/c$. Additionally, the y-component of the wavevector in the air side can be written as $k_y = -j\gamma_0 = -j\sqrt{k_{\parallel}^2 - k_0^2}$, where γ_0 is the propagation constant in free space. When the incident wave is TE^y polarized, it does not interact with the pins – as can be seen from (2.14) – and hence the wire medium behaves like a dielectric slab with relative permittivity ε_{h}.

Indeed, if the incoming electric field is of the form of $\mathbf{E} = e^{\gamma_0 y} e^{-jk_z z}\mathbf{u}_x$, it can be written as

$$E_x = \begin{cases} \left(e^{\gamma_0 y} + R^{\text{TE}} e^{-\gamma_0 y}\right) e^{-jk_z z} & y > 0 \\ \left(A_{\text{TE}}^{+} e^{-\gamma_{\text{TE}} y} + A_{\text{TE}}^{-} e^{\gamma_{\text{TE}} y}\right) e^{-jk_z z} & -L < y < 0 \end{cases} \tag{2.15}$$

where $\gamma_{\text{TE}} = \sqrt{k_{\parallel}^2 - k_{\text{h}}^2}$ is the propagation constant of the TE^y mode, R^{TE} is the reflection coefficient for the electric field and $\text{A}_{\text{TE}}^{\pm}$ is the amplitude of the electric field inside the dielectric slab. Now the magnetic field can be calculated from the expression $\mathbf{H} = \dfrac{j}{\omega\mu}\nabla \times \mathbf{E}$ if the following boundary conditions are taken into account

$$\mathbf{u}_y \times \left(\mathbf{E}_{\text{air}} - \mathbf{E}_{\text{wire medium}}\right)\Big|_{y=0} = 0 \Rightarrow E_x(y=0)\Big|_{\text{wire medium}} - E_x(y=0)\Big|_{\text{air}} = 0 \tag{2.16}$$

$$\mathbf{u}_y \times \left(\mathbf{H}_{\text{air}} - \mathbf{H}_{\text{wire medium}}\right)\Big|_{y=0} = 0 \Rightarrow H_z(y=0)\Big|_{\text{wire medium}} - H_z(y=0)\Big|_{\text{air}} = 0 \tag{2.17}$$

$$\mathbf{u}_y \times \mathbf{E}_{\text{wire medium}}\Big|_{y=-L} = 0 \Rightarrow E_z(y=-L) = 0 \tag{2.18}$$

which imply the continuity of the electric and magnetic fields at the air-wire medium interface and that the electric field vanishes at a PEC interface. Thus, the following 3 $\times$ 3 linear system can be obtained.

$$\begin{bmatrix} -1 & 1 & 1 \\ \gamma_0 & -\gamma_{\text{TE}} & \gamma_{\text{TE}} \\ 0 & e^{\gamma_{\text{TE}} L} & e^{-\gamma_{\text{TE}} L} \end{bmatrix} \begin{bmatrix} R^{\text{TE}} \\ A_{\text{TE}}^{+} \\ A_{\text{TE}}^{-} \end{bmatrix} = \begin{bmatrix} 1 \\ \gamma_0 \\ 0 \end{bmatrix} \tag{2.19}$$

The reflection coefficient R^{TE} can be found as

$$R^{\text{TE}} = -\frac{\gamma_{\text{TE}} - \gamma_0 \tanh\left(\gamma_{\text{TE}} L\right)}{\gamma_{\text{TE}} + \gamma_0 \tanh\left(\gamma_{\text{TE}} L\right)} = -\frac{\sqrt{k_{\text{h}}^2 - k_{\parallel}^2} + j\sqrt{k_{\text{h}}^2 - k_{\parallel}^2}\tan\left(\sqrt{k_{\text{h}}^2 - k_{\parallel}^2} L\right)}{\sqrt{k_{\text{h}}^2 - k_{\parallel}^2} - j\sqrt{k_{\text{h}}^2 - k_{\parallel}^2}\tan\left(\sqrt{k_{\text{h}}^2 - k_{\parallel}^2} L\right)} \tag{2.20}$$

$$A_{\text{TE}}^{+} = -\frac{\gamma_0}{\gamma_{\text{TE}}\cosh(\gamma_{\text{TE}} L) + \gamma_0 \sinh(\gamma_{\text{TE}} L)} = -\frac{\gamma_0 \text{sech}(\gamma_{\text{TE}} L)}{\gamma_{\text{TE}} + \gamma_0 \tanh(\gamma_{\text{TE}} L)} \tag{2.21}$$

$$A_{\text{TE}}^{-} = \frac{\gamma_0\left[1 + \tanh(\gamma_{\text{TE}} L)\right]}{\gamma_{\text{TE}} + \gamma_0 \tanh(\gamma_{\text{TE}} L)} \tag{2.22}$$

and the surface impedance that the incoming wave sees can be written as

$$Z_{\text{s}}^{\text{TE}} = -\frac{E_x(y=0)}{H_z(y=0)}\Big|_{\text{air}} = \frac{j\eta_0 k_0}{\gamma_{\text{TE}}}\tanh\left(\gamma_{\text{TE}} L\right) = \frac{j\eta_0 k_0}{\sqrt{k_{\text{h}}^2 - k_{\parallel}^2}}\tan\left(\sqrt{k_{\text{h}}^2 - k_{\parallel}^2} L\right) \tag{2.23}$$

On the other hand, a TM^y polarized wave excites both the TEM^y and TM^y mode inside the wire medium because it induces a current that flows along the pins. For example, if for simplicity the incoming magnetic field is assumed to be $\mathbf{H} = e^{\gamma_0 y} e^{-jk_z z}\mathbf{u}_x$ and taking into account that $\mathbf{k}_\parallel$ is preserved along the y-direction, the magnetic field in all space is given by the following expression [13]

$$H_x = \begin{cases} \left(e^{\gamma_0 y} + R^{\mathrm{TM}} e^{-\gamma_0 y}\right) e^{-jk_z z} & y > 0 \\ \left(A^{+}_{\mathrm{TEM}} e^{-jk_h y} + A^{-}_{\mathrm{TEM}} e^{jk_h y} + A^{+}_{\mathrm{TM}} e^{-\gamma_{TM} y} + A^{-}_{\mathrm{TM}} e^{\gamma_{TM} y}\right) e^{-jk_z z} & -L < y < 0 \end{cases} \tag{2.24}$$

where $\gamma_{\mathrm{TM}} = \sqrt{k_{\mathrm{p}}^2 + k_\parallel^2 - k_{\mathrm{h}}^2}$ is the propagation constant of the TM^y mode, R^{TM} is the reflection coefficient for the magnetic field and $\mathrm{A}^{\pm}_{\mathrm{TEM}}$, $\mathrm{A}^{\pm}_{\mathrm{TM}}$ are the amplitudes of the supported TEM^y and TM^y modes. As can be easily seen, (2.24) has five unknowns but the classical boundary conditions, (2.16)-(2.18) are only three and thus insufficient to solve this problem. Therefore, additional boundary conditions need to be considered in order to determine all the unknowns.

However, before the derivation of the new boundary conditions is presented, a brief outline of some fundamental homogenization concepts is given [12]. The microscopic electric and magnetic fields $(\mathbf{e}, \mathbf{h})$ inside the wire medium verify Maxwell's equations

$$\nabla \times \mathbf{e} = -j\omega\mu\mathbf{h} \tag{2.25}$$

$$\nabla \times \mathbf{h} = j\omega\varepsilon\mathbf{e} + \mathbf{J}_d \tag{2.26}$$

and have the Floquet property [24]. This means that the electric and magnetic field are periodic along the directions in which the microstructured material is assumed to be infinite. In our case, $(\mathbf{e}, \mathbf{h})e^{j\mathbf{k}_\parallel \cdot \mathbf{r}}$ is periodic inside the wire medium so the transverse (with respect to the plane normal to the orientation of the pins) average (TA) fields can be defined as [12]

$$\mathbf{E}^{\mathrm{T}}_{\mathrm{av}}(y) = \frac{1}{A_{\mathrm{cell}}} \int\limits_{\Omega_{\mathrm{T}}} \mathbf{e}(\mathbf{r}) e^{j\mathbf{k}_\parallel \cdot \mathbf{r}} dxdz \tag{2.27}$$

$$\mathbf{H}^{\mathrm{T}}_{\mathrm{av}}(y) = \frac{1}{A_{\mathrm{cell}}} \int\limits_{\Omega_{\mathrm{T}}} \mathbf{h}(\mathbf{r}) e^{j\mathbf{k}_\parallel \cdot \mathbf{r}} dxdz \tag{2.28}$$

where A_{cell} is the area of Ω_{T} (for a square lattice $A_{\mathrm{cell}} = a^2$). To this end, it is important to note that the TA fields represent macroscopic quantities rather than microscopic ones, so starting from (2.25)-(2.26) the expressions for the macroscopic fields are obtained

$$\left(\nabla_\parallel + \frac{\partial}{\partial y}\mathbf{u}_y\right) \times \mathbf{e} e^{j\mathbf{k}_\parallel \cdot \mathbf{r}} = -j\omega\mu\mathbf{h} e^{j\mathbf{k}_\parallel \cdot \mathbf{r}} \tag{2.29}$$

$$\left(\nabla_\parallel + \frac{\partial}{\partial y}\mathbf{u}_y\right) \times \mathbf{h} e^{j\mathbf{k}_\parallel \cdot \mathbf{r}} = j\omega\varepsilon_{\mathrm{h}}\mathbf{e} e^{j\mathbf{k}_\parallel \cdot \mathbf{r}} + \mathbf{J}_d e^{j\mathbf{k}_\parallel \cdot \mathbf{r}} \tag{2.30}$$

where $\nabla_\parallel = \dfrac{\partial}{\partial x}\mathbf{u}_x + \dfrac{\partial}{\partial z}\mathbf{u}_z$. Integrating (2.29)-(2.30) over Ω_{T} and using (2.27)-(2.28) the following two expressions for the macroscopic fields are obtained [12]

$$\left(-j\mathbf{k}_\parallel + \frac{\partial}{\partial y}\mathbf{u}_y\right) \times \mathbf{E}^{\mathrm{T}}_{\mathrm{av}} = -j\omega\mu\mathbf{H}^{\mathrm{T}}_{\mathrm{av}} \tag{2.31}$$

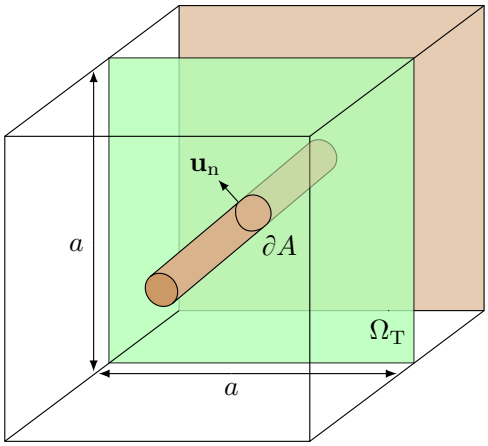


Figure 2.2: Geometry of a unit cell. The Fakir's bed of nails is periodic along the plane Ω_T.

$$\left(-j\mathbf{k}_{\parallel} + \frac{\partial}{\partial y}\mathbf{u}_y \right) \times \mathbf{H}_{av}^{T} = j\omega\varepsilon_h(y)\mathbf{E}_{av}^{T} + \mathbf{J}_{d,av}(y) \tag{2.32}$$

where $\mathbf{J}_{d,av}$ is defined by [12]

$$\mathbf{J}_{d,av}(y) = \frac{1}{A_{cell}} \int_{\partial A} \mathbf{J}_c(\mathbf{r}) e^{j\mathbf{k}_{\parallel}\cdot\mathbf{r}} \frac{1}{|\mathbf{u}_n \times \mathbf{u}_z|} d\ell \tag{2.33}$$

where ∂A, $\mathbf{u}_n$ are shown in Fig. 2.2 and the current $\mathbf{J}_c$ is given by the boundary condition $\mathbf{u}_n \times \mathbf{h} = \mathbf{J}_c$. From (2.31)-(2.32) one observes that the components of the fields along the y-direction (normal components) are continuous when the tangential TA fields are continuous, so at the free space-wire medium interface the following two conditions hold [12].

$$\mathbf{u}_y \cdot \left(\mathbf{H}_{av}^{T}(y=0)\Big|_{\text{wire medium}} - \mathbf{H}_{av}^{T}(y=0)\Big|_{\text{air}} \right) = 0 \tag{2.34}$$

$$\mathbf{u}_y \cdot \left(\varepsilon_h \mathbf{E}_{av}^{T}(y=0) + \frac{\mathbf{J}_{d,av}(y=0)}{j\omega}\Big|_{\text{wire medium}} - \mathbf{E}_{av}^{T}(y=0) - \frac{\mathbf{J}_{d,av}(y=0)}{j\omega}\Big|_{\text{air}} \right) = 0 \tag{2.35}$$

It is important to note that the current flowing on the pins surface along the y-direction should vanish at $y = 0$ since the air side has zero conductivity. In other words, $\mathbf{u}_y \cdot \mathbf{J}_{d,av}(y=0) = 0$. This means that (2.35) is reduced to [12]

$$\mathbf{u}_y \cdot \left(\varepsilon_h \mathbf{E}_{av}^{T}(y=0)\Big|_{\text{wire medium}} - \mathbf{E}_{av}^{T}(y=0)\Big|_{\text{air}} \right) = 0 \tag{2.36}$$

However, (2.24) is still undetermined because one more boundary condition is needed. So far, only the behaviour at the air interface has been analyzed. To this end, the effects taking place at the PEC interface [13] are studied. It is well known, that the electric field does not have any tangential components at a PEC boundary. Thus, assuming that the pins are perfect conductors, the electric field verifies the conditions $\mathbf{e} \cdot \mathbf{u}_y$ (pins side) and $\mathbf{e} \cdot \mathbf{u}_x$, $\mathbf{e} \cdot \mathbf{u}_z$ (ground plane side), so $\mathbf{e} = 0$ at the PEC interface. Moreover, the surface charge density ϱ_s on an arbitrary pin is given by $\varepsilon_0\varepsilon_h \mathbf{e} \cdot \mathbf{u}_n = \varrho_s$. This relation implies that the surface charge density should be zero at the PEC interface since the electric field is zero.

Next, assuming that the pins are very thin and taking into account the continuity equation $\nabla \cdot \mathbf{J}_c = -j\omega\varrho_s$, a relation between the microscopic current $\mathbf{J}_c$ and the TA fields can be established.

Within the thin wire approximation, the current is flowing along the y-direction which means that $\varrho_{\mathrm{s}} = -\dfrac{1}{j\omega}\dfrac{d(\mathbf{J}_{\mathrm{c}}\cdot\mathbf{u}_y)}{d\ell}$, where ℓ is the length along the pin. As can be seen, the charge vanishes only when $\dfrac{d(\mathbf{J}_{\mathrm{c}}\cdot\mathbf{u}_y)}{d\ell} = 0$. Starting from the fact that the current is distributed uniformly over the cross section of the pins, i.e. $\mathbf{J}_{\mathrm{c}} = \dfrac{I(y)}{2\pi r_0}e^{-j\mathbf{k}_{\parallel}\cdot\mathbf{r}}\mathbf{u}_z$, where I is the current along the pin and using (2.33) one gets $\mathbf{J}_{\mathrm{d,av}}(y) = \dfrac{1}{a^2}I(y)\mathbf{u}_y$. Solving for $I(y)$ and substituting $I(y)$ into the expression for $\mathbf{J}_{\mathrm{c}}$ we obtain [13]

$$J_{\mathrm{c},y} = \frac{a^2}{2\pi r_0}e^{-j\mathbf{k}_{\parallel}\cdot\mathbf{r}}\mathbf{J}_{\mathrm{d,av}}(y)\cdot\mathbf{u}_y \tag{2.37}$$

where $r = \ell\mathbf{u}_y$. Thus, in order $\dfrac{dJ_{\mathrm{c},y}}{d\ell} = 0$ to be verified, an additional boundary condition at the PEC interface of the form [13]

$$\Big(-j\mathbf{k}_{\parallel} + \mathbf{u}_y\frac{d}{dy}\Big)\cdot\mathbf{u}_y\mathbf{u}_y\cdot\mathbf{J}_{\mathrm{d,av}} = 0 \tag{2.38}$$

needs to be considered. Using (2.32), (2.38) can also be written as [13]

$$\begin{aligned}\frac{d}{dy}\Big[\omega\varepsilon_0\varepsilon_{\mathrm{h}}\mathbf{u}_y\cdot\mathbf{E}^{\mathrm{T}}_{\mathrm{av}}(y=-L) + \mathbf{u}_y\times\mathbf{k}_{\parallel}\cdot\mathbf{H}^{\mathrm{T}}_{\mathrm{av}}(y=-L)\Big] = 0 \Rightarrow \\ k_0\varepsilon_{\mathrm{h}}\frac{dE_y}{dy}\bigg|_{y=-L} - k_{\parallel}\eta_0\frac{dH_x}{dy}\bigg|_{y=-L} = 0\end{aligned} \tag{2.39}$$

Putting all these together, and using (2.16)-(2.18), (2.24), (2.36), (2.39) the original scattering problem can now be solved analytically. Of course, since we are primarily interested in the reflection coefficient R^{TM}, (2.24) can be simplified further by taking into account that the tangential components of each one of the TE^y, TM^y and TEM^y modes vanish independently at the PEC boundary [14]. This is because of the symmetric structure of the Fakir's bed of nails. Having this in mind, (2.24) can be written in the form [14]

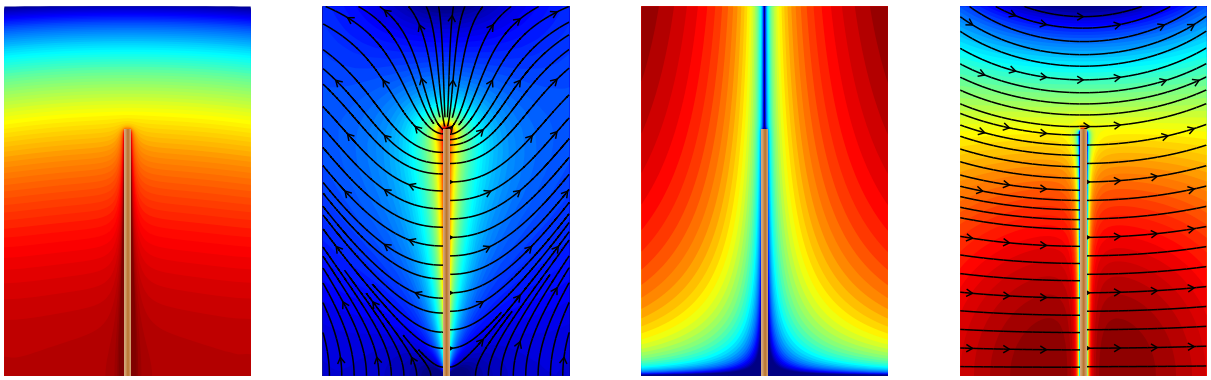
$$H_x = \begin{cases}\Big(e^{\gamma_0 y} + R^{\mathrm{TM}}e^{-\gamma_0 y}\Big)e^{-jk_z z} & y > 0 \\ \Big[A_{\mathrm{TEM}}\cos\Big(\big(y+L\big)k_h\Big) + A_{\mathrm{TM}}\cosh\Big(\big(y+L\big)\gamma_{\mathrm{TM}}\Big)\Big]e^{-jk_z z} & -L < y < 0\end{cases} \tag{2.40}$$

As a consequence, (2.40) and the boundary conditions (2.16),(2.17),(2.36) yield to the following block of equations [14].

$$\begin{bmatrix} 1 & -\cos\big(k_{\mathrm{h}}L\big) & -\cosh\big(\gamma_{\mathrm{TM}}L\big) \\ -\gamma_0 & -\dfrac{k_{\mathrm{h}}}{\varepsilon_{\mathrm{h}}}\sin\big(k_{\mathrm{h}}L\big) & -\dfrac{\gamma_{\mathrm{TM}}}{\varepsilon_{\mathrm{h}}}\sinh\big(k_{\mathrm{h}}L\big) \\ \gamma_0^2 + k_0^2 - k_{\mathrm{h}}^2 & k_{\mathrm{h}}^2\cos\big(k_{\mathrm{h}}L\big) & -\gamma_{\mathrm{TM}}^2\cosh\big(\gamma_{\mathrm{TM}}L\big)\end{bmatrix}\begin{bmatrix} R^{\mathrm{TM}} \\ A_{\mathrm{TEM}} \\ A_{\mathrm{TM}}\end{bmatrix} = \begin{bmatrix} -1 \\ -\gamma_0 \\ -\gamma_0^2 - k_0^2 + k_{\mathrm{h}}^2\end{bmatrix} \tag{2.41}$$

From the expression above, the reflection coefficient can be calculated straightforward and is equal to

$$R^{\mathrm{TM}} = -\frac{k_{\mathrm{h}}k_{\mathrm{p}}^2\tan\big(k_{\mathrm{h}}L\big) - k_{\parallel}^2\gamma_{\mathrm{TM}}\tanh\big(\gamma_{\mathrm{TM}}L\big) + \varepsilon_{\mathrm{h}}\gamma_0\big(k_{\mathrm{p}}^2 + k_{\parallel}^2\big)}{k_{\mathrm{h}}k_{\mathrm{p}}^2\tan\big(k_{\mathrm{h}}L\big) - k_{\parallel}^2\gamma_{\mathrm{TM}}\tanh\big(\gamma_{\mathrm{TM}}L\big) - \varepsilon_{\mathrm{h}}\gamma_0\big(k_{\mathrm{p}}^2 + k_{\parallel}^2\big)} \tag{2.42}$$



(a) (b) (c) (d)

Figure 2.3: Field distributions for a TM and TE polarized incoming wave. (a) H_x and (b) $\mathbf{E}$ distributions for TM polarization. (c) E_x and (d) $\mathbf{H}$ distributions for TE polarization. The parameters are: $r_0/a = 0.01$, $L = a$, $\theta = 45^{\text{o}}$ and $k_0 a = 1.05$.

In order to get better insight in the behaviour of the Fakir's bed of nails, the fields for both polarizations are shown in Fig. 2.3. As can be seen, the bed of nails interacts only with a parallel polarized incoming wave whereas, for perpendicular polarization it behaves like a dielectric slab backed by a ground plane.

2.3 Equivalent Surface Impedance

In this section attempt to study the cases in which a local model for the relative permittivity $\bar{\bar{\varepsilon}}_{\text{r}}$ can be used is presented. Let us assume that the Fakir's bed of nails consists of pins that are packed very densely, so that $\dfrac{L}{a} \gg 1$. In this case, the wire medium can be seen as a medium with extreme anisotropy described by a relative permittivity of the form [9, 14]

$$\bar{\bar{\varepsilon}}_{\text{r}} = \varepsilon_{\text{h}}\big(\mathbf{u}_x\mathbf{u}_x + \varepsilon_{yy}\mathbf{u}_y\mathbf{u}_y + \mathbf{u}_z\mathbf{u}_z\big) \quad \text{where} \quad \varepsilon_{yy} \to \infty \tag{2.43}$$

This suggests that spatial dispersion effects can be neglected and the propagating along the pins TEM^y mode sees an infinite permittivity. With a TEM^y mode, $k_y^2 = k_{\text{h}}^2$ and therefore, from (2.1) $\varepsilon_{yy} \to \infty$ so that $E_y = 0$ and D_y is finite. Under these circumstances, the metamaterial can be treated as an impedance boundary, as described in [7]. For densely packed pins, (2.42) reduces to

$$R^{\text{TM}} \simeq -\frac{k_{\text{h}} \tan\big(k_{\text{h}}L\big) + \varepsilon_{\text{h}}\gamma_0}{k_{\text{h}} \tan\big(k_{\text{h}}L\big) - \varepsilon_{\text{h}}\gamma_0} \tag{2.44}$$

because when $a \to 0$ (and r_0/a is constant – the model is valid for $a \to 0$ as long as r_0/a is constant), from the definition of k_{p} and the propagation constant γ_{TM} follows that $k_{\text{p}} \to \infty$ and $\gamma_{\text{TM}} \to k_{\text{p}}$.

At a generic surface that can be described using the surface impedance concept, the boundary condition (Leontovich boundary condition) [20, 25]

$$\mathbf{E} \times \mathbf{u}_{\text{n}} = Z_{\text{s}}\big(\mathbf{u}_{\text{n}} \times \mathbf{H}\big) \times \mathbf{u}_{\text{n}} \tag{2.45}$$

holds, where Z_{s} is the surface impedance and $\mathbf{u}_{\text{n}}$ is the unit normal vector pointing towards the free-space side (in our case $\mathbf{u}_{\text{n}} = \mathbf{u}_y$). For the geometry shown in Fig. 2.1, (2.45) reads

$$Z_{\text{s}}^{\text{TM}} = -\frac{E_z(y=0)}{H_x(y=0)}\bigg|_{\text{air}} = j\eta_0\frac{\gamma_0}{k_0}\Big(\frac{R^{\text{TM}}-1}{R^{\text{TM}}+1}\Big) = j\eta_0\frac{1}{\sqrt{\varepsilon_{\text{h}}}}\tan\big(k_{\text{h}}L\big) \tag{2.46}$$

where the electric field $\mathbf{E}$ can be calculated from Ampere's law $\mathbf{E} = \frac{1}{j\omega}\bar{\bar{\varepsilon}}_{\mathrm{r}}^{-1}\cdot\nabla\times\mathbf{H}$ with $\bar{\bar{\varepsilon}}_{\mathrm{r}}^{-1} = \frac{1}{\varepsilon_{\mathrm{h}}}\Big(\mathbf{u}_x\mathbf{u}_x+\frac{1}{\varepsilon_{yy}}\mathbf{u}_y\mathbf{u}_y+\mathbf{u}_z\mathbf{u}_z\Big)$ What is remarkable in (2.46) is that the surface impedance is independent of the incident angle of the incoming electromagnetic wave. Of course, this property is valid only in the limit case in which the pins are arranged very densely and hence the spatial dispersion can be neglected.

In the analysis presented thus far, the pins were assumed lossless (i.e., PEC). Although this is a very good approximation at microwave frequencies some further discussion is required to demonstrate its range of applicability. As has already been shown, the relative permittivity of the metal pins is given by

$$\varepsilon_{\mathrm{m}} = 1 + \frac{\sigma}{j\omega\varepsilon_0} \tag{2.47}$$

which, in the microwave spectrum, can be re-written as

$$\varepsilon_{\mathrm{m}} = 1 + \frac{2}{j\big(k_0\delta\big)^2} \tag{2.48}$$

where $\delta = \sqrt{\frac{2}{\omega\mu_0\sigma}}$ is the skin depth. In general, in the case of lossy metal pins the effective homogenized permittivity along the y-direction can be written as [10]

$$\varepsilon_{yy}(\omega,k_y) = 1 + \frac{1}{\frac{\varepsilon_{\mathrm{h}}}{(\varepsilon_{\mathrm{m}}-\varepsilon_{\mathrm{h}})f_V} - \frac{k_{\mathrm{h}}^2-k_y^2}{k_{\mathrm{p}}^2}} \tag{2.49}$$

where $f_V = \pi\Big(\frac{r_0}{a}\Big)^2$ is the volume fraction of the pins (describing the volume occupied by the pin within the unit cell). It is interesting to note that (2.49) reduces to (2.1) in the case of PEC pins (i.e., $\varepsilon_{\mathrm{m}}\to-\infty$). With finite conductivity pins, the TEM$^{\mathrm{y}}$ mode (supported by PEC pins) is converted to a quasi-TEM$^{\mathrm{y}}$ mode with a dispersion relation of the form $k_y = k_y(\omega,k_\parallel)$ [10, 31]. As can be seen, the quai-TEM$^{\mathrm{y}}$ mode is dispersive as it depends on $k_\parallel$ and hence, the phase velocity along the pin axis depends on the phase shift on the transverse to the pins plane. As a result, the losses can be neglected only when this dependence can be neglected [14]. Therefore, in order to evaluate the level of dependence, the parameter $\frac{k_y(\omega,k_\parallel=\infty)}{k_y(\omega,k_\parallel=0)}$ can be introduced as a means to quantify the dependence of k_y on $k_\parallel$ [14]. Thus, taking into account (2.48) the following relation has to be close to unity in order to neglect losses [14]

$$\frac{k_y(\omega,k_\parallel=\infty)}{k_y(\omega,k_\parallel=0)} \simeq \frac{\sqrt{k_{\mathrm{h}}^2+k_{\mathrm{c}}^2}}{k_{\mathrm{h}}} = \sqrt{1-j\frac{(k_{\mathrm{p}}a)^2}{2\pi}\Big(\frac{\delta}{r_0}\Big)^2} \tag{2.50}$$

where $k_{\mathrm{c}}^2 = -\frac{\varepsilon_{\mathrm{h}}k_{\mathrm{p}}^2}{(\varepsilon_{\mathrm{m}}-\varepsilon_{\mathrm{h}})f_V}$. It is clear, that losses can be neglected only when $\frac{\delta}{r_0}\ll 1$ [14].

It is interesting to note that the accuracy of the previous homogenization approach is higher when $k_0a\ll\pi$ and $k_\parallel a\ll\pi$ [14]. Also, when the pin radius diverges from the thin wire approximation, the permittivity in the transverse to the pins plane needs to be corrected to take into account the polarization effects in this plane and can be written as [10]

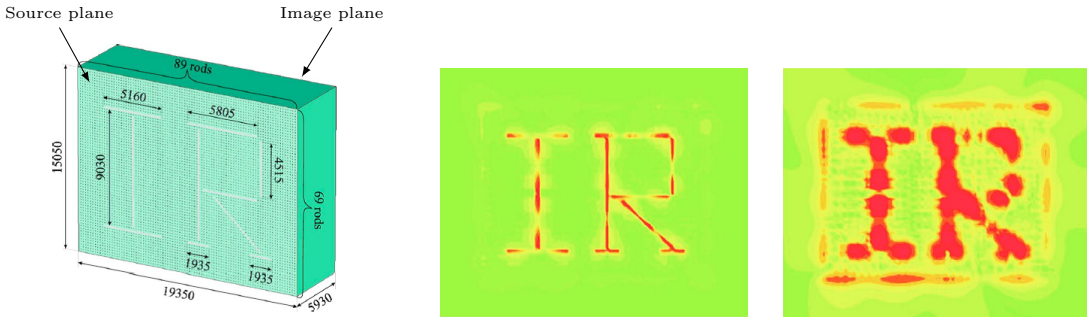
$$\varepsilon_{xx} = \varepsilon_{zz} = 1 + \frac{2}{\frac{1}{f_V}\frac{\varepsilon_{\mathrm{m}}+\varepsilon_{\mathrm{h}}}{\varepsilon_{\mathrm{m}}-\varepsilon_{\mathrm{h}}} - 1} \tag{2.51}$$

With thicker pins charge can be accumulated at the tip of the pins and hence, the additional boundary condition at the air-wire medium interface needs to be modified as explained in [16, 17]. However, the accuracy of the simple model presented here is good for most practical applications, as shown in Chapter 3.

2.4 Applications

With wire media forming the basic ingredient for many other metamaterials [26] and impedance surfaces [27–29], together with their extraordinary electromagnetic properties, led to an explosion in new applications. Based on the previous analytical model, various practical applications of the "Fakir's bed of nails" are discussed here. For example, lenses for near-field sub-wavelength imaging, based either on the conversion of free-space evanescent fields into propagating waves within the wire medium (i.e., operation in the canalization region) [30–37] or amplification of evanescent field components [38], are commonly used to overcome the diffraction limit. The physics in the latter case has already been discussed in Chapter 1. However, with a wire medium operating in the canalization region, sub-wavelength resolution is obtained by a fundamentally different physical mechanism; the conversion of the near-field evanescent waves into propagating waves within the wire medium slab [30]. As has already been shown, a parallel polarized incoming wave excites two modes within the wire medium, a TEM^y and a TM^y mode. The wavevector associated with the TM^y mode is $k_y = -j\gamma_{\mathrm{TM}} = -j\sqrt{k_{\mathrm{p}}^2 + k_{\parallel}^2 - k_{\mathrm{h}}^2}$ which describes an evanescent mode when $k_{\mathrm{h}} < k_{\mathrm{p}}$ for all real k_y. Similarly, in the air side the incident wave has a wavevector $k_y = -j\gamma_0 = \sqrt{k_{\parallel}^2 - k_0^2}$ which corresponds to a propagating mode in free space when $k_{\parallel} < k_0$ and to an evanescent mode when $k_{\parallel} > k_0$ (i.e., sub-wavelength spatial spectrum) [30]. On the other hand, the TEM^y is always a propagating mode and hence, the evanescent spectrum in free space is converted into propagating TEM waves within the wire medium. As a result, the evanescent near-field components are canalized through the wire medium to the image plane to reconstruct a super-resolved image. In Fig. 2.4, the electric field distributions are shown for such an imaging device. It should be emphasized that this behaviour can be obtained only for parallel polarization, since a perpendicular polarized wave does not excite the TEM^y mode, as has already been explained. It is clear that for such applications the wire medium is used without a ground plane so that the incoming waves can be transmitted through the wire medium. However, recently a new concept was presented employing the Fakir's bed of nails as a superlens, based on the internal imaging method [34], as shown in Fig. 2.5. In this case the length of the pins is half compared to the device shown in Fig. 2.4. The principle of operation is similar to the method of images where the ground plane acts as a mirror.

Moreover, there are cases where the grounded wire medium (or some variations of it) has been used in order to realize artificial high impedance surfaces or perfect magnetic conductors [39]. In [40–45] the Green's functions for a simple structure containing the Fakir's bed of nails are presented and these results are then used to implement artificial magnetic conductors so that wave propagation along specific directions is suppressed. Specifically, the realization of perfect electric conductor/perfect magnetic conductor (PEC/PMC)-walled waveguides is of great interest. For example the ridge-gap waveguide (i.e., parallel-plate waveguide with a ridge, as shown in Fig. 2.6) can be used as an alternative to traditional metal-pipe rectangular waveguide technologies, because of advantages in construction and performance [46–54]. With such a device, the energy is confined along a desired direction (i.e., along the ridge). Here, a quasi-TEM mode is supported along the ridge while being strongly attenuated above the bed of nails region when the pins form an artificial magnetic conductor. The latter is achieved by tuning the surface impedance given by (2.46) to obtain a high impedance surface (i.e., PMC) and hence, the fields decay exponentially away from the ridge along the x-direction.



(a) Geometry of the imaging device **(b)** Distribution of $|E_y|$ at the source plane **(c)** Distribution of $|E_y|$ at the image plane

Figure 2.4: Imaging device realized by the wire medium [31]. The field patterns correspond to the frequency at which highest resolution is obtained (30 THz).

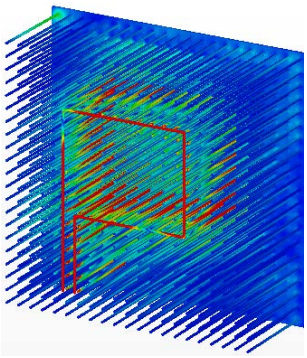
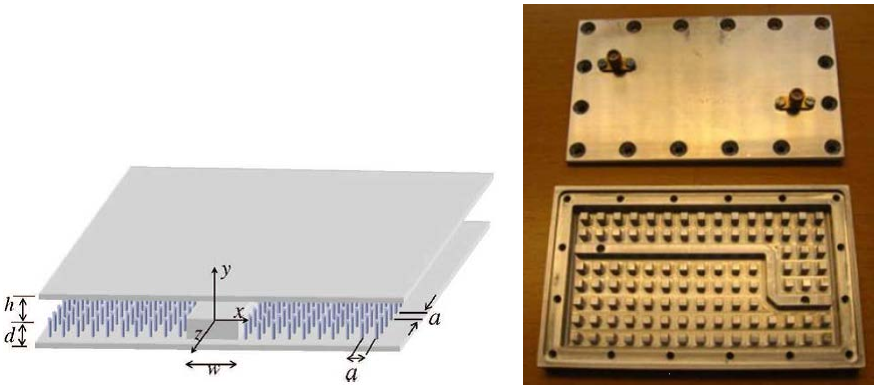


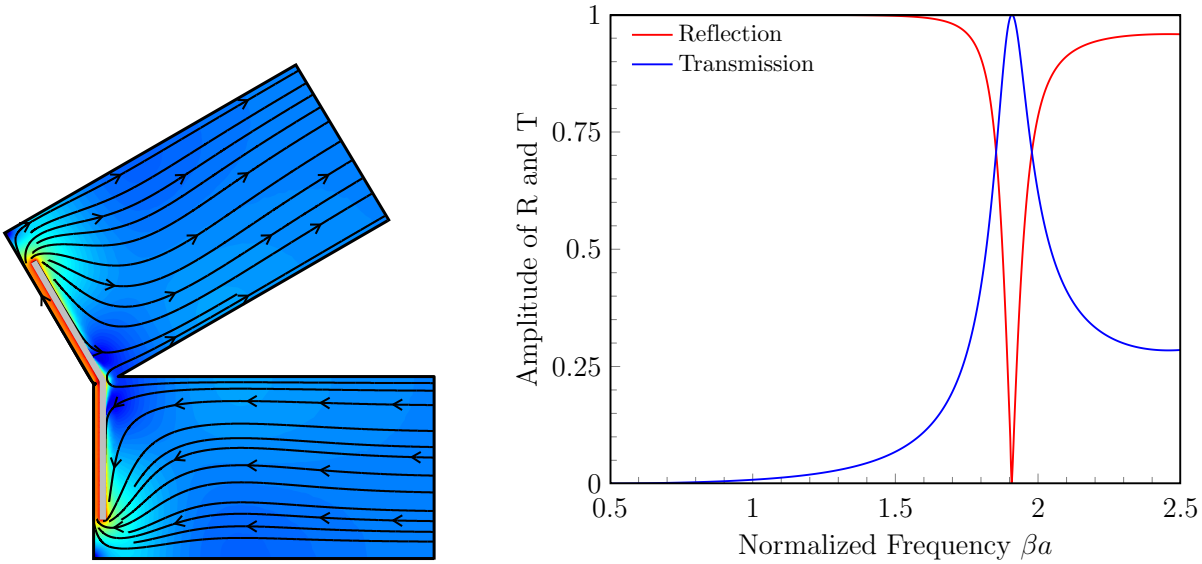
Figure 2.5: Internal imaging using the Fakir's bed of nails.



(a) **(b)**

Figure 2.6: The ridge gap parallel plate waveguide. (a) Perspective view and (b) fabricated prototype. The quasi-TEM mode is confined and propagates along the ridge.

Other applications include the realization of ε near zero (ENZ) material, as shown in Fig. 2.7, where two parallel-plate waveguides are connected to each other with a very narrow channel filled with an ENZ material. The latter one is implemented with an 1D periodic arrangement of pins. As has been discussed previously, the wire medium exhibits a plasma-like behaviour and therefore, by adjusting its length, its effective permittivity can be tuned close to zero over a narrow frequency range. Within this band, power can be tunneled through very thin layers of such media



(a) (b)

Figure 2.7: Parallel-plate waveguide terminated with a thin layer of ε near zero material. (a) Power flow and (b) transmission (blue curve) and reflection (red curve) characteristics.

with minimum reflections [55–57], as shown in Fig. 2.7. Additionally, the realization of negative refraction media [58–60], broadband absorbers [61–63] as well as increased bandwidth backward-wave metamaterials with the use of nanowire arrays [64–67] are further typical applications of the wire medium metamaterial.

2.5 Conclusion

A rigorous electromagnetic characterization of the Fakir’s bed of nails metamaterial has been presented from first principles using homogenization techniques. Spatial dispersion effects have been taken into account and the behaviour of the bed of nails for both polarizations has been studied and the appropriate additional boundary conditions required have been analyzed. Moreover, a simplified model applicable in the limit case of densely packed pin where spatial dispersion effects can be neglected has been presented. Finally, various practical applications based on the Fakir’s bed of nails structure have been discussed exploring its extraordinary properties. Emphasis has given on imaging devices with sub-wavelength resolution and the implementation of high impedance surfaces as two of the most illustrative types of applications. This chapter serves as the foundations for the analysis presented next, where a more general model describing the behaviour of a modified parallel-plate waveguide with both plates replaced by the bed of nails is presented.

References

[1] J. Brown, "Artificial dielectrics with refractive indices less than unity",*Proc. IEE-Part IV: Institution Monographs*, vol. 100, no. 5, pp. 51-62, Oct. 1953

[2] J. Brown and W. Jackson, "The properties of artificial dielectrics at centimetre wavelengths", *Proc. IEE-Part B: Radio and Electronic Engineering*, vol. 102, no. 1, pp. 11-16, Jan. 1955

[3] A. Carne and J. Brown, "Theory of reflections from the rodded-type artificial dielectric",*Proc. IEE-Part B: Radio and Electronic Engineering*, vol. 106, no. 26. pp. 107-114, Mar. 1959

[4] J. S. Seeley and J. Brown, "The use of dispersive artificial dielectrics in a beam-scanning prism", *Proc. IEE-Part B: Radio and Electronic Engineering*, vol. 106, no. 26, pp. 93, Mar. 1959

[5] J. Brown, "Artficial dielectrics", *Progress in dielectrics*, vol. 2, pp. 195-225, 1960

[6] W. Rotman, "Plasma simulation by artificial dielectrics and parallel-plate media", *IRE Trans. Antennas Propag.*, vol. 10, no. 1, pp. 82-95, Jan. 1962

[7] R. King, D. Thiel and K. Park, "The synthesis of surface reactance using an artificial dielectric", *IEEE Trans. Antennas Propag.*, vol. 31, no. 3, pp. 471-476, May 1983

[8] P. A. Belov, S. A. Tretyakov and A. J. Viitanen, "Dispersion and reflection properties of artificial media formed by regular lattices of ideally conducting wires", *Journal of Electromagnetic Waves and Applications*, vol. 16, no. 8, pp. 1153-1170, 2002

[9] P. A. Belov, R. Marqués, S. I. Maslovski, I. S. Nefedov, M. Silveirinha, C. R. Simovski and S. A. Tretyakov, "Strong spatial dispersion in wire media in the very large wavelength limit", *Phys. Rev. B*, vol. 67, no. 11, p. 113103, Mar. 2003

[10] M. G. Silveirinha, "Nonlocal homogenization model for a periodic array of ε-negative rods", *Phys. Rev. E*, vol. 73, no. 4. p. 046612, Apr. 2006

[11] M. G. Silveirinha, "Additional boundary condition for the wire medium", *IEEE Trans. Antennas Propag.*, vol. 54, no. 6, pp. 1766-1780, Jun. 2006

[12] M. G. Silveirinha and C. A. Fernandes, "Transverse-average field approach for the characterization of thin metamaterial slabs", *Phys. Rev. E*, vol. 75, no. 3, p. 036613, Mar. 2007

[13] M. G. Silveirinha, C. A. Fernandes and J. R. Costa, "Additional boundary condition for a wire medium connected to a metallic surface", *New J. Phys.*, vol. 10, no. 5, p. 053011, 2008

[14] M. G. Silveirinha, C. A. Fernandes and J. R. Costa, "Electromagnetic characterization of textured surfaces formed by metallic pins", *IEEE Trans. Antennas Propag.*, vol. 56, no. 2, pp. 405-415, Feb. 2008

[15] S. I. Maslovski and M. G. Silveirinha, "Nonlocal permittivity from a quasistatic model for a class of wire media", *Phys. Rev. B*, vol. 80, no. 24, p. 245101, Dec. 2009

[16] S. I. Maslovski, T. A. Morgado, M. G. Silveirinha, C. S. R. Kaipa and A. B. Yakovlev, "Generalized additional boundary conditions for wire media", *New J. Phys.*, vol. 12, p. 113047, 2010

[17] A. B. Yakovlev, Y. R. Padooru, G. W. Hanson, A. Mafi and S. Karbasi, "A generalized additional boundary condition for mushroom-type and bed-of-nails-type wire media", *IEEE Trans. Microw. Theory Techn.*, vol. 59, no. 3, pp. 527-531, Mar. 2011

[18] S. I. Maslovski, T. A. Morgado, M. G. Silveirinha "The auxiliary source method and its application to the reflection problem at an interface with tilted wires", *URSI Int. Symp. Electr. Theory*, pp. 319-322, 2010

[19] G. W. Hanson, E. Forati, M. G. Silveirinha, "Modeling of spatially dispersive wire media: transport representation, comparison with natural materials, and additional boundary conditions", *IEEE Trans. Antennas Propag.*, vol. 60, pp. 4219-4232, Sept. 2012

[20] S. Tretyakov, "Analytical modeling in applied electromagnetics", *Artech House*, 2003

[21] I. V. Lindell, S. A. Tretyakov, K. I. Nikoskinen and S. Ilvonen, "BW media: media with negative parameters, capable of supporting backward waves", *Microw. Opt. Techn. Lett.*, vol. 31, no. 2, pp. 129-133, Aug. 2001

[22] C. A. Moses and N. Engheta, "Electromagnetic wave propagation in the wire medium: a complex medium with long thin inclusions", *Wave Motion*, vol. 34, no. 3, pp. 301-317, Sep. 2001

[23] I. Lindell, "Methods for electromagnetic field analysis", *Wiley-IEEE Press*, 1996

[24] J. Bladel, "Electromagnetic fields", *Wiley-IEEE Press*, 2007

[25] I. V. Lindell and A. H. Sihvola, "Realization of impedance boundary", *IEEE Trans. Antennas Propag.*, vol. 54, no. 12, pp. 3669-3676, Dec. 2006

[26] R. A. Shelby, D. R. Smith and S. Schultz, "Experimental verification of negative index of refraction",*Science*, vol. 292, no. 5514, pp. 77-79, Apr. 2001

[27] O. Luukkonen, M. G. Silveirinha, A. B. Yakovlev, C. R. Simovski, I. S. Nefedov and S. A. Tretyakov, "Effects of spatial dispersion on reflection from mushroom-type artificial impedance surfaces", *IEEE Trans. Microw. Theory Tech.*, vol. 57, no. 12, pp. 2692-2699, Nov. 2009

[28] A. B. Yakovlev, M. G. Silveirinha, O. Luukkonen, C. R. Simovski, I. S. Nefedov and S. A. Tretyakov, "Characterization of surface-wave and leaky-wave propagation on wire-medium slabs and mushroom structures based on local and nonlocal homogenization models", *IEEE Trans. Microw. Theory Tech.*, vol. 57, pp. 2700-2714, Nov. 2009

[29] C. S. R. Kaipa, A. B. Yakovlev, S. I. Maslovski and M. G. Silveirinha "Mushroom-type high-impedance surface with loaded vias: Homogenization model and ultra-thin design",*IEEE Antenn. Wireless Propagat. Lett.*, vol. 10, pp. 1503-1506, Dec. 2011

[30] P. A. Belov and M. G. Silveirinha, "Resolution of sub-wavelength transmission devices formed by a wire medium", *Phys. Rev. E*, vol. 73, no. 5, p. 056607, May 2006

[31] M. G. Silveirinha, P. A. Belov and C. R. Simovski, "Subwavelength imaging at infrared frequencies using an array of metallic nanorods", *Phys. Rev. B*, vol. 75, no. 3, p. 035108, Jan. 2007

[32] T. A. Morgado and M. G. Silveirinha, "Transport of an arbitrary near-field component with an array of tilted wires", *New J. Phys.*, vol. 11, no. 8, p. 083023, 2009

[33] X. Radu, D. Garray and C. Craeye, "Toward a wire medium endoscope for MRI imaging", *Metamaterials*, vol. 3, no. 2, pp. 90-99, 2009

[34] A. E. Ageyskiy, S. Y. Kosulnikov, S. I. Maslovski, Y. S. Kivshar and P. A. Belov, "Quarter-wavelength nanorod lens based on internal imaging", *Phys. Rev. B*, vol. 85, no.3, p. 033105, Jan. 2012

[35] P. A. Belov, Y. Zhao, S. Tse, P. Ikonen, M. G. Silveirinha, C. R. Simovski, S. Tretyakov, Y. Hao and C. Parini, "Transmission of images with subwavelength resolution to distances of several wavelengths in microwave regime", *Phys. Rev. B*, vol. 77, no. 19, p. 193108, May 2008

[36] P. A. Belov, C. R. Simovski and P. Ikonen, "Canalization of subwavelength images by electromagnetic crystals", *Phys. Rev. B*, vol. 78, no. 19, p. 195121, Nov. 2008

[37] S. Y. Kosulnikov, E. A. Yankovskaya, S. I. Maslovski, P. A. Belov and Y. S. Kivshar "Optimal filling factor of nanorod lenses for subwavelength imaging", *Phys. Rev. A*, vol. 84, no. 6, p. 065801, Dec. 2011

[38] C. S. R. Kaipa, A. B. Yakovlev, S. I. Maslovski and M. G. Silveirinha, "Near-field imaging with a loaded wire medium", *Phys. Rev. B*, vol. 86, no. 15, p. 155103, Oct. 2012

[39] O. Luukkonen, "Artificial impedance surfaces", Ph.D. Thesis, *Helsinki University of Technology*, Dec. 2009

[40] D. Pozar, "Radiation and scattering from a microstrip patch on a uniaxial substrate", *IEEE Trans. Antennas Propag.*, vol. 35, no. 6, pp. 613-621, Jun. 1987

[41] Z. Sipus, H. Merkel, and P.-S. Kildal, "Green's functions for planar soft and hard surfaces derived by asymptotic boundary conditions", *IEE Proc. Microw. Antennas Propag.*, vol. 144, no. 5, pp. 321-328, Oct. 1997

[42] Z. Sipus, M. Bosiljevac and P.-S. Kildal, "Local wave green's functions of parallel plate metamaterial-based gap waveguides with one hard wall", *3rd EuCAP*, pp.37-40, Mar. 2009

[43] M. Bosiljevac, Z. Sipus, and P.-S. Kildal, "Construction of green's functions of parallel plates with periodic texture with application to gap waveguides – a plane-wave spectral-domain approach", *IET Microw. Antennas Propag.*, vol. 4, no. 11, pp. 1799-1810, Nov. 2010

[44] A. Polemi and S. Maci, "Closed form expressions for the modal dispersion equations and for the characteristic impedance of a metamaterial-based gap waveguide", *IET Microw. Antennas Propag.*, vol. 4, no. 8, pp. 1073-1080, Aug. 2010

[45] A. Polemi, S. Maci, and P-S. Kildal, "Approximated closed form characteristic impedance for the bed of nails-based gap waveguide", *4th EuCAP*, pp. 1-3, Apr. 2010

[46] P.-S. Kildal, "Three metamaterial-based gap waveguides between parallel metal plates for mm/submm waves", *3rd EuCAP*, pp. 28-32, Mar. 2009

[47] P.-S. Kildal, E. Alfonso, A. Valero-Nogueira, and E. Rajo-Iglesias, "Local metamaterial-based waveguides in gaps between parallel metal plates", *IEEE Antenn. Wireless Propag. Lett.*, vol. 8, pp. 84-87, 2009

[48] P.-S. Kildal, E. Rajo-Iglesias, E. Alfonso, A. Valero and A. U. Zaman, "Wideband, low loss, low-cost, quasi-tem metamaterial-based local waveguides in air gaps between parallel metal plates. In Electromagnetics in Advanced Applications", *ICEAA*, pp. 588-591, Sep. 2009

[49] P.-S. Kildal and M. N. M. Kehn, "The ridge gap waveguide as a wideband rectangular hard waveguide", *4th EuCAP*, pp. 1-4, Apr. 2010

[50] E. Pucci, A. U. Zaman, E. Rajo-Iglesias, P.-S. Kildal and A. Kishk, "Losses in ridge gap waveguide compared with rectangular waveguides and microstrip transmission lines", *4th EuCAP*, pp. 1-4, Apr. 2010

[51] E. Rajo-Iglesias, A. U. Zaman and P.-S. Kildal, "Parallel plate cavity mode suppression in microstrip circuit packages using a lid of nails", *IEEE Microw. Wireless Components Lett.*, vol. 20, no. 1, pp. 31-33, Jan. 2010

[52] P.-S. Kildal, A. U. Zaman, E. Rajo-Iglesias, E. Alfonso and A. Valero-Nogueira, "Design and experimental verification of ridge gap waveguide in bed of nails for parallel-plate mode suppression", *IET Microw., Antennas Propag.*, vol. 5, no. 3, pp. 262-270, Feb. 2011

[53] A. Polemi, S. Maci and P.-S. Kildal, "Dispersion characteristics of a metamaterial-based parallel-plate ridge gap waveguide realized by bed of nails", *IEEE Trans. Antennas Propag.*, vol. 59, no. 3, pp. 904-913, Mar. 2011

[54] E. Rajo-Iglesias and P.-S. Kildal, "Numerical studies of bandwidth of parallel-plate cut-off realised by a bed of nails, corrugations and mushroom-type electromagnetic bandgap for use in gap waveguides", *IET Microw. Antennas Propag.*, vol. 5, no. 3, pp. 282-289, Feb. 2011

[55] B. Edwards, A. Alu, M. E. Young, M. G. Silveirinha and N. Engheta, "Experimental verification of epsilon-near-zero metamaterial coupling and energy squeezing using a microwave waveguide", *Phys. Rev. Lett.*, vol. 100, no. 3, p. 033903, Jan. 2008

[56] B. Edwards, A. Alu, M. G. Silveirinha and N. Engheta, "Reflectionless sharp bends and corners in waveguides using epsilon-near-zero effects", *J. Appl. Phys.*, vol. 105, p. 044905, Jan. 2009

[57] M. Kashanianfard, "Electromagnetic wave transmission through sub-wavelength channels and bends using metallic wires", *MSc Thesis*, University of Waterloo, Canada, 2009

[58] M. G. Silveirinha, "Broadband negative refraction with a crossed wire mesh", *Phys. Rev. B*, vol. 79, no. 15, p. 153109, Apr. 2009

[59] M. G. Silveirinha and A. B. Yakovlev, "Negative refraction by a uniaxial wire medium with suppressed spatial dispersion", *Phys. Rev. B*, vol. 81, no. 23, p. 233105, Jun. 2010

[60] C. S. R. Kaipa, A. B. Yakovlev, S. I. Maslovski and M. G. Silveirinha, "Indefinite dielectric response and all-angle negative refraction by a structure formed with deeply-subwavelength inclusions", *Phys. Rev. B*, vol. 84, no. 16, p. 165135, Oct. 2011

[61] S. A. Tretyakov and S. I. Maslovski, "Thin absorbing structures for all incidence angles based on the use of a high-impedance surface", *Microw. Opt. Technol. Lett.*, vol. 38, no. 2, pp. 153-157, Jun. 2003

[62] O. Luukkonen, F. Costa, C. R. Simovski, A. Monorchio and S. A. Tretyakov, "A thin electromagnetic absorber for wide incidence angles and both polarizations", *IEEE Trans. Antennas Propag.*, vol. 57, pp. 3119-3124, Oct. 2009

[63] Y. R. Padooru, A. B. Yakovlev, C. S. R. Kaipa, G. W. Hanson, F. Medina, F. Mesa, and A. W. Glisson, "New absorbing boundary conditions and analytical model for multilayered mushroom-type metamaterials: Applications to wideband absorbers", *IEEE Trans. Antennas Propag.*, vol. 60, no. 12, pp. 5727-5742 Dec. 2012

[64] I. S. Nefedov, S. A. Tretyakov, "Effective medium model for two dimensional periodic arrays of carbon nanotubes", *Photonics and Nanostructures – Fundamentals and Applications*, vol. 9, pp. 374-380, Oct. 2011

[65] I. S. Nefedov and S. Tretyakov, "Ultabroadband electromagnetically indefinite medium formed by aligned carbon nanotubes", *Phys. Rev. B*, vol. 84, no. 11, p. 113410, Sep. 2011

[66] A. Demetriadou, J. B. Pendry, "Taming spatial dispersion in wire metamaterials", *J. Phys.: Condens. Matter*, vol. 20, p. 295222, 2008

[67] I. S. Nefedov, "Electromagnetic waves propagating in a periodic array of parallel metallic carbon nanotubes", *Phys. Rev. B*, vol. 82, no. 15, p. 155423, Oct. 2010

Chapter 3

Propagation Characteristics in Fakir's Bed of Nails Metamaterial Waveguides

In this chapter, following the results presented previously, the propagation characteristics of electromagnetic waves in waveguides implemented using the "Fakir's bed of nails" are investigated both analytically and numerically. The classical metal walls of a parallel-plate waveguide are replaced by a Fakir's bed of nails metamaterial having arbitrary pin lengths on both walls; treated as a homogenized effective spatially dispersive dielectric. A modal analysis of the electromagnetic fields is presented and dispersion expressions for the propagating modes are derived analytically and independently validated with full-wave numerical simulations. An equivalent transmission line model is also given and similarities with the classical metal-dielectric-metal structure commonly used in optics are discussed.

3.1 Introduction

Waveguides have been an essential component in almost every system operating across the electromagnetic spectrum, including frequencies from microwaves to terahertz [1–3]. At such wavelengths, their significance becomes even more obvious when considering circuits and subsystems that can be implemented. One of the most widely used guided-wave structure is the parallel-plate waveguide. Its behaviour is well-known and has been studied extensively [4]. Because of its simple geometry, it is used in a variety of applications [5], ranging from terahertz time-domain spectroscopy [6, 7] to lens realization [8].

Here, generalized expressions are derived that describe the behaviour of waveguides with bed of nails walls and thus, existing models expanded to describe more complicated structures used for practical applications. The propagation characteristics in a parallel-plate waveguide with both plates being replaced by the Fakir's bed of nails are studied, both analytically and numerically. The behaviour of such a structure resembles a metal-dielectric-metal structure, where coupling between the interfaces affects the performance; both approaches are compared and contrasted. Various parametric studies, highlighting the general behaviour of the Fakir's bed of nails metamaterial waveguide structure, are also undertaken and an equivalent transmission line model is presented.

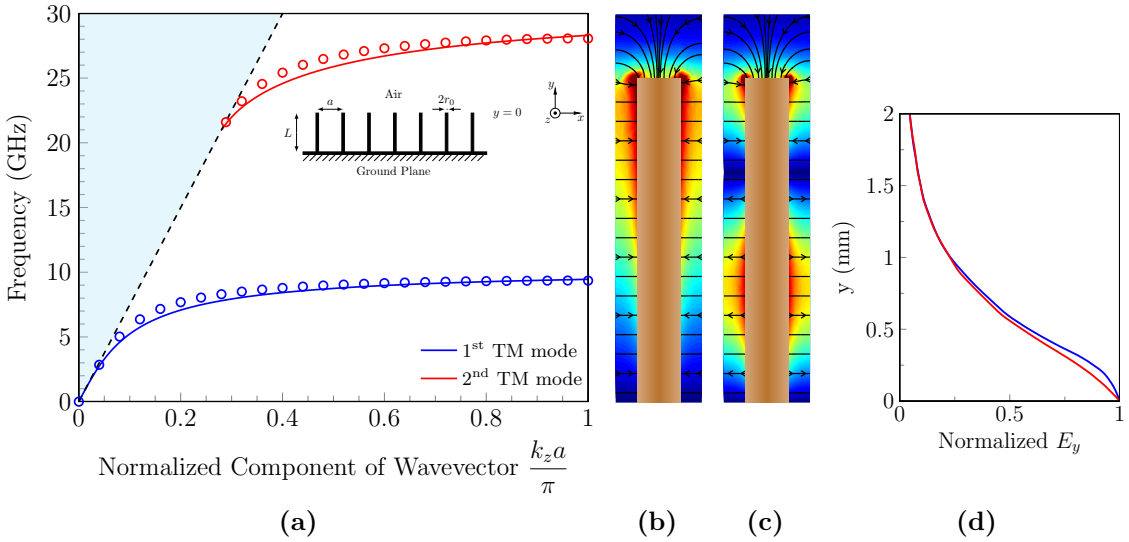


Figure 3.1: (a) Real part of k_z for the Fakir's bed of nails benchmark structure with $L = 7.5$ mm, $r_0 = 0.5$ mm and $a = 2$ mm. Solid lines: analytical model [9]. Discrete symbols: full-wave numerical simulation results obtained using HFSS$^{\text{TM}}$. The light line is plotted with a dashed line. (b) and (c) Electric field distributions at the pins for $k_z a = \pi$ in the first and second mode, respectively. (d) Electric field E_y at the center of the pins along the air gap. Blue curves correspond to the first mode and red curves to the second mode.

3.2 Analytical Formulation

3.2.1 Plain Fakir's Bed of Nails

A comprehensive electromagnetic analysis of the "Fakir's bed of nails" structure has already been presented in Chapter 2. Here the dispersion characteristics of the surface modes supported by such a structure are presented in greater detail so that better physical insight is obtained. Moreover, this simple geometry is used as a benchmark reference structure for the more general model presented in the following section. As has been shown in Chapter 1, the eigenmodes of the "Fakir's bed of nails" metamaterial can be obtained from the poles in the reflection coefficient (2.42) – for simplicity we use $k_{\|} = k_z$. The dispersion characteristics are shonw in Fig. 3.1, where as can be seen there are solutions only to the right of the light line, corresponding to bound surface waves. This is intuitively expected, since such an open structure cannot normally guide energy in a particular direction, as it is spatially unbounded. Thus, the energy must be guided along the interface in the form of bound surface waves.

3.2.2 Fakir's Bed of Nails Parallel-Plate Waveguide

A conventional parallel-plate waveguide, where both bottom and top metal plates have been replaced by the Fakir's bed of nails metamaterial, is considered as shown in Fig. 3.2. The structure can be treated as a classical parallel-plate waveguide partially filled with a dielectric (wire medium) and partially filled with air and, hence, the propagating modes in general are not TE or TM. Instead they are hybrid modes, which can be characterized as longitudinal section electric (LSE) or longitudinal section magnetic (LSM) modes, respectively.

A complete analysis of these types of modes is presented in [11]. The fundamental wave-guiding

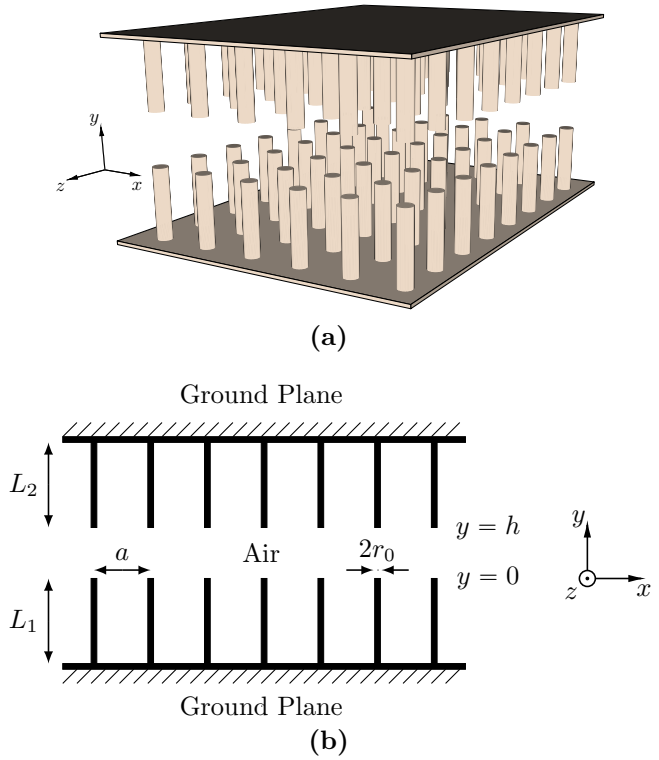


Figure 3.2: Fakir's bed of nails parallel-plate waveguide. (a) Perspective view and (b) side view.

mode is an LSM^y mode ($H_y = 0$) and our derivation of the modal equation for the LSM^y modes will now be given here. A simple way to express the field distributions is by using (2.40) and (2.42). In the air gap between the plates, the magnetic field satisfies the following relation [9]

$$\mathbf{H} \propto (\mathbf{k}_\parallel \times \mathbf{u}_y)\, g\,(y, k_\parallel)\, e^{-j\mathbf{k}_\parallel \cdot \mathbf{r}}, \qquad y > 0 \tag{3.1}$$

where $g\,(y, k_\parallel) = e^{\gamma_0 y} + Re^{-\gamma_0 y}$ and $\mathbf{k}_\parallel = (k_x, 0, k_z)$ is the wavevector parallel to the air-bed of nails interface, $\gamma_0 = \sqrt{k_\parallel^2 - k_0^2}$ is the free-space propagation constant within the gap and R is the reflection coefficient for the magnetic field from the interface at $y = 0$, given by (2.42). As has already been shown [9], (3.1) represents the magnetic field in the air region, taking into account the reflection from the Fakir's bed of nails structure at $y = 0$. Thus, the waveguide modes can be obtained if solutions of the form given in (3.1) are combined and also taking into account the fact that the wave-guiding modes have to satisfy the appropriate boundary conditions at the interfaces at $y = 0$ and $y = h$. For example, the superposition of plane waves with wave vectors (k_x,0,k_z) and ($-k_x$,0,k_z) results in a magnetic field distribution of the form

$$\mathbf{H} = H_0 \left[-\frac{k_z}{k_0}\cos(k_x x), 0, -\frac{jk_x}{k_0}\sin(k_x x) \right] g\,(y, k_\parallel)\, e^{-jk_z z} \tag{3.2}$$

with H_0 being a constant. Next, the electric field can be calculated from Ampere's law as follows

$$E_x = -\eta_0 H_0 \frac{k_x}{k_0^2}\sin(k_x x)\frac{dg}{dy}e^{-jk_z z} \tag{3.3}$$

$$E_y = \eta_0 H_0 \frac{k_\parallel^2}{k_0^2}\cos(k_x x) g(y, k_y) e^{-jk_z z} \tag{3.4}$$

$$E_z = -\eta_0 H_0 \frac{jk_z}{k_0^2}\cos(k_x x)\frac{dg}{dy}e^{-jk_z z} \tag{3.5}$$

where η_0 is the intrinsic impedance of fee space. Here, (3.2)-(3.5) must satisfy the appropriate boundary conditions at $y = 0$; satisfying the following Leontovich boundary condition

$$\mathbf{E} \times \mathbf{u}_{\mathrm{n}} = Z_{\mathrm{s}}\big(\mathbf{u}_{\mathrm{n}} \times \mathbf{H}\big) \times \mathbf{u}_{\mathrm{n}} \tag{3.6}$$

where Z_{s} is the surface impedance at the interface and $\mathbf{u}_{\mathrm{n}}$ is the unit normal vector pointing to the air gap. In our case, (3.6) is equivalent to

$$Z_{\mathrm{s}} = -\frac{E_z}{H_x}\bigg|_{y=0} = j\eta_0 \frac{\gamma_0}{k_0}\frac{R-1}{R+1} \tag{3.7}$$

From (3.7), Z_{s} can be used to give a general description of surface impedance for the Fakir's bed of nails, as long as the pins are oriented along the y-direction. This is because (3.7) contains only the reflection coefficient of the structure and is invariant in translation along the y-direction. Moreover, at $y = h$ the modal fields also have to satisfy the appropriate boundary conditions. Thus,

$$Z_{\mathrm{s}} = \frac{E_z}{H_x}\bigg|_{y=h} = \frac{j\eta_0}{k_0}\frac{dg}{dy}\frac{1}{g}\bigg|_{y=h} \tag{3.8}$$

Combining (3.7) and (3.8), the following relationship is obtained

$$\frac{dg}{dy} - g\gamma_0 \frac{R-1}{R+1}\bigg|_{y=h} = 0 \tag{3.9}$$

where R is the reflection coefficient for the magnetic field from the interface at $y = h$ for the top bed of nails.

In the case of perpendicular polarization (i.e., there is no electric field in the direction of the pins), the propagating wave does not interact with the pins (i.e., with a thin wire approximation) and the modal equation for the TE mode is derived by substituting (2.20) into (3.8). Without loss of generality, for the rest of the analysis, the pins are assumed to surrounded by air (i.e., $\varepsilon_{\mathrm{h}} = 1$); this helps reduce losses, as the dielectric losses associated with the host medium are removed. After some algebraic manipulations, the modal equation for the TE mode reduces to

$$\sin\big[k_y(h + L_1 + L_2)\big] = 0 \tag{3.10}$$

where L_1 and L_2 are the length of pins at the bottom and top plate, respectively, and hence the solutions are

$$k_y = \frac{n\pi}{h + L_1 + L_2}, \quad n = 0, 1, \ldots \tag{3.11}$$

As can be easily seen, (3.11) gives the dispersion equation for a classical parallel-plate waveguide, where the plates are separated by a distance $h + L_1 + L_2$. A more accurate approach that accounts for the pin radii, by considering a corrected permittivity model in the x-z plane, would require a hybrid mode analysis and is out of the scope of this work.

Our focus will be for the case of parallel polarized incoming waves, since this highlights the behaviour of our structure. By combining (2.42) and (3.9) we obtained the more general transcendental equation given by (3.12). However, when pin length is identical, (3.12) reduces to (3.13). While, for the case that only one plate is populated with pins (i.e., $L_2 = 0$), (3.12) simplifies even further to the expression given in [10]. In the limit case where spatial dispersion effects can

be neglected (i.e., for densely packed pins, with $a/L \to 0$) then $\gamma_{\mathrm{TM}} \to 0$, resulting in the modal equations for $L_1 \neq L_2$ and $L = L_1 = L_2$, respectively, given in (3.14) and (3.15), respectively.

$$\left[\frac{k_0 k_{\mathrm{p}}^2 \tan(k_0 L_1)}{k_{\mathrm{p}}^2 + k_{\parallel}^2} - \frac{k_{\parallel}^2 \gamma_{\mathrm{TM}} \tanh(\gamma_{\mathrm{TM}} L_1)}{k_{\mathrm{p}}^2 + k_{\parallel}^2}\right]\left[\frac{k_0 k_{\mathrm{p}}^2 \tan(k_0 L_2)}{k_{\mathrm{p}}^2 + k_{\parallel}^2} - \frac{k_{\parallel}^2 \gamma_{\mathrm{TM}} \tanh(\gamma_{\mathrm{TM}} L_2)}{k_{\mathrm{p}}^2 + k_{\parallel}^2}\right]\tan(k_y h) +$$

$$\frac{k_{\mathrm{p}}^2}{k_{\mathrm{p}}^2 + k_{\parallel}^2} k_y k_0 \tan(k_0 L_1) - \frac{k_y k_{\parallel}^2 \gamma_{\mathrm{TM}} \tanh(\gamma_{\mathrm{TM}} L_1)}{\left(k_{\mathrm{p}}^2 + k_{\parallel}^2\right)} + \frac{k_{\mathrm{p}}^2}{k_p^2 + k_{\parallel}^2} k_y k_0 \tan(k_0 L_2) -$$

$$\frac{k_y k_{\parallel}^2 \gamma_{\mathrm{TM}} \tanh(\gamma_{\mathrm{TM}} L_2)}{\left(k_{\mathrm{p}}^2 + k_{\parallel}^2\right)} + k_y^2 \tan(k_y h) = 0 \tag{3.12}$$

$$\left[\frac{k_0 k_{\mathrm{p}}^2 \tan(k_0 L)}{k_{\mathrm{p}}^2 + k_{\parallel}^2} - \frac{k_{\parallel}^2 \gamma_{\mathrm{TM}} \tanh(\gamma_{\mathrm{TM}} L)}{k_{\mathrm{p}}^2 + k_{\parallel}^2}\right]^2 \tan(k_y h) +$$

$$2\frac{k_{\mathrm{p}}^2}{k_{\mathrm{p}}^2 + k_{\parallel}^2} k_y k_0 \tan(k_0 L) - 2\frac{k_y k_{\parallel}^2 \gamma_{\mathrm{TM}} \tanh(\gamma_{\mathrm{TM}} L)}{k_{\mathrm{p}}^2 + k_{\parallel}^2} + k_y^2 \tan(k_y h) = 0 \tag{3.13}$$

$$k_y k_0 \tan(k_0 L_1) + k_y k_0 \tan(k_0 L_2) + k_y^2 \tan(k_y h) - k_0^2 \tan(k_0 L_1)\tan(k_0 L_2)\tan(k_y h) = 0 \tag{3.14}$$

$$2k_y k_0 \tan(k_0 L) - \left[k_0 \tan(k_0 L)\right]^2 \tan(k_y h) + k_y^2 \tan(k_y h) = 0 \tag{3.15}$$

For each frequency in turn, (3.12) to (3.15) can be solved numerically for k_y and assuming propagation along the z-direction for simplicity, the dispersion equation can then be obtained from $k_z = \sqrt{k_0^2 - k_y^2}$. The previous equations are nonlinear and therefore, a starting point for k_y is required for most algorithms to converge onto a solution. Here, a scanning technique was employed in order to obtain various starting points and hence, a more accurate solution. As an example, the propagation characteristics for the first two TM modes are given in Figs. 3.3 and 3.4, for a symmetric configuration with $L = L_1 = L_2$ and an asymmetric configuration with $L_1 = 2L_2$, respectively. The latter corresponds to the special case of a PEC/PMC combination. Clearly, the bandgap where surface waves are suppressed can be controlled by adjusting the geometric characteristics of the structure.

For comparison, the dispersion characteristics for a bed of nails covered with a metal lid [10] is shown in Fig. 3.5. This structure was studied previously and serves as a convenient benchmark to provide an independent validation of our more general expressions.

As can be seen from Figs. 3.3 to 3.5, the dispersion characteristics of the second mode can be changed dramatically by adjusting the length of the pins (and also the separation distance between the plates). This results in a wide range of dispersion curves; whereby the second mode has a bandwidth from 50 MHz (in Fig. 3.3) to 12 GHz (in Fig. 3.5). Its cut-off frequency also changes, but this is a consequence of the total length $L_1 + h + L_2$ not being constant, as will be discussed in more detail later.

In contrast to Fig. 3.1, in Fig. 3.5 there are solutions to the left of the light line, corresponding to radiating fast waves, which is a result of the top plate. In this case, energy can be guided within the air gap between the two plates. However, as k_z increases these loosely bound surface waves convert to strongly confined surface waves.

The analytical model presented has been compared against full-wave numerical simulations using two commercially available software packages: High Frequency Structure Simulator (HFSS™), with results in Fig. 3.1 only, and CST Microwave Studio (CST MWS) used everywhere else. For the plain Fakir's bed of nails structure, the setup shown in Fig. 3.6(a) was used in order to employ absorbing

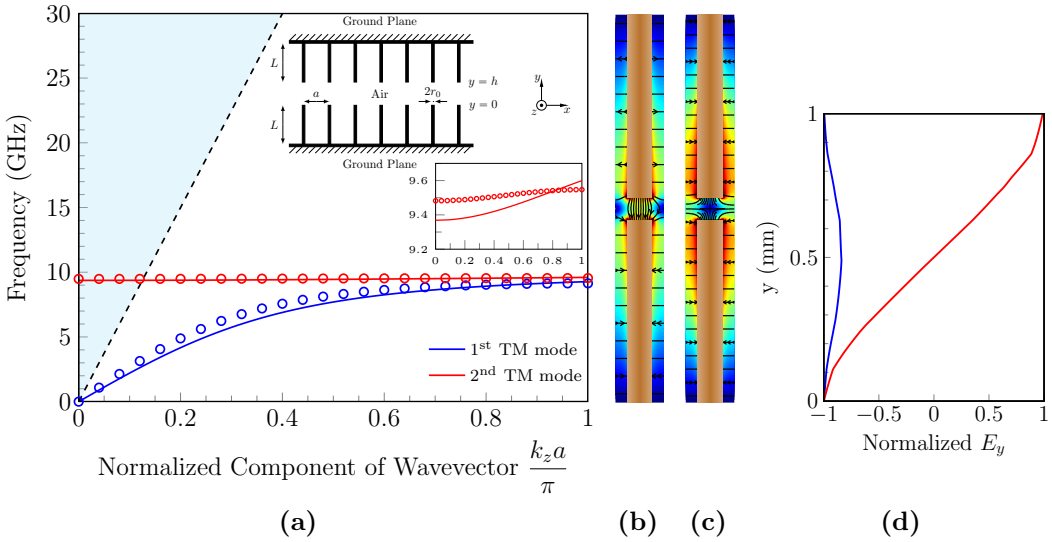


Figure 3.3: Real part of k_z for $L = L_1 = L_2 = 7.5$ mm, $r_0 = 0.5$ mm $a = 2$ mm and and $h = 1$ mm. Solid lines: analytical model. Discrete symbols: full-wave numerical simulation results using CST MWS. The light line is plotted with a dashed line. Inset shows that the second mode has a small but non-zero group velocity. (b) and (c) Electric field distributions at the pins for $k_z a = \pi$ in the first and second mode, respectively. (d) Electric field E_y at the center of the pins along the air gap. Blue curves correspond to the first mode and red curves to the second mode.

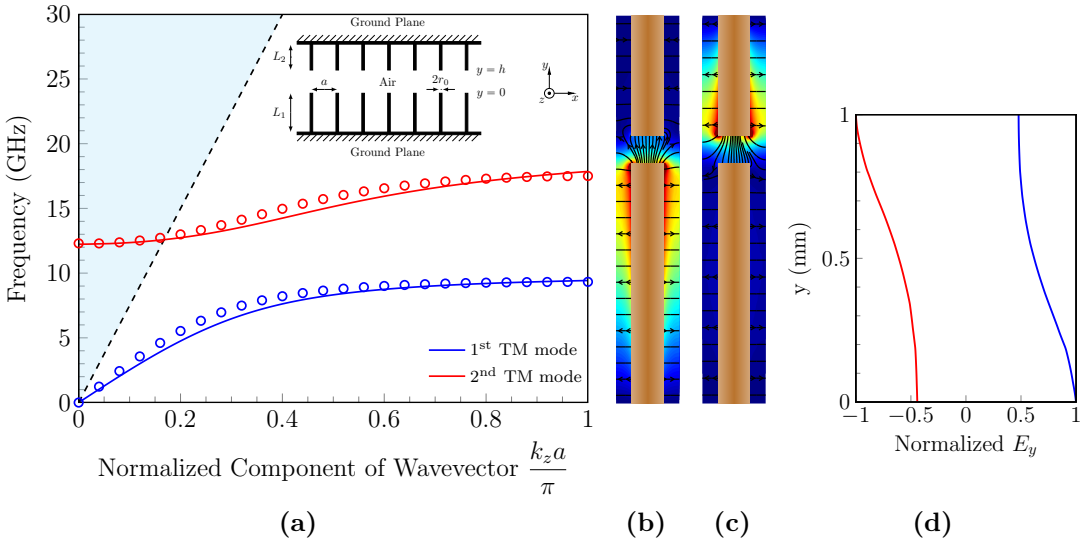


Figure 3.4: Real part of k_z for $L_1 = 7.5$ mm, $L_1 = 2L_2$, $r_0 = 0.5$ mm, $a = 2$ mm and $h = 1$ mm. Solid lines: analytical model. Discrete symbols: full-wave numerical simulation results obtained using CST MWS. The light line is plotted with a dashed line. (b) and (c) Electric field distributions at the pins for $k_z a = \pi$ in the first and second mode,respectively. (d) Electric field E_y at the center of the pins along the air gap. Blue curves correspond to the first mode and red curves to the second mode.

boundary conditions (i.e., perfectly matched layers, PML – only available with the eigenmode solver in HFSS™). With the eigenmode solvers used with HFSS™ and CST MWS, a single unit cell having periodic boundary conditions along the x and z-directions was adopted, as shown in Fig.

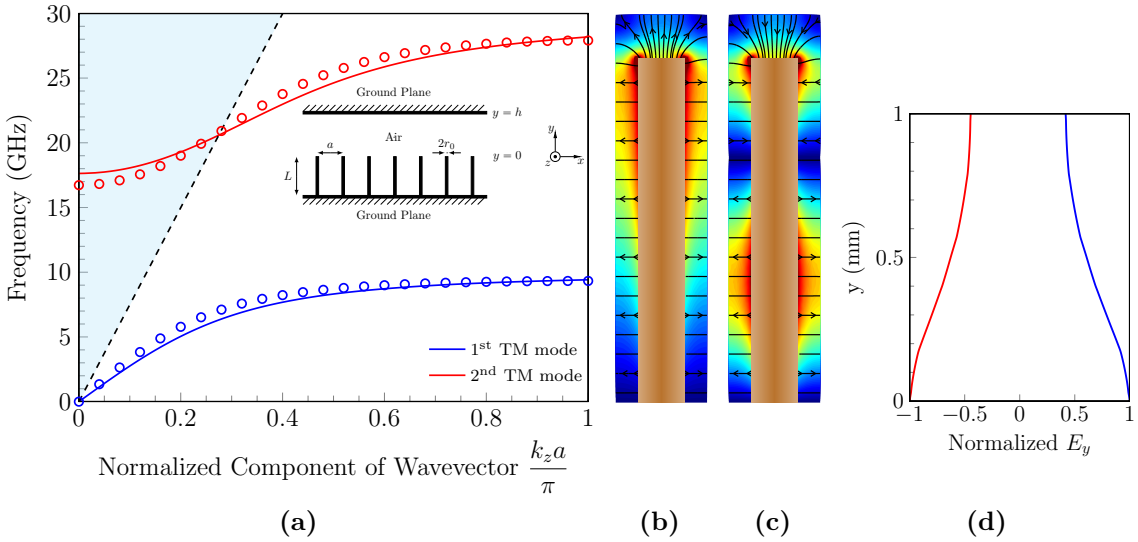


Figure 3.5: Real part of k_z for the benchmark structure with $L_1 = 7.5$ mm, $L_2 = 0$, $r_0 = 0.5$ mm, $a = 2$ mm and $h = 1$ mm. Solid lines: analytical model [10]. Discrete symbols: full-wave numerical simulation results obtained using CST MWS. The light line is plotted with a dashed line. (b) and (c) Electric field distributions at the pins for $k_z a = \pi$ in the first and second mode, respectively. (d) Electric field E_y at the center of the pins along the air gap. Blue curves correspond to the first mode and red curves to the second mode.

3.6(b).

By inspection of the electric field distributions for the aforementioned structures, a field enhancement at the edge of the tips can be observed. It is interesting to note that the second mode for the structures shown in Figs. 3.1 and 3.5 is a higher order mode, as can be seen in Figs. 3.1(c) and 3.5(c).

However, when both plates have equal length pins, the field patterns (within the wire media) remain similar for both modes, with surface waves at both bed of nails-air interfaces ($y = 0$ and $y = h$) being excited. In the case that the pins have different lengths, the field patterns remain the same, but the interface supporting the surface wave changes. This is because, in the frequency range where one interface supports a surface wave, the other interface exhibits a bandgap where no propagation is allowed. Moreover, the electric field decays exponentially away from the interface, in a similar way to surface plasmon polaritons with a metal-dielectric-metal (MDM) structure. For example, the field decays exponentially and tends to zero for the single bed of nails-air interface, as seen in Fig. 3.1(d); analogous to a metal-dielectric interface. This is expected, since the bed of nails has been modeled as an effective dielectric medium with a plasma-like behaviour. However, when a metal plate is placed in close proximity to the Fakir's bed of nails, the field saturates to a value significantly higher than zero, as shown in Fig. 3.5(d). For the symmetrical structure shown in Fig. 3.3, the two modes can be identified as symmetric and antisymmetric, respectively, to the center of the air gap, as shown in Fig. 3.3(d); resembling the field profile in a symmetric MDM structure.

On the other hand, the asymmetric structure shown in Fig. 3.4 does not support these type of modes and the field decays exponentially away from the interface, as shown in Fig. 3.4(d) (similar to Fig. 3.5(d)). This is in contrast to the asymmetric MDM structure, where the field is similar to that shown in Fig. 3.3(d), but with the structural asymmetry removing the field symmetry that was previously at the center of the gap. The reason for this discrepancy is that one wall of the Fakir's bed of nails waveguide exhibits bandgaps and, therefore, no surface waves are propagating,

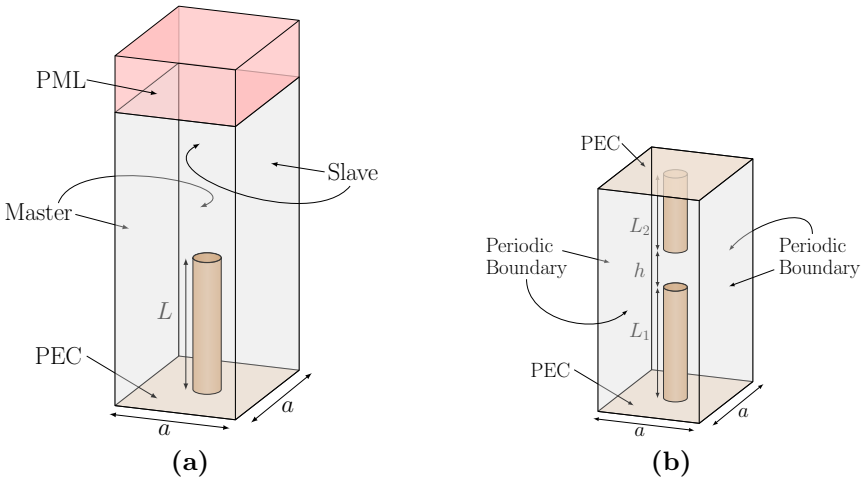


Figure 3.6: Simulation setup for the (a) bed of nails with HFSS^{TM} and (b) waveguide with CST MWS. The parameters used are: periodicity of the lattice $a = 2$ mm, air gap $h = 1$ mm and pin radius $r_0 = 0.5$ mm.

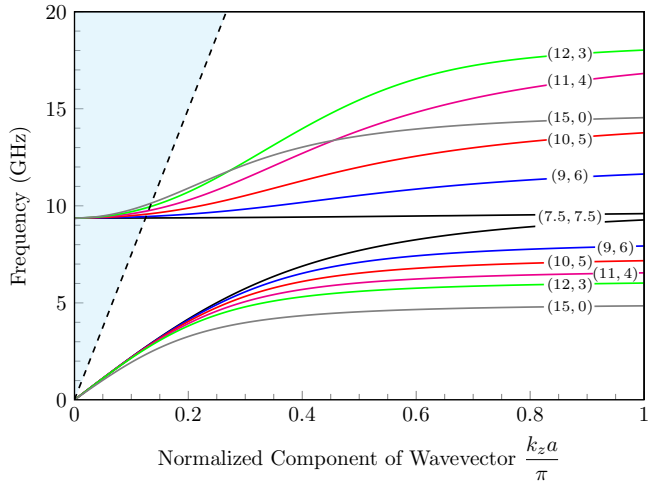


Figure 3.7: Real part of k_z for various (L_1,L_2) combinations when $L_1 + h + L_2 = 16$ mm. The rest of the parameters are given in Fig. 3.6. Lower and upper families of curves correspond to the first and second mode, respectively.

whereas a normal MDM would support surface waves at both interfaces.

In order to obtain a better physical grasp of the device behaviour, and how the various physical characteristics affect its performance, several parametric studies were undertaken. In the first study, the distance between the ground planes is kept constant and made equal to $t = L_1 + h + L_2 = 16$ mm; with the rest of the parameters as given in Fig. 3.6 and L_1, L_2 allowed to vary. This corresponds to the transition from the structure shown in the inset of Fig. 3.3 to a configuration similar to that shown in the inset of Fig. 3.5. Under these conditions, the frequency of the first mode increases monotonically as the air gap is shifted from the top (i.e., $L_1 = 15$ mm and $L_2 = 0$) to the center (i.e., $L = L_1 = L_2 = 7.5$ mm), with the surface wave resonance dictated by L_1 shown in Fig. 3.7. However, the second mode does not change monotonically and its bandwidth can be controlled by adjusting both lengths L_1, L_2. Bandwidth enhancement is obtained when both plates are suitably textured whereas $L_1 = L_2$ results in minimum bandwidth (almost suppressed).

In the second study, the lengths are kept constant with $L = L_1 = L_2 = 7.5$ mm and the gap

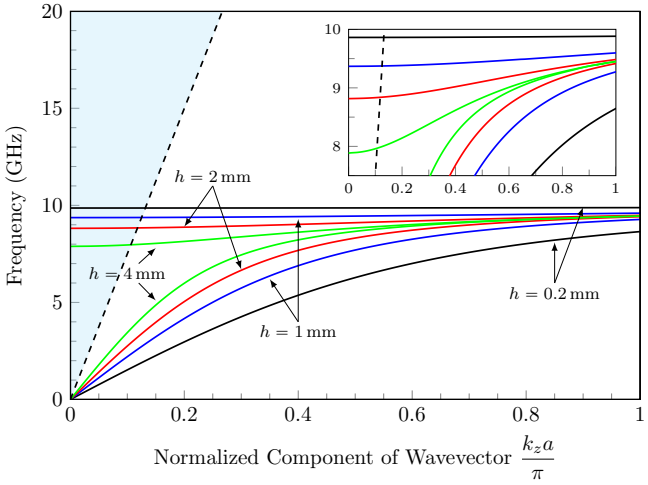


Figure 3.8: Real part of k_z for various gap sizes h when $L_1 = L_2 = 7.5$ mm. The rest of the parameters are given in Fig. 3.6. Lower and upper families of curves correspond to the first and second mode, respectively.

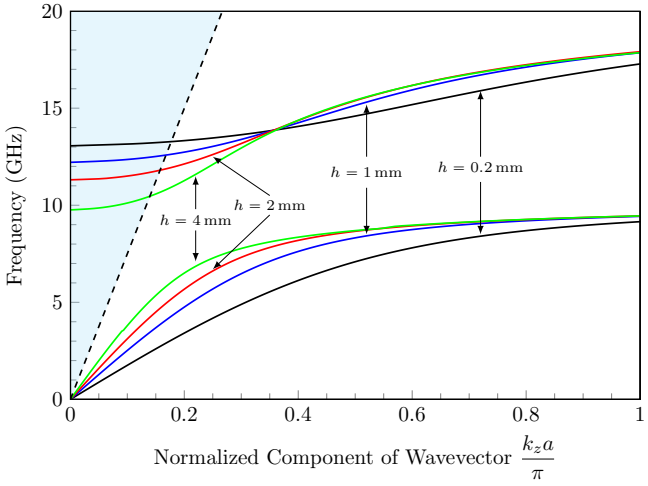


Figure 3.9: Real part of k_z for various gap sizes h when $L_1 = 2L_2 = 7.5$ mm. The rest of the parameters are given in Fig. 3.6. Lower and upper families of curves correspond to the first and second mode, respectively.

size h (or equivalently t) is varied. As seen in Fig. 3.8, for smaller gap sizes the coupling between surface waves at both interfaces is stronger, which results in two distinct branches in the dispersion curve. With larger gaps, the coupling between the bottom and top interfaces is weaker and the two branches coincide for larger k_z values. This resembles the split into two branches (corresponding to two modes) in the dispersion characteristics with a MDM structure. However, here there are always two distinct branches for small k_z values, which is in contrast to a classical MDM structure. Similarly, the results for the asymmetric structure with $L_1 = 2L_2 = 7.5$ mm are given in Fig. 3.9, where the surface wave resonances are affected by the values of L_1 and L_2; the cut-off frequency for the second mode can be tuned by changing the gap size. Finally, when the gap is varying with the total distance being a constant $t = 16$ mm and $L = L_1 = L_2$, the surface wave resonance is affected by the pin length. Therefore, larger gap sizes result in weaker coupling, pushing the dispersion curves closer together, as shown in Fig. 3.10. Finally, the effect of the pin radius is presented in Fig. 3.11, where as can be seen the slope of the dispersion curves changes significantly, particularly with

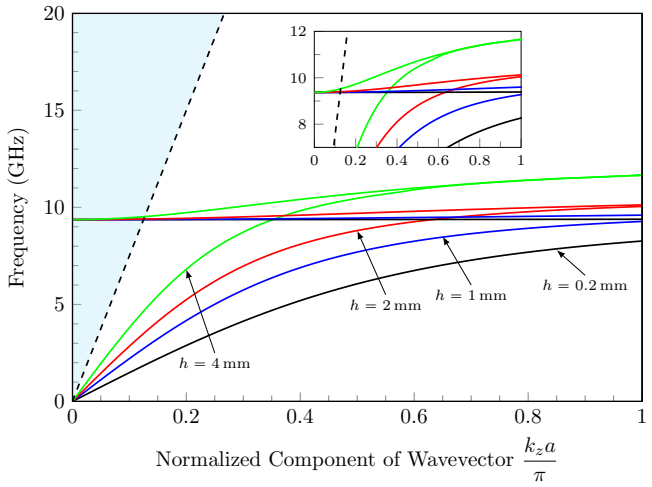


Figure 3.10: Real part of k_z for various gap sizes h when $t = h + 2L = 16$ mm. The rest of the parameters are given in Fig. 3.6. Lower and upper families of curves correspond to the first and second mode, respectively.

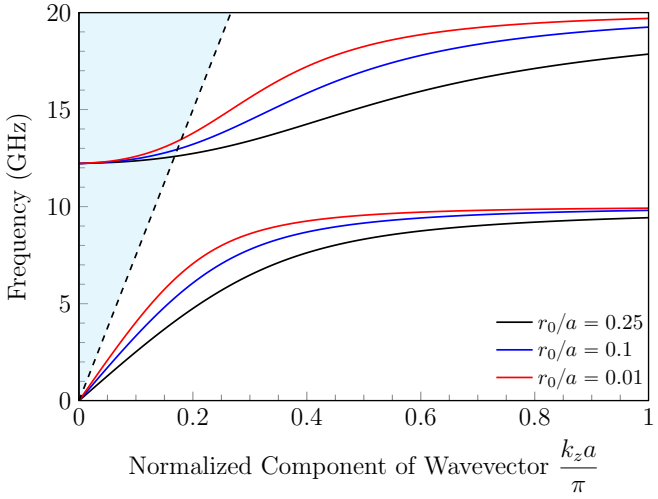


Figure 3.11: Real part of k_z for various radius sizes r_0/a when $L_1 = 2L_2 = 7.5$ mm. The rest of the parameters are given in Fig. 3.6. Lower and upper families of curves correspond to the first and second mode, respectively.

the second mode.

3.3 Transmission Line Model

The behaviour of the Fakir's bed of nails metamaterials waveguide can also be modeled using an equivalent transmission line circuit, as shown in Fig. 3.12. This has been previously demonstrated, but for the simple structure shown in Fig. 3.5 [10]. However, a more general model is required for waveguides having both the top and bottom implemented using Fakir's bed of nails with arbitrary pin lengths.

The dispersion equation can be derived from a series resonant network. Here, $Z^{\text{b}}_{\text{TEM}}$ and Z^{b}_{TM} represent the modal impedances seen at $y = 0$ (bottom interface), looking towards the lower PEC ground plane (where the pins are short circuited). Similarly, Z^{t}_{TEM} and Z^{t}_{TM} are the modal

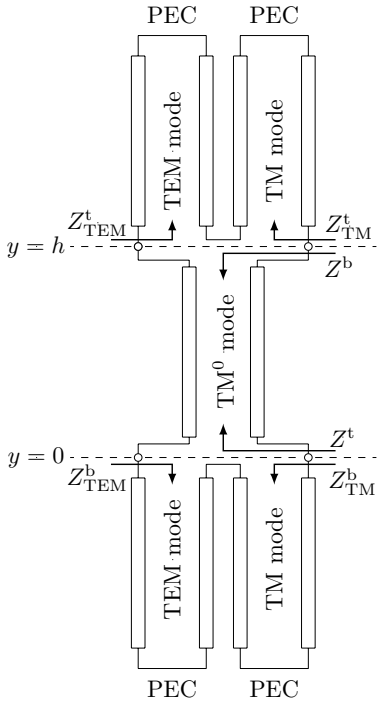


Figure 3.12: Equivalent transmission line model for the structure shown in Fig. 3.2 having both the top and bottom implemented using Fakir's bed of nails with arbitrary pin lengths.

impedances seen at $y = h$ (top interface), looking towards the upper PEC ground plane. Thus, (3.12) can be interpreted as a transmission line resonant network where from the transverse resonance condition $Z^{\mathrm{b}}_{\mathrm{TEM}} + Z^{\mathrm{b}}_{\mathrm{TM}} + Z^{\mathrm{t}} = 0$ the following is obtained

$$Z^{\mathrm{b}}_{\mathrm{TEM}} + Z^{\mathrm{t}}_{\mathrm{TEM}} + Z^{\mathrm{b}}_{\mathrm{TM}} + Z^{\mathrm{b}}_{\mathrm{TM}} + j\Big(Z^{\mathrm{b}}_{\mathrm{TEM}} + Z^{\mathrm{b}}_{\mathrm{TM}}\Big)\Big(Z^{\mathrm{t}}_{\mathrm{TEM}} + Z^{\mathrm{t}}_{\mathrm{TM}}\Big)\frac{\tan(k_y h)}{\eta_0} + j\eta_0 \tan(k_y h) = 0 \quad (3.16)$$

where

$$Z^{\mathrm{b}}_{\mathrm{TEM}} = j\eta_0 \frac{k_0 k_{\mathrm{p}}^2}{k_y\left(k_{\mathrm{p}}^2 + k_{\parallel}^2\right)} \tan(k_0 L_1) \quad (3.17)$$

$$Z^{\mathrm{t}}_{\mathrm{TEM}} = j\eta_0 \frac{k_0 k_{\mathrm{p}}^2}{k_y\left(k_{\mathrm{p}}^2 + k_{\parallel}^2\right)} \tan(k_0 L_2) \quad (3.18)$$

$$Z^{\mathrm{b}}_{\mathrm{TM}} = -j\eta_0 \frac{k_{\parallel}^2 \gamma_{\mathrm{TM}}}{k_y\left(k_{\mathrm{p}}^2 + k_{\parallel}^2\right)} \tanh(\gamma_{\mathrm{TM}} L_1) \quad (3.19)$$

$$Z^{\mathrm{t}}_{\mathrm{TM}} = -j\eta_0 \frac{k_{\parallel}^2 \gamma_{\mathrm{TM}}}{k_y\left(k_{\mathrm{p}}^2 + k_{\parallel}^2\right)} \tanh(\gamma_{\mathrm{TM}} L_2) \quad (3.20)$$

In the limit case, where spatial dispersion effects can be neglected (i.e., by having densely packed pins), $Z^{\mathrm{b}}_{\mathrm{TM}} = Z^{\mathrm{t}}_{\mathrm{TM}} = 0$ and (3.21) reduces to

$$Z^{\mathrm{b}}_{\mathrm{TEM}} + Z^{\mathrm{t}}_{\mathrm{TEM}} + \Big(Z^{\mathrm{b}}_{\mathrm{TEM}} Z^{\mathrm{t}}_{\mathrm{TEM}} + \eta_0^2\Big)\frac{j\tan(k_y h)}{\eta_0} = 0 \quad (3.21)$$

3.4 Discussion and Conclusion

Using modal analysis, the propagation of electromagnetic waves in a parallel-plate waveguide employing the Fakir's bed of nails has been studied both analytically and numerically. Here, we have expanded previously published models to address the more general case for waveguides having both top and bottom walls implemented using the Fakir's bed of nails with arbitrary pin lengths.

The dispersion properties can be controlled by adjusting the geometric parameters of the structure and, specifically, the length of the pins and their separation distance. The bandwidth of the modes and the bandgaps can be easily tuned with the more general waveguide structure investigated here.

Although the simplified model used in our calculations does not take into account the finite radius of the pins and the resulting associated fringe capacitance (i.e., deviating from thin wire approximation), the results are still very accurate for most practical applications; this accounts for the small discrepancies seen between the analytical and numerical results.

An equivalent transmission line model has also been presented the more general waveguide structure. The dispersion characteristics have been compared and contrasted with the classical metal-dielectric-metal structure commonly used in optics. Moreover, our analytical modeling can be modified to describe metal-pipe rectangular waveguides, having two conventional parallel metal walls and the other two walls replaced by the Fakir's bed of nails.

Our analytical model provides a quick way to investigate the behaviour of waveguide structures that employ the Fakir's bed of nails walls, without the need for time-consuming full-wave numerical modeling analysis. It is believed that the work presented here can find diverse applications, such as the design of novel resonators, filters and mode converters.

References

[1] M. S. Aftanasar, P. R. Young, I. D. Robertson, J. Minalgiene and S. Lucyszyn, "Photoimageable thick-film millimetre-wave metal-pipe rectangular waveguides", *IEE Electron. Lett.*, vol. 37, no. 18, pp. 1122-1123, Aug. 2001

[2] S. Lucyszyn, D. Budimir, Q. H. Wang and I. D. Robertson, "Design of compact monolithic dielectric-filled metal-pipe rectangular waveguides for millimetre-wave applications", *IEE Proc. Microw. Antennas Propag.*, vol. 143, no. 5, pp. 451-453, Oct. 1996

[3] S. Lucyszyn, Q. H. Wang and I. D. Robertson, "0.1 THz rectangular waveguide on GaAs semi-insulating substrate", *IEE Electron. Lett.*, vol. 31, no. 9, pp. 721-722, Apr. 1995

[4] S. F. Mahmoud, "Electromagnetic Waveguides: Theory and Applications", *IEE Electromagn. Waves Ser.*, vol. 32, Peter Peregrinus, London, 1991

[5] R. Mendis and D. M. Mittleman, "Multifaceted terahertz applications of parallel plate waveguide: TE1 mode", *Electron. Lett.*, vol. 46, no. 26, pp. 40-44, Dec. 2010

[6] R. Mendis, "THz transmission characteristics of dielectric-filled parallel plate waveguides", *J. Appl. Phys.*, vol. 101, no. 8, p. 083115, Apr. 2007

[7] R. Mendis and D. Grischkowsky, "Undistorted guided-wave propagation of subpicosecond terahertz pulses", *Opt. Lett.*, vol. 26, no. 11, pp. 846-848, Jun. 2001

[8] R. Mendis and D. M. Mittleman, "A 2-D artificial dielectric with $0 \leqslant n < 1$ for the terahertz region", *IEEE Trans. Microw. Theory Tech.*, vol. 58, no. 7, pp. 1993-1998, Jul. 2010

[9] M. G. Silveirinha, C. A. Fernandes and J. R. Costa "Electromagnetic characterization of textured surfaces formed by metallic pins", *IEEE Trans. Antennas Propag.*, vol. 56, no. 2, pp. 405-415, Feb. 2008

[10] A. Polemi, S. Maci and P.-S. Kildal "Dispersion characteristics of a metamaterial-based parallel-plate ridge gap waveguide realized by bed of nails", *IEEE Trans. Antennas Propag.*, vol. 59, no. 3, pp. 904-913, Mar. 2011

[11] R. Collin "Field Theory of Guided Waves", *Wiley-IEEE Press*, 1990

Chapter 4

Coupling-induced Red-shifted Plasmonic Resonances on Infinite Chains of Nanopins

In the previous chapters, an array of pins arranged periodically next to each other were studied. Here, this arrangement is modified so that the pins are placed periodically along their vertical axis to form an infinite chain of pins. The resonant properties of infinite chains of gold nanostructures separated by small gaps are studied theoretically and the observed red-shift of the resonance in comparison to a single nanopin is explained in terms of coupled plasmonic modes across the gaps. The deduced dispersion characteristics for variable gap sizes and nanopin lengths provide physical insight into the coupling mechanisms. It is also proven that the resonant behaviour of an infinite chain of nanopins is in close analogy to that of an isolated narrow-gap split ring or split square resonator. This confirms that surface plasmon coupling across the gap can be employed for quantitative description of the red shift of the split ring resonance, traditionally attributed to the ring capacitance variation with decreasing gap. This study, generalized to two and three dimensions, will aid the design of metamaterial nanostructures with desired resonance characteristics.

4.1 Introduction

The science of surface plasmons started well over a century ago with the works of Sommerfeld [1] and Fano [2] who called them "superficial waves". The next major advance was due to Oliner and Tamir [3] who showed that both forward and backward surface waves may propagate on an infinitely wide metallic slab (a detailed study of this type of waves can be found in the review by Economou [4]). Renewed interest in surface plasmons came around the turn of the millennium. The eigenmodes of metal slabs of finite width were found by Berini [5, 6] and Al-Bader [7], whereas the resonances of various nanostructures were determined by Kottmann *et al.* [8, 9] and Aizpurua *et al.* [10]. However, the greatest interest emerged with the advent of metamaterials. On the one hand, it was shown that the exponentially growing waves in Pendry's superlens [11] were due to the excitation of surface plasmon resonances at the rear boundary. An explanation in terms of surface plasmons was also bound to come for describing the operation of metallic split ring resonators, the most popular building block of metamaterials [12, 13]. Since research was originally focused on radio-frequencies and microwaves, where the wavelength is large compared to element size, it was reasonable to explain resonances in terms of lumped-element LC circuits [14]. This approach was further expanded in [15, 16] to distributed circuits which made it possible to calculate not only the fundamental resonant frequency but the higher harmonics as well. Interestingly, the

drive towards applications in the optical region did not immediately lead to the demise of the circuit picture. It was retained with the modification that the kinetic inductance was added to the magnetic inductance [17–19]. However, at such high frequencies the natural approach was to attribute resonances to surface plasmons bouncing between the two ends of the structure, as done by Ditlbacher *et al.* [20] using silver nanopins. Following this lead, further works were published: a thorough investigation of a number of different structures by measuring reflection of a plane wave [21, 22], dependence on the thickness of the structure [23], I, L, O, U structures [24], additional resonances for L structures [25, 26] and L structures in different periodic configurations [27]. There is now a consensus that the behaviour of such structures is best described by surface plasmons but that does not mean that the circuit description should be disregarded. Meyrath *et al.*[28] introduced a general model that could also account for radiation resistance and there was also a refined *LC* model by Corrigan *et al.* [29] that was capable of matching experimental results.

The aim of this chapter is to analyze plasmonic behaviour of an infinite chain of nanopins aligned along their vertical axis and to quantify the red-shift of the resonance in comparison to that of a single nanopin. Four different metallic nanostructures are investigated, namely a split ring (SR), split square (SS), free pin (FP) and infinite chain of coupled pins – also referred to as coupled pins (CP) for short – as shown in Fig. 4.1, with the first two acting as reference benchmark structures for comparison purposes. The emphasis is on the last two, the free pin and the infinite chain of coupled nanopins, with the main interest being the inter-relationship of their resonant frequencies while the gap between the pins is varied. Coupled pins have been investigated before as metamaterial elements under the name of cut-wires, in particular, by Maslovski *et al.* [30], Dolling *et al.* [31], Tsai *et al.* [32] and Wakatsuchi *et al.* [33] but their aims were different. In [30] they were looking for negative permittivity, in [31] the search was for magnetic atoms, in [32] they designed a metamaterial gradient index diffraction grating, and the emphasis in [33] was on matching the resonant frequencies, predicted by a numerical model, with a sophisticated equivalent circuit. Our investigation is mainly concerned with the variation of resonant frequencies as the gap between the coupled pins varies. The explanation of the phenomena is based on the properties of coupled surface plasmons, a discipline just emerging.

4.2 Description of the Structures and Numerical Approach

The resonance properties of the four structures shown in Fig. 4.1 are investigated with the simplest one being a straight pin resonator (FP), which is the building block of other nanostructures and our starting point. The well-known split ring resonator (SR) and a modification of the split ring, referred to as split square resonator (SS), on account of its rectangular shape, are also studied. An entirely new structure, an infinite chain of coupled pins (CR), is presented here and its behaviour is compared and contrasted to the aforementioned structures. In all four cases the cross section is constant and equal to $a \times a = 10 \times 10\ \mathrm{nm}^2$.

Full-wave numerical simulations of gold structures in free-space were performed, employing the lossy Drude [34, 35] model that provides a fairly good approximation for the permittivity of gold at infrared frequencies. The variation in the relative permittivity with frequency, as described by the Drude model, is given by the following expression

$$\varepsilon_{\mathrm{r}} = 1 - \frac{\omega_{\mathrm{p}}^2}{\omega(\omega - j\gamma_{\mathrm{p}})} \tag{4.1}$$

where ω and ω_{p} are the angular frequency and angular plasma frequency, respectively, and the damping constant γ_{p} indicates the losses within the metal. In the case of gold, the plasma frequency

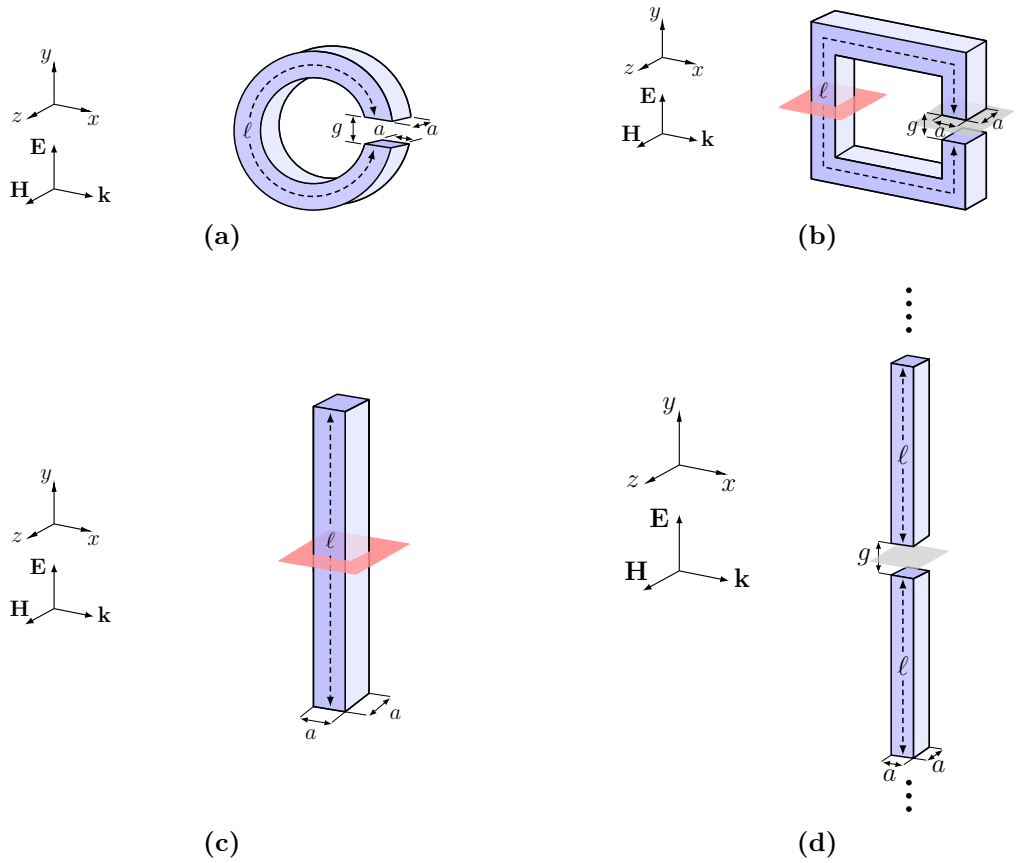


Figure 4.1: The four nanostructures under study. (a) Split ring (SR), (b) split square (SS), (c) free pin (FP) and (d) infinite chain of coupled pins (CP). Possible symmetry planes for the electric field are also shown in red and gray.

$\omega_\mathrm{p} = 136.66 \cdot 10^{14}$ rad/s corresponding to a plasma wavelength of $\lambda_\mathrm{p} = 2\pi c/\omega_\mathrm{p} \simeq 138$ nm with c being the speed of light and the damping constant $\gamma_\mathrm{p} = 40.84 \cdot 10^{12}$ rad/s [34, 35]. The previous expression for the permittivity results in a surface plasmon resonance frequency $\omega_\mathrm{s} = \omega_\mathrm{p}/\sqrt{2} \simeq 1535$ THz.

The excitation is in the form of a plane wave propagating along the x-direction with its electric field in the y-direction, parallel to the pin. Time domain full-wave numerical simulations, using the commercially available software package CST Microwave Studio (CST MWS), have been performed to obtain the frequency response of the various structures. In the simulations, an adaptive meshing was used and the grid step varied from 0.4 nm inside the structures to 3 nm in free space. Open boundary conditions were approximately 100 nm away from the structure. The simulation size was typically around 3 million mesh cells and symmetry planes have also been employed to reduce simulation time.

4.3 Symmetry Considerations and Resonances

At the lowest resonance, the split ring and the split square have similar charge distributions with one half being charged positively and the other half negatively. The presence of a symmetry plane in the middle of the split square (indicated by red and gray planes in Fig. 4.1(b)) provides a hint for the search of an equivalent pin structure which would exhibit similar plasmonic response. For this reason, the split square was straightened to form a pin of the same total length and cross sectional

Table 4.1: Comparison of the resonant frequency of four different nanostructures. The structures have a total lenght of 270 nm and a gap of 10 nm.

	1st resonance (THz)	2nd resonance (THz)	3rd resonance (THz)
Split Ring	121.5	346.2	519.8
Split Square	127.7	357	523.8
Free Pin	142.9	366.8	535.6
Coupled Pins	119.3	352	525.5

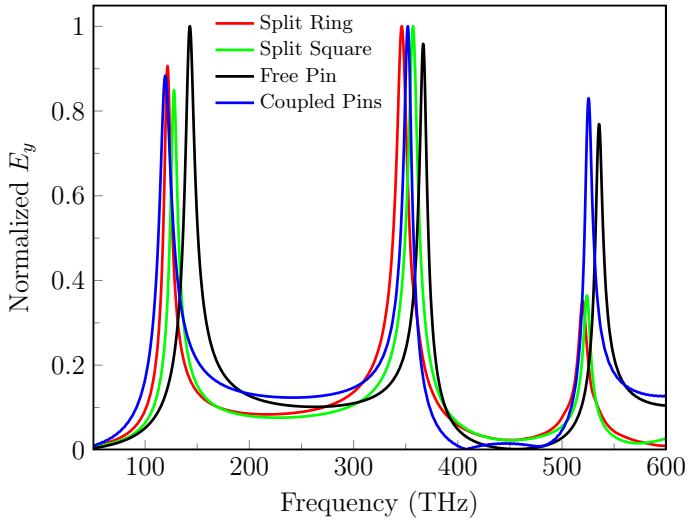


Figure 4.2: Normalized electric field as a function of frequency for the various nanostructures. The structures have a gap of 10 nm and all of them have a total length of 270 nm.

area that is symmetrical with respect to the red plane, as shown in Fig. 4.1(c). Next, additional pins of the same length are introduced along the y-direction (axis of the pins) to establish interaction similar to that in the gap of the split square. The spacing between the two pins should be equal to the gap g. With a finite number of pins, the outer pins lack symmetry. Therefore, the pin system should be infinite to achieve symmetry, both at the middle of the structure and at the middle of the gap. In order to simulate an infinite structure, appropriate boundary conditions must be used, mimicing its behaviour. The symmetry plane (red plane in Fig. 4.1(c)) in the middle of the pin, when disregarding the asymmetric modes that correspond to surface charges with the same sign on both ends of the pin (which cannot be excited by a plane wave), results in a node in both the charge and electric field distributions at $y = 0$. This corresponds to an electric symmetry plane at $y = 0$ (implemented by assigning a perfect electrical conductor boundary ($E_{\tan} = 0$) with CST MWS). Following a similar approach, a perfect electrical conductor boundary should be established in the middle of the gap. Now, the charge and current distributions are mirrored and form an infinite pin structure (a similar effect in optics can be observed when standing between two parallel mirrors). In the split ring and split square simulations (both structures have identical perimeter and gap size), there is an electric and a magnetic symmetry plane with both planes being perpendicular to each other and to the exciting electric field (x-z plane), going through the center of the structure. We need to emphasize here that the CP structure has not been investigated before. We have surmised that, as far as the plasma resonances are concerned, the CP structure behaves similarly to the SR and SS structures because the physics is the same; the resonance is due to surface plasmons coupled across the gap.

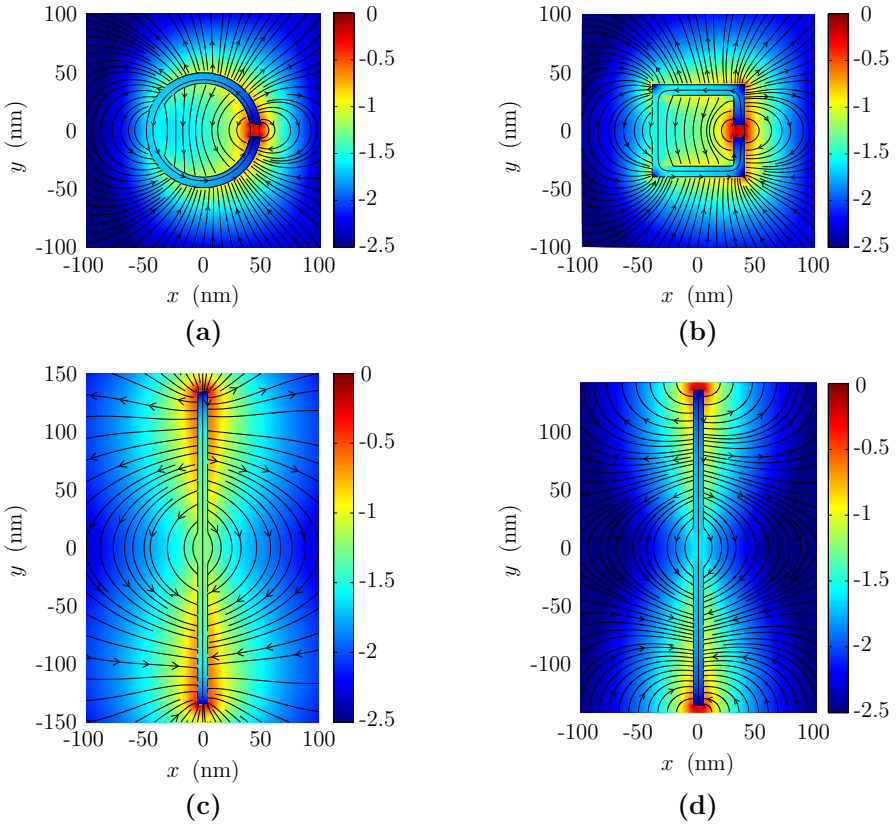


Figure 4.3: Comparison of the electric field patterns at the lowest resonance for the (a) SR, (b) SS, (c) FP and (d) CP. The field strength is plotted on a logarithmic scale normalized to the field maximum.

In all four cases, the structure length measured along the middle of the cross section was taken as $\ell = 270$ nm. There is obviously no gap associated with the free pin but for the three others the gap size was $g = 10$ nm. The simulated electric field is plotted as a function of frequency in Fig. 4.2, showing the first three resonant frequencies for the split ring, split square, free pin and infinite chain of pins. As can be seen, the resonant frequencies of the structures (having the same total length) match, so it is safe to assume that they generate the same type of surface plasmon modes: symmetrical surface charge distributions like $+-$, $+--+$ and $+--+--+-$ at the first, second and third resonant frequency, respectively [24]. The field patterns of the various structures are discussed in the following section, confirming this claim.

The exact values of the resonant frequencies are given in Table 4.1 with the quality factor at the first resonance ranging from 9 to 12. As expected, the SR and the SS have very similar resonant frequencies for all modes. However, they are not identical, suggesting that the shape of the structure, and the extra edges with the SS, have a minor influence on the resonance. The resonant frequency of the CP is also close to those of the SR and SS, indicating that the assumption made previously, is essentially correct whereas the resonant frequency of the free pin is quite different. Thus the assertion, for example in [24], that only the total length is important, is no longer valid. The structures investigated there were the I, L, O, U types, none of them having a gap. However, in the presence of a gap, the behaviour changes and can be described qualitatively in terms of an LC circuit model: the capacitance increases as the gap decreases resulting in a lower resonant frequency.

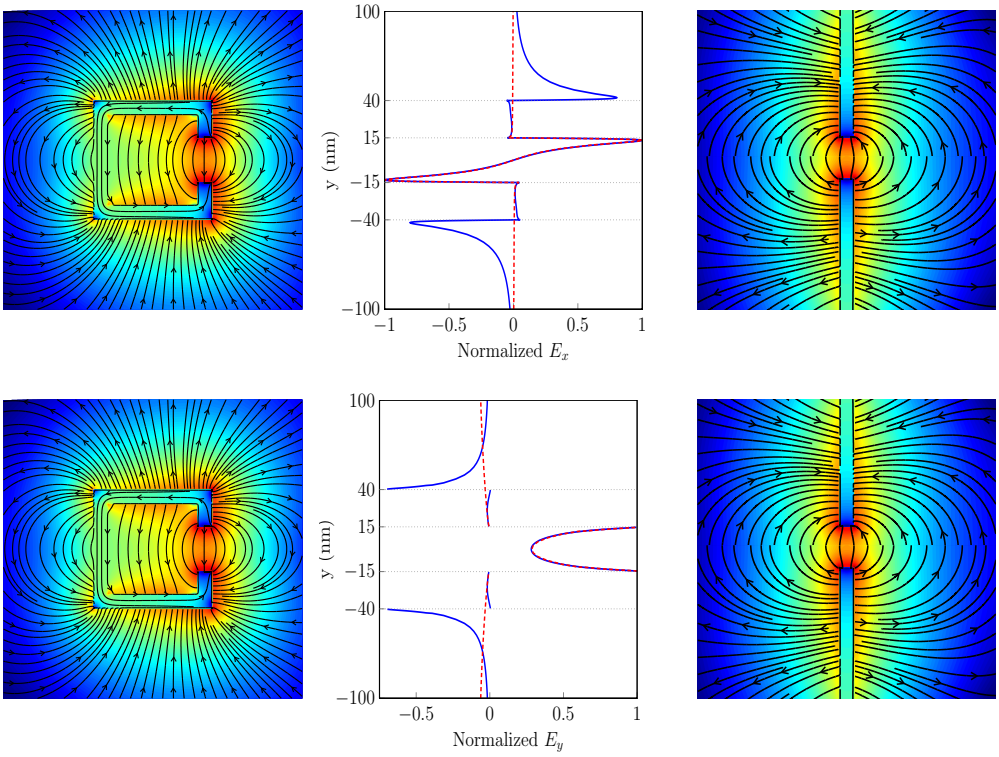


Figure 4.4: Comparison of the x and y components of the electric field distribution along the gap of the square structure with the gap of 30 nm (blue line) and along the coupled pin (red line).

4.4 Electric Field Patterns

The electric field lines of the various structures at the lowest resonant frequency are extracted in the symmetry plane, as shown in Fig. 4.3. This offers the opportunity to compare the concentration and direction of the field lines and to check the intensity of the field ($|E|$) at each point in the plane. At the lowest resonance, the simplest symmetrical pattern may be expected: one part of the structure is charged positively and the other one negatively.

Fig. 4.3 also shows the electric field distributions for the SR, SS, FP and CP structures. In Figs. 4.3(a)-(b) a high field intensity is observed in the gap whereas the lowest field values can be found in the middle of the structures. Similar field distribution can be observed along the CP. Obviously, having no gap, the field distribution along the FP is quite different. As shown in Fig. 4.3, the electric field lines point away from the boundary at the lower part and towards the boundary at the upper part, indicating a positive surface charge at the upper and a negative surface charge at the lower part. The surface charge varies monotonically along the CP and the SR. As expected, the additional edges of the SS distort the monotony acting as electric field "hot spots". This also explains the difference in the resonant frequency compared to the SR and CP.

The next step in comparing the nanostructures is to investigate in greater detail the electric field distributions. Therefore, both the x and y components of the electric field are plotted along the y-direction at $z = 0$ nm and $x = 39$ nm for the SS and $x = 4$ nm for the CP. The reason for moving off the axis of the pin is that E_x is zero at $x = 0$ due to symmetry.

The field profile for the split square has been shifted so that the edges of the two structures coincide, enabling a direct comparison of the fields. As shown in Fig. 4.4, the coupled pins and the split square have very similar field patterns within the metal and in the gap.

After comparing the resonant behaviour of nanostructures with various shapes and same gap

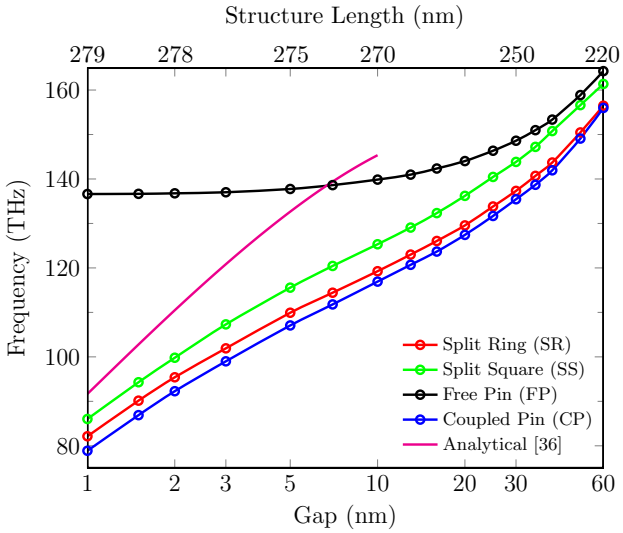


Figure 4.5: Comparison of the resonant frequencies of the nanostructures with varying gap size. The structure length is always $\ell + g = 280$ nm.

size, the gap is varied i.e. turn a U-shaped structure into a split square and investigate whether the assumptions/claims made in the previous sections are still valid. For this reason, the gap size is varied from 60 nm, corresponding to the U-shaped structure, to 1 nm, while keeping the perimeter $\ell + g$ constant and equal to 280 nm. For the free pin, this results in length variation from 220 nm to 279 nm. A longer structure leads to longer plasmon wavelength and consequently a decline in the resonant frequency, as shown in Fig. 4.5. Now, the question arises: can one reproduce the green, red and blue curves, given in Fig. 4.5, obtained by simulations, using analytical techniques? Let us first try the circuit model. As the gap size decreases, it is obvious that all three, the inductance, surface capacitance and gap capacitance, increase, and consequently the resonant frequency is bound to decline. Some approximate expressions for the above three quantities were obtained for the SR by Delgado *et al.* [36]. For example, the resonant frequency can be calculated from [36]

$$f_0 = \frac{1}{2\pi\sqrt{\left(L_{\text{mag}} + L_{\text{kin}}\right)\left(C_{\text{gap}} + C_{\text{surf}}\right)}} \tag{4.2}$$

where $L_{\text{mag}} = \mu_0 R\left[\ln\left(\frac{8R}{a+g}\right) - \frac{1}{2}\right]$ is the magnetic inductance, $L_{\text{kin}} = \frac{2\pi R - g}{a^2\omega_{\text{p}}^2\varepsilon_0}$ is the kinetic inductance, $C_{\text{gap}} = \varepsilon_0\left(2a + g + \frac{a^2}{g}\right)$ is the gap capacitance, $C_{\text{surf}} = \frac{4\varepsilon_0 a}{\pi}\ln\left(\frac{4R}{g}\right)$ is the surface capacitance and R is the mean radius of the SR. The variation of the resonant frequency against gap size is shown in magenta in Fig. 4.5. The analytically obtained results, can very roughly predict the trend of the curve corresponding to the split square. Unfortunately, no further information is provided. This approximation is marginally acceptable for the 1 nm gap and deteriorates quickly as the gap increases, since the analytical model was derived for small gaps and at frequencies well below the plasma frequency. Therefore, it is of limited practical use; we only report these results in comparison to our more accurate surface plasmon approach.

4.5 Explanation in Terms of Coupled Surface Plasmons

One has to admit that explanation in terms of a circuit model is both easier and more in line with common knowledge. Once the frequency response is experimentally or numerically obtained, the

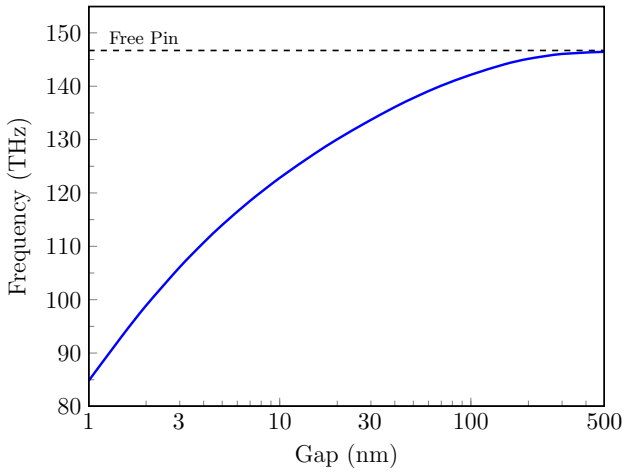


Figure 4.6: Resonant frequency for the infinite chain of coupled nanopins with varying gap size. The resonance of the free pin is also shown with dashed line. The length of the structure is $\ell = 260$ nm.

natural inclination is to find an equivalent circuit model that matches this behaviour and hence, establish an analytic expression.

The problem with an explanation in terms of surface plasmons is that no analytic formulation has been found so far, except for the cases of a single metal-dielectric interface and an infinite slab with finite thickness. There are no expressions for the resonant frequencies of a free pin, let alone an infinite chain of coupled nanopins. Therefore, the resonant frequencies under various conditions have to be determined either experimentally or numerically.

The physics is that surface plasmons on opposite sides of the gap are coupled to each other and, as is well known, the resonant frequency, is split in the presence of coupling. When the interaction is stronger (gap reduced) the split is larger. This gives rise to two distinct resonant frequencies; one higher and one lower than the uncoupled resonant frequency. As shown in Fig. 4.5, the coupled resonant frequencies are indeed below the uncoupled resonant frequency and the split increases for smaller gaps.

In order to further explore the behaviour of the infinite chain of coupled nanopins, several parametric studies have been undertaken to provide physical insight. Comparing the behaviour of the infinite chain of coupled nanopins to that of the free pin, it can be seen that for large gap values the resonant frequency for the coupled pins tends to the resonant frequency of a single free pin. This occurs because for gap sizes large compared to the structure length, the fields have decayed sufficiently so that the pins are effectively decoupled. This is shown in Fig. 4.6, where the resonant frequency as a function of gap size is plotted. Practically when the gap is larger than about twice the structure's length the resonant frequency reduces to that of the free pin.

Next, a parametric study with respect to gap size was undertaken. As can be seen in Fig. 4.7, for decreasing gap sizes the resonant frequency is shifted to lower values. This highlights the fact that coupling is stronger for smaller gaps and hence, stronger coupling between the pins results in higher detuning in the resonant frequency. The surface plasmon dispersion diagram is shown in Fig. 4.8, where the black and blue curves show the well-known relationship between frequency and wave number for a single interface and a 10 nm thick slab, respectively, and are used as reference structures. It is interesting to note that although a plane wave in free space cannot excite an infinite interface (as explained in Chapter 1), it does interact with the structures shown in Fig. 4.1. This is possible because of the finite length of the structures and their sharp edges and corners that create scattering effects that are sufficient to excite the surface plasmon polaritons. The dispersion

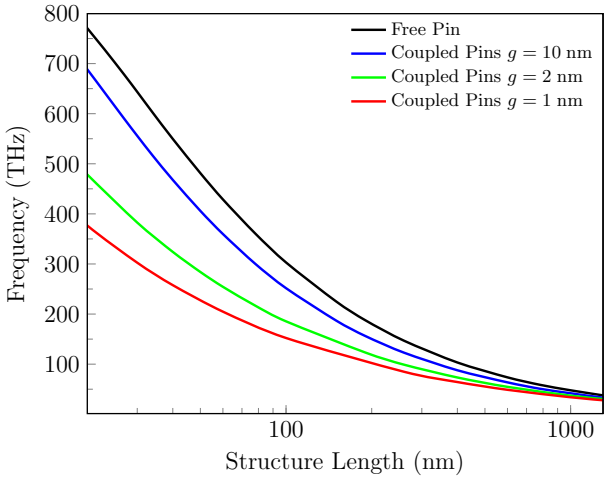


Figure 4.7: Resonant frequency for the infinite chain of coupled nanopins with varying structure length. The resonance of the free pin is also shown for comparison.

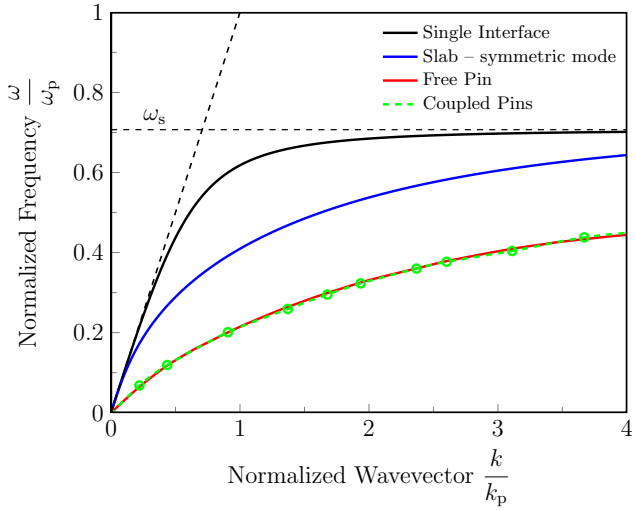


Figure 4.8: Dispersion diagram for the infinite chain of coupled nanopins. The curves for a free pin, a slab and a single interface are also plotted as reference structures.

curve for a pin of square cross section is not so well-known. It may be expected to be below the dispersion curve of the slab and that is indeed the case (see red curve in Fig. 4.8), as shown earlier by Tatartschuk *et al.* [24]. The new result is that for the infinite chain of coupled nanopins. In this case the dispersion relation may be expected to depend strongly on the size of the gap. However, as shown by the green curve in Fig. 4.8, this does not occur and the dispersion curve for the CP matched that for the FP. The dispersion curve can be obtained by extracting the wavelength at the resonant frequencies. For example, Fig. 4.9 shows the electric field along the coupled pins at two resonant frequencies, where the wavelength within the nanopins at 820 THz is shown in Fig. 4.9(a) and is $\lambda \simeq 53$ nm, corresponding to $k_y = 2\pi/\lambda \simeq 11.85 \cdot 10^7$ m^{-1}. Following this approach, the rest of the points on the dispersion curve can be obtained. The curves are shown only up to $k_y/k_p = 4$ but the monotonic increase in frequency as a function of wave number can already be seen. This aspect of the surface plasmon dispersion curves is well known. Eventually, in the limit for large k_y values, all curves must tend to the asymptotic value of the surface plasmon resonance, $\omega_p/\sqrt{2}$. For example, a large wavevector component along the slab results in a large imaginary wavevector component across the slab since $k_x^2 + k_y^2 = k^2$. Therefore, there is a fast field decay across the slab

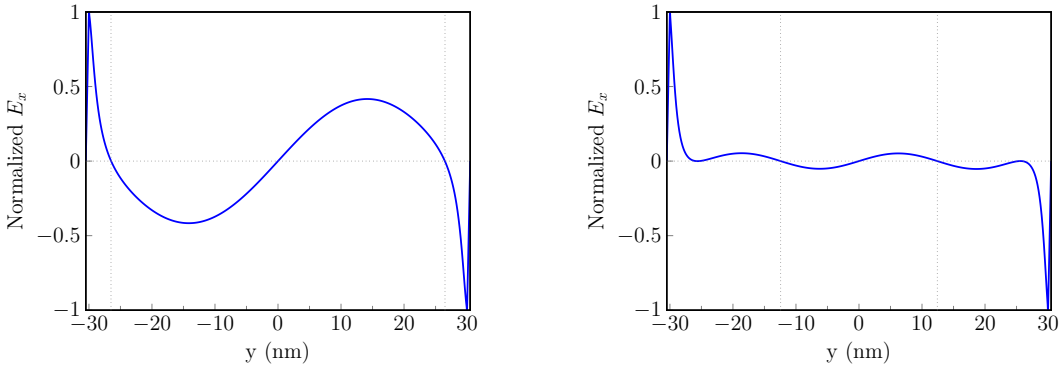


Figure 4.9: Normalized E_x field component along the chain of nanopins at (a) 820 THz and (b) 1049 THz.

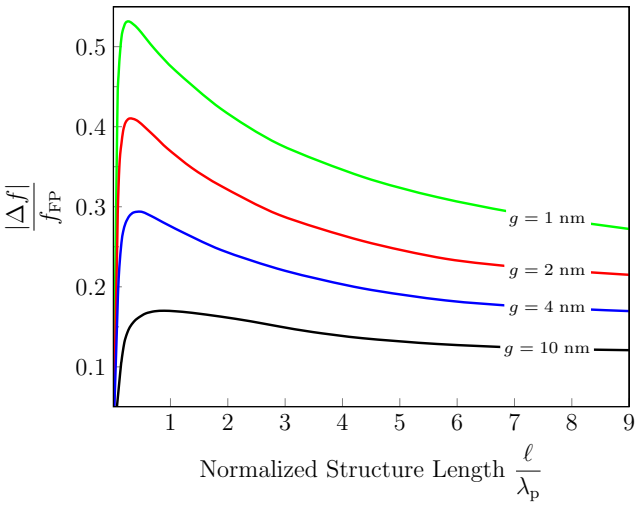


Figure 4.10: Normalized frequency detuning for the first resonance for the infinite chain of coupled nanopins with varying length size.

and hence, no field coupling between parallel surfaces, similar to a single air-metal interface.

Furthermore, in Fig. 4.10, the normalized detuning from the resonant frequency of the free pin $|f_{\mathrm{FP}} - f_{\mathrm{CP}}|/f_{\mathrm{FP}} = |\Delta f|/f_{\mathrm{FP}}$, where f_{FP} and f_{CP} are the first resonant frequencies for the FP and CP, respectively, is plotted against structure size with the gap size as a parameter. All three curves show the same tendency: they start at zero frequency, there is sudden rise for $\ell < \lambda_{\mathrm{p}}/2$, the maxima occur close to $\ell \simeq \lambda_{\mathrm{p}}/2$ and then all curves decline towards zero frequency detuning.

This phenomenon tallies also with the explanation in terms of coupled surface plasmons. When the structure is short (wave number large) all the structures have the same resonant frequency. When the structure is long (wave number small) all the dispersion curves tend to the origin, i.e. they tend to be equal independently of the gap. Thus, a maximum for structure lengths in between is bound to occur: the smaller the gap the higher is the maximum.

4.6 Conclusion

The importance of the gap size in the behaviour of an infinite chain of nanopins has been analyzed thoroughly. Various parametric studies have been undertaken in order to accurately capture and describe its behaviour. The lowest resonance has been calculated using a circuit model but the emphasis in our analysis is on coupling between surface plasmons, a discipline just emerging. The differences between the properties of the free pin and an infinite chain of coupled pins have been studied in detail by investigating their frequency characteristics and plotting the dispersion curves, with strong dependence of the resonant frequencies on the size of the gap having been found. This behaviour can be explained by the amount of coupling between the surface plasmons, suggesting that the origin of the resonances is the same. The results of this work enrich the understanding of the resonances of nanostructures and the corresponding field distributions and may aid the design of nanostructured metamaterials with required properties in the infrared and optical domain.

References

[1] A. Sommerfeld, "Über die fortpflanzung elektrodynamischer wellen langs eines drahtes", *Ann. Phys. Chem.*, vol. 303, pp. 233-290, 1899

[2] U. Fano, "The theory of anomalous diffraction gratings and of quasi-stationary waves on metallic surfaces (Sommerfeld's waves)", *J. Opt. Soc. Am.*, vol. 31, no. 3, pp. 213-222, Mar. 1941

[3] A. A. Oliner and T. Tamir, "Backward waves on isotropic plasma slabs", *J. Appl. Phys.*, vol. 33, no. 1, pp. 231-233, Jan. 1962

[4] E. N. Economou, "Surface plasmons in thin films", *Phys. Rev.*, vol. 182, no. 2, pp. 539-554, Jun. 1969

[5] P. Berini, "Plasmon-polariton modes guided by a metal film of finite width", *Opt. Lett.*, vol. 24, no. 15, pp. 1011-1013, Aug. 1999

[6] P. Berini, R. Charbonneau, N. Lahoud, and G. Mattiussi, "Characterisation of long-range surface plasmon-polariton waveguides", *J. Appl. Phys.*, vol. 98, no. 4, p. 043109, Aug. 2005

[7] S. J. Al-Bader and M. Imtar, "Optical transmission on metallic wires-fundamental modes", *IEEE J. Quant. Electron.*, vol. 40, no. 3, pp. 325-329, Mar. 2004

[8] J. P. Kottmann, O. J. F. Martin, D. R. Smith, and S. Schultz, "Field polarization and polarization charge distributions in plasmon resonant nanoparticles", *New J. Phys.*, vol. 2, 27.1-27.9 Nov. 2000

[9] J. P. Kottmann, O. J. F.Martin, D. R. Smith, and S. Schultz, "Non-regularly shaped plasmon resonant nanoparticle as localized light source for near field microscopy", *J. Microsc.*, vol. 202, no. 1, pp. 60-65, Apr. 2001

[10] J. Aizpurua, P. Hanarp, D. S. Sutherland, M. Kall, G. W. Bryant, and F. J. Garcia de Abajo, "Optical properties of gold nanorings", *Phys. Rev. Lett.*, vol. 90, no. 5, p. 057401, Feb. 2003

[11] J. B. Pendry, "Negative refraction makes a perfect lens", *Phys. Rev. Lett.*, vol. 85, no. 18, pp. 3966-3969, Oct. 2000

[12] W. H. Hardy and L. A. Whitehead, "Split-ring resonator for use in magnetic resonance from 20-2000 MHz", *Rev. Sci. Instrum.*, vol. 52, no. 2, pp. 213-216, Feb. 1981

[13] J. B. Pendry, A. J. Holden, D. J. Robbins, andW. J. Stewart, "Magnetism from conductors and enhanced nonlinear phenomena", *IEEE Trans. Microw. Theory Techn.*, vol. 47, no. 11, pp. 2075-2084, Nov. 1999

[14] R. Marques, F. Medina, and R. Rafii-El-Idrissi, "Role of bianisotropy in negative permeability and left-handed metamaterials", *Phys. Rev. B*, vol. 65, no. 14, p. 144440, Apr. 2002

[15] M. Shamonin, E. Shamonina, V. A. Kalinin, and L. Solymar, "Properties of a metamaterial element: Analytical solutions and numerical simulations for a singly split double ring", *J. Appl. Phys.*, vol. 95, no. 7, pp. 3778-3784, Apr. 2004

[16] M. Shamonin, E. Shamonina, V. A. Kalinin, and L. Solymar, "Resonant frequencies of a split-ring resonator: analytical solutions and numerical simulations", *Microw. Opt. Technol. Lett.*, vol. 44, no. 2, pp. 133-136, Jan. 2005

[17] J. Zhou, T. Koschny, M. Kafesaki, E. N. Economou, J. B. Pendry, and C. M. Soukoulis, "Saturation of the magnetic response of split-ring-resonators at optical frequencies", *Phys. Rev. Lett.*, vol. 95, no. 22, p. 223902, Nov. 2005

[18] R.Marques and M. Freire, "On the usefulness of split ring resonators for magnetic metamaterial design at infrared and optical frequencies", *IEEE MELECON*, pp. 222-224, Malaga, Spain, May 2005

[19] S. Tretyakov, "On geometrical scaling of split-ring and double-bar resonators at optical frequencies", *Metamaterials*, vol. 1, no. 1, pp. 40-43, Mar. 2007

[20] H. Ditlbacher, A. Hohenau, D. Wagner, U. Kreibig, M. Rogers, F. Hofer, F. R. Aussenegg, and J. R. Krenn, "Silver nanowires as surface plasmon resonators", *Phys. Rev. Lett.*, vol. 95, no. 25, p. 257403, Dec. 2005

[21] C. Rockstuhl, T. Zentgraf, H. Guo, N. Liu, C. Etrich, I. Loa, K. Szassen, J. Kuhl, F. Lederer, and H. Giessen, "Resonances of split-ring-resonator metamaterials in the near infrared", *Appl. Phys. B*, vol. 84, no. 1-2, pp. 219-227, Jul. 2006

[22] C. Rockstuhl, F. Lederer, C. Etrich, T. Zentgraf, J. Kuhl, and H. Giessen, "On the reinterpretation of resonances in split-ring-resonators at normal incidence", *Opt. Express*, vol. 14, no. 19, pp. 8827-8836, Aug. 2006

[23] H. Guo, N. Liu, L. Fu, H. Schweizer, S. Kaiser, and H. Giessen, "Thickness dependence of the optical properties of split-ring resonator metamaterials", *Phys. Status Solidi B*, vol. 244, no. 4, pp. 1256-1261, Apr. 2007

[24] E. Tatartschuk, E. Shamonina, and L. Solymar, "Plasmonic excitations in metallic nanoparticles: Resonances, dispersion characteristics and near-field patterns", *Opt. Express*, vol. 17, no. 10, pp. 8447-8460, May 2009

[25] Y. Jing, Z. Jia-Sen, W. Xiao-Fei, and G. Qi-Huang, "Resonant modes of L-shaped gold nanoparticles"', *Chin. Phys. Lett.*, vol. 29, no. 6, p. 067802, 2009

[26] H. Husu, J. Mäkitalo, J. Laukkanen, M. Kuittinen, and M. Kauranen, "Particle plasmon resonances in L-shaped gold nanoparticles", *Opt. Express*, vol. 18, no. 16, pp. 16601-16606, Jul. 2010

[27] H. Husu, J. Mäkitalo, R. Siikanen, G. Genty, H. Pietarinen, J. Lehtolahti, J. Laukkanen, M. Kuittinen, and M. Kauranen, "Spectral control in anisotropic resonance-domain metamaterials", *Opt. Lett.*, vol. 36, no. 12, pp. 2375-2377, Jun. 2011

[28] T. P. Meyrath, T. Zentgraf, and H. Giessen, "Lorentz model for metamaterials': Optical frequency resonance circuits", *Phys. Rev. B*, vol. 75, no. 20, p. 205102, May 2007

[29] T. D. Corrigan, P. W. Kolb, A. B. Sushkov, H. D. Drew, D. C. Schmadel, and R. J. Phaneuf, "Optical plasmonic resonances in split-ring resonator structures: an improved LC model", *Opt. Express*, vol. 16, no. 24, pp. 19850-19864, Nov. 2008

[30] S. I. Maslovski, S. A. Tretyakov and P. A. Belov, "Wire media with negative effective permittivity: a quasi-static model", *Microw. Opt. Technol. Lett.*, vol. 35, no. 1, pp. 47-51, Aug. 2002

[31] G. Dolling, C. Enkrich, M. Wegener, J. F. Zhou, C. M. Soukoulis, S. Linden, "Cut-wire pairs and plate pairs as magnetic atoms for optical metamaterials", *Opt. Lett.*, vol. 30, no. 23, pp. 3198-3200, Dec. 2005

[32] Y. J. Tsai, S. Larouche, T. Tyler, G. Lipworth, N. M. Jokerst and D. R. Smith, "Design and fabrication of a metamaterial gradient index diffraction grating at infrared wavelengths", *Opt. Express*, vol. 19, no. 24, pp. 24411-24423, Nov. 2011

[33] H. Wakatsuchi, J. Paul, S. Greedy and C. Christopoulos, "Cut-wire metamaterial design based on simplified equivalent circuit models", *IEEE Trans. Antennas Propag.*, vol. 60, no. 8, pp. 3670-3678, Aug. 2012

[34] M. A. Ordal, L. L. Long, R. J. Bell, S. E. Bell, R. R. Bell, R. W. Alexander, Jr. and C. A. Ward, "Optical properties of the metals Al, Co, Cu, Au, Fe, Pb, Ni, Pd, Pt, Ag, Ti, and W in the infrared and far infrared", *Appl. Optics*, vol. 22, no. 7, pp. 1099-1119, Apr. 1983

[35] M. A. Ordal, R. J. Bell, R. W. Alexander, Jr., L. L. Long and M. R. Querry, "Optical properties of fourteen metals in the infrared and far infrared: Al, Co, Cu, Au, Fe, Pb, Mo, Ni, Pd, Pt, Ag, Ti, V, and W.", *Appl. Optics*, vol. 24, no. 24, pp. 4493-4499, Dec. 1985

[36] V. Delgado, O. Sydoruk, E. Tatartschuk, R. Marques, M. J. Freire, and L. Jelinek, "Analytical circuit model for split ring resonators in the far infrared and optical frequency range", *Metamaterials*, vol. 3, no. 2, pp. 57-62, Mar. 2009

Chapter 5

Reconfigurable Waveguide Components Using Metamaterials

A new enabling technology for implementing tunable rectangular waveguide components and circuits is reported for the first time with the use of 2D and 3D metamaterials; a holey metal surface and wire media, respectively. Traditional solid metal irises are replaced by a wire medium metamaterial. These media are well known and used to emulate plasma behaviour and, therefore, can be used to replace solid metal. As proof of concepts, results for tunable rectangular waveguide filters are presented with the use of pin block inductive irises and capacitive posts. Furthermore, by adapting the traditional metal-pipe rectangular waveguide for tunability, regions of the solid metal walls are replaced by holey metasurfaces that enable adjustments in the position and spacing of the pin blocks. Prototype tunable structures were measured for verification and good agreement is achieved between full-wave simulations and measurements. The results clearly demonstrate the potential for this tunable/reconfigurable rectangular waveguide enabling technology. Potentially new applications for this permeable enabling technology include lightweight and forced-air/cryogenically-cooled subsystems, gas/vapor/humidity/pressure/light sensors, optoelectronic and even real-time tunable/reconfigurable components, circuits and subsystems.

5.1 Introduction

Rectangular waveguide technologies have been advancing for many decades and find many applications. Traditional metal-pipe rectangular waveguides (MPRWGs) have been used for extremely low loss applications (e.g., low power radio astronomy to high power radar). Other non-extreme power applications have been implemented with substrate integrated waveguides (SIWs); from the original monolithic metal-pipe [1, 2] to the low-cost PCB post-wall (or picket fence) [3] to the next generation of light-pattern-defined "virtual" plasma sidewall REconfigurable Terahertz INtegrated Architecture (RETINA) concept [4, 5] for real-time tunable/reconfigurable applications.

The diverse range of MPRWG components, circuits and subsystems make them essential for many microwave and millimeter-wave applications. However, tuning components/circuits and reconfiguring circuit/subsystem architectures with conventional MPRWG-based technologies can be difficult and/or expensive. To address this issue, tunable metamaterials can be employed [6]. Indeed, the last few decades has seen intensive research in the area of metamaterials with structures having unusual electromagnetic properties. One such material is the so called wire (or rodded) medium, which has been known to emulate plasma behaviour for over half a century [7]. However, it was only recently that a complete physical insight, describing its behaviour, was given [8–10]. The wire medium can replace some of the solid metal parts of rectangular waveguide structures

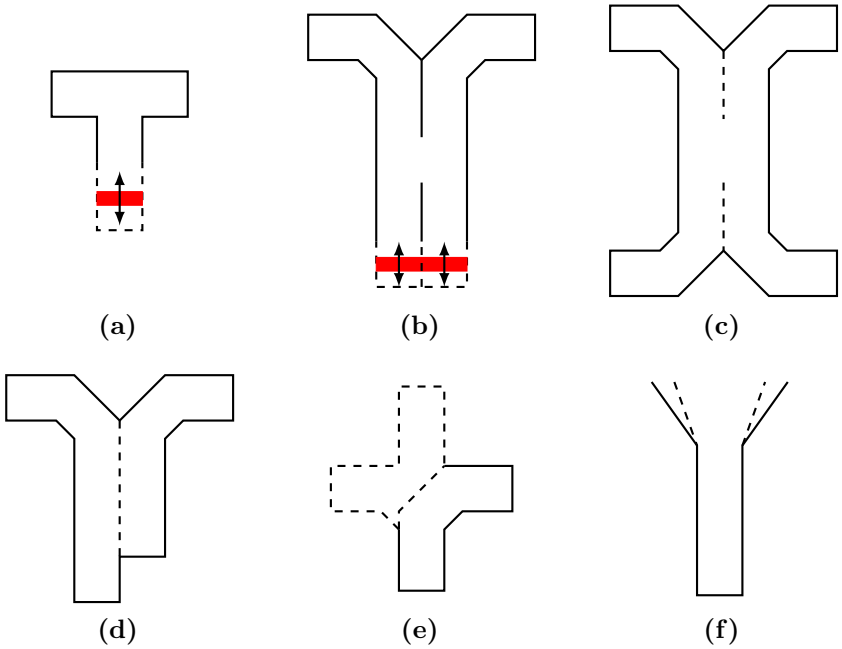


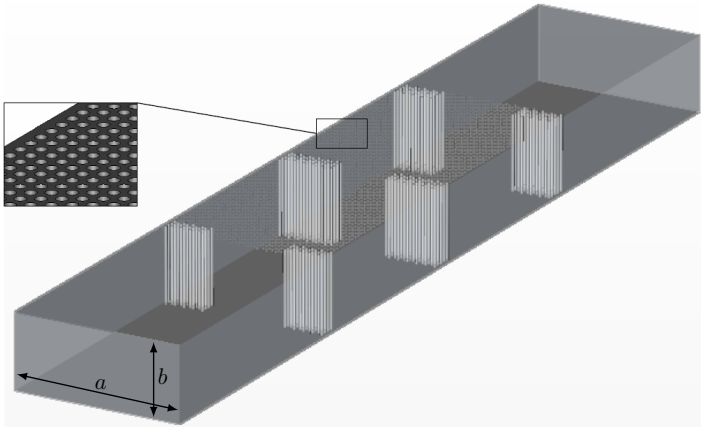
Figure 5.1: Concept illustrations of tunable/reconfigurable waveguide components. (a) short-circuit tuning stub, (b) variable delay line, (c) programmable directional coupler, (d) programmable power splitter, (e) SP3T switch and (f) adjustable H-plane horn antenna. The red sections in (a) and (b) represent moveable pin block. The dashed lines in (c)-(f) represent possible post wall pin configurations.

with the use of pin blocks. This alone is not enough to make tunable devices, as the issue of adjusting the geometric characteristics remain. For this reason, one further modification is required. Regions of the solid waveguide walls can be replaced by holey metasurfaces, patterned with deeply subwavelength holes [11, 12]. The new wall regions provide access to the interior of the waveguide while maintaining its wave-guiding characteristics.

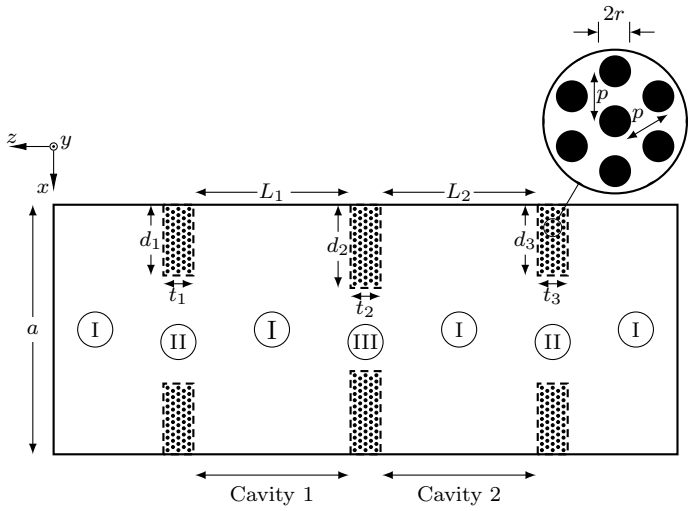
For example, short-circuit tuning stubs can be easily realized by replacing the movable solid metallic end wall with a pin block that can be placed through the holey surface in various positions, as illustrated in Fig. 5.1(a). As a result, variable delay lines are straightforward to implement, as illustrated in Fig. 5.1(b), by adjusting the relative position of such tuning stubs and, thus, controlling the effective propagation path length of the guided wave. Similarly, programmable directional couplers with adjustable coupling aperture and tuning posts can be formed, as illustrated in Fig. 5.1(c), resulting in a change in the coupling coefficient. This concept can also be applied to power splitters, where power ratio can be changed by adjusting their external and internal geometric characteristics, as illustrated in Fig. 5.1(d). For reconfigurable applications N-throw switches can be realized, e.g., the single-pole three-throw (SP3T) switch shown in Fig. 5.1(e), where the position of the pins determines the output. Finally, as shown in Fig. 5.1(f), an adjustable H-plane horn antenna can be realized, where the gain/half-power beamwidth and beam pointing angle of the main lobe can be controlled.

Of course, single- and double-ridged rectangular waveguides can also be implemented, by partially penetrating pins within the waveguide (in the case of double-ridged waveguides both top and bottom walls need to be replaced by the holey metasurface); the penetration depth offers the flexibility of being able to adjust the capacitive loading and hence the guiding properties of the waveguide.

Among the most widely used rectangular waveguide circuits are filters, which can be implemented in a variety of ways; for example, employing inductive and/or capacitive irises, septa or posts [13–16].



(a)



(b)

Figure 5.2: Proposed filter geometry. (a) Perspective view and (b) plan view.

For the purposes of demonstrating tunable waveguide circuits using holey surfaces and pin block metamaterials, filters employing inductive irises will be reported, although capacitive irises, septa and posts could also have been used.

5.2 Filter Design

The design of inductive iris filters is well-known and in some cases they can also be investigated analytically. However, a quick way to design such filters is by full-wave simulations or even free online available applets [17]; the latter approach was used here during the initial design. Fig. 2 shows illustrations of a 2-pole tunable inductive iris filter. A metal sheet patterned with an array of holes (arranged in a triangular lattice) to create the metasurface is used to replace small sections of one or more of the traditional MPRWG walls. In addition, the traditional solid internal field-perturbing metallic elements have been replaced by pin blocks. The result is the implementation of a band pass filter having tunable characteristics from the (re-)positioning of individual pins. The holey metasurface provides the required good electrical characteristics (i.e., sufficiently high conductivity) while enabling to reconfigure the structure mechanically (e.g., by inserting/removing pins through the holes).

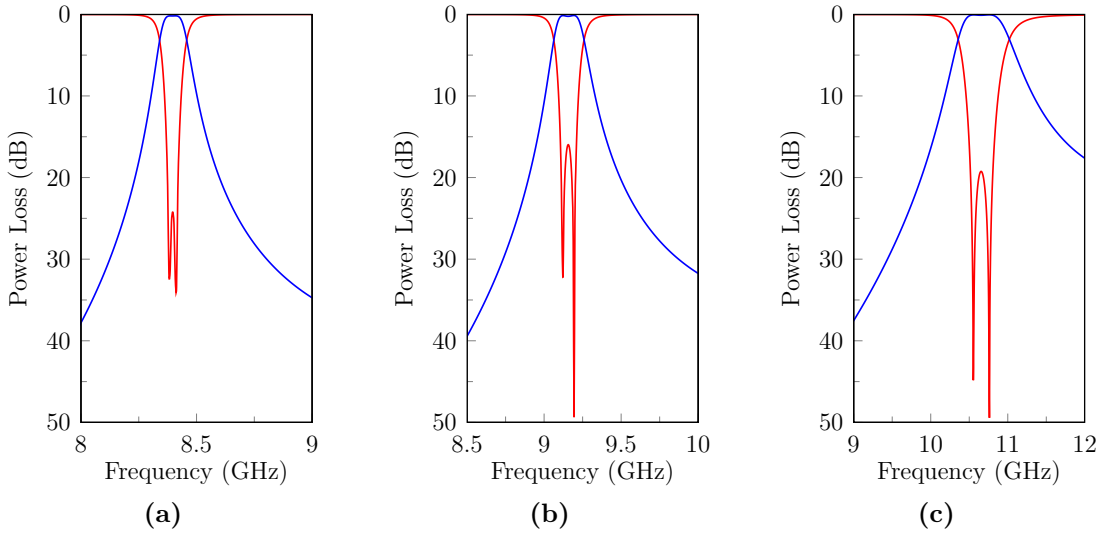


Figure 5.3: Numerical simulation results of transmission (blue curves) and reflection (red curves) power loss characteristics for a tunable filter using the parameters given in Table 5.1, having its center frequency tuned for (a) 8.4 GHz, (b) 9.2 GHz and (c) 10.6 GHz.

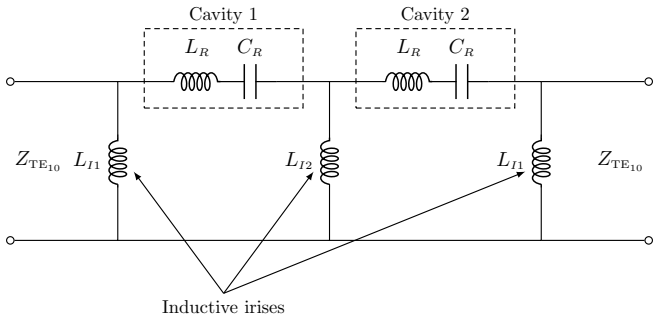


Figure 5.4: Ideal lumped-element equivalent circuit model for the 2-pole filter demonstrator.

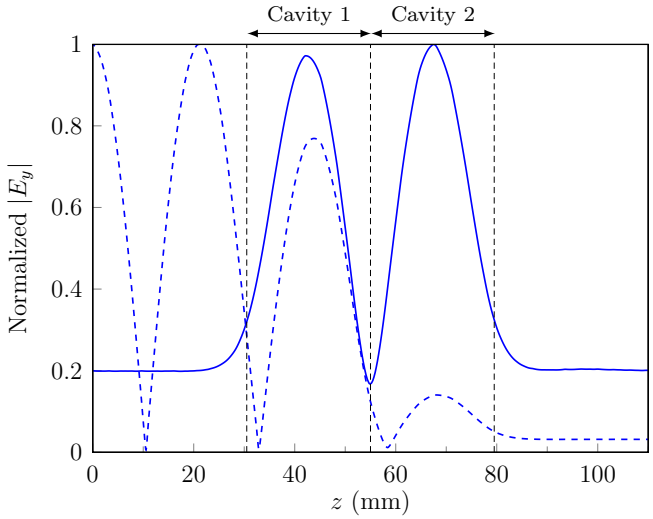
Metallic cylindrical pin arrays penetrate the waveguide, via the holes of the metasurface, to create pin block regions that behave as solid metal blocks from a traditional inductive iris, as illustrated in Fig. 5.2. The physical length of the pins is equal to the external height of the waveguide, with their radius ideally matching that of the holes from the metasurface. The holes have deeply subwavelength dimensions, with respect to the guide wavelength (i.e., $r \ll \lambda_g$ where r and λ_g are the radius of the holes and the guide wavelength, respectively) and are arranged in a triangular lattice to minimize the spacing between adjacent pins; maximizing the pin block density and resolution of the individual pin positions. The former is important in order for the pin blocks to better mimic the low loss behaviour of the solid blocks; while the latter enables finer tuning resolution.

Due to the perforated periodic pattern of the metasurface, the size and position of the inductive irises can be altered by changing the density and individual positions of pins and, therefore, the pass band can be easily tuned.

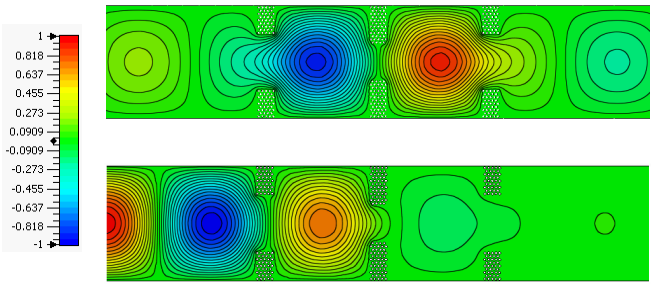
For simplicity, the waveguide is operating at the fundamental TE_{10} mode (only E_y, H_x, and H_z are non-zero), so that higher order modes are cut off. Thus, the pins have to be placed vertically (parallel to the electric field) in order for E_y to induce currents along the pins and hence strongly interact with them. It is well known that wave-guiding structures containing discontinuities can be

Table 5.1: Spatial dimensions (in mm) of the proposed filter corresponding to triangular lattice hole/pin positions.

$\mathbf{f_0}$	**a**	**b**	**p**	**r**	$\mathbf{L_1 = L_2}$	$\mathbf{d_1 = d_3}$	$\mathbf{d_2}$	$\mathbf{t_1 = t_3}$	$\mathbf{t_2}$
8.4 GHz	23	10	0.75	0.25	24.5	5.82	7.79	2.75	3.5
9.2 GHz	23	10	0.75	0.25	19.5	5.82	7.79	3.5	3.5
10.6 GHz	23	10	0.75	0.25	14.5	5.82	7.12	3.125	3.5



(a)



(b)

Figure 5.5: (a) Numerical simulation results of normalized magnitude of E_y in the pass band at 9.2 GHz (solid curves) and outside the pass band at 9.5 GHz (dashed curves) and (b) corresponding contour plots of Ey in the pass band (top) and outside the pass band (bottom), respectively.

studied analytically using mode-matching techniques. If this technique is applied for the design shown in Fig. 5.2, where the waveguide is partitioned into several sections, the fields in each section are expanded in normal waveguide modes and the continuity of the fields is enforced at the interfaces. A thorough analysis is beyond the scope of this work and can be found in many standard textbooks (e.g., [18, 19]).

5.2.1 Band Pass Filter

A 2-pole X-band tunable band pass filter will first be simulated with the use of a rectangular waveguide having approximate internal width a and height b spatial dimensions of $a \times b = 23$ mm $\times$

10 mm (i.e., similar to a standard WR-90 waveguide), with the whole of the top wall (as an extreme case) replaced by the holey metasurface.

To create a 2-pole filter, two cavity regions require six pin blocks inside the rectangular waveguide. For this particular filter design, symmetry exists in the x-z plane at $x = a/2$ and also in the x-y plane at the center of the filter. Therefore, the physical length of each cavity $L_1 = L_2 = L$ and the first and third irises have the same effective spatial dimensions of depth ($d_1 = d_3$) and thickness dimensions ($t_1 = t_3$). The nominal physical dimensions of the designed structures are given in Table 5.1.

This metamaterial filter has the important advantage in that it can be easily tuned, where the pass band can be translated across the entire X-band. The resonant frequency of the cavities (which defines the center frequency of the pass band f_0) is mainly affected by separation distance L. However, in order to fine tune the performance of the filter, other parameters can be adjusted, as will be discussed later. As an example, the results of full-wave numerical simulations using CST Microwave Studio (MWS) are shown in Fig. 5.3, for a filter having holey surfaces and pin block metamaterials defined by the physical dimensions given in Table 5.1.

Moreover, but not shown here, the bandwidth of the pass band can just as easily be controlled by varying the depths d_1, d_2, d_3 to achieve the required coupling coefficient, by tuning levels of shunt inductive coupling.

A lumped-element equivalent circuit model for the 2-pole filter demonstrator is shown in Fig. 5.4. It consists of two directly coupled series $L_{\mathrm{R}}C_{\mathrm{R}}$ resonators, which describe the identical cavity resonators in the waveguide filter, and three inductive coupling elements that correspond to the inductive irises (i.e., L_{I1} and L_{I2}) formed by the pin blocks. Finally, $Z_{\mathrm{TE}_{10}} = \omega\mu/k_z$ is the transverse wave impedance for the dominant TE_{10} mode, with μ being the magnetic permeability of the waveguide filler (i.e., air in this case, with $\mu = \mu_0$), $k_z = \sqrt{k_0^2 - (\pi/a)^2}$ is the wavevector for the TE_{10} mode along the direction of propagation and the phase constant in free space $k_0 = \omega/c$, with ω and c being the angular frequency and the speed of light in free space, respectively.

Numerical simulation results clearly show that, within the pass band, both cavities are excited at resonance and most of the power propagates along and through the waveguide. Moreover, the physical spacing L is approximately half the guided wavelength, as seen in Fig. 5.5. Conversely, outside the pass band, the cavities are excited but the evanescent electric field decays exponentially through the cavities; the result is that the output power is just a small fraction of the input power.

To further investigate the performance of the holey surfaces and pin block metamaterials filter, and understand the effect of the various design parameters on its operation, parametric analysis has been undertaken, with some results shown in Fig. 5.6. Specifically, Figs. 5.6(a) to 5.6(d) were obtained by adding/removing a row of pins in the dimension of interest. It can be seen that resonance is sensitive to changes in d_1, d_2 and t_2; even small variations in these parameters may completely distinguish the resonance. However, t_1 can be used to fine tune the pass band characteristics. As expected, different scenarios can yield similar results. For example, Figs. 5.6(e) and 5.6(f) show that appropriate combinations for the values of d_1 and d_2 can shift the pass band, similar to adjusting the length L (i.e., increasing d_1 and d_2 increases the shunt inductance, which effectively reduces the electrical length of the cavities, similar to reducing L). Thus, there are many degrees of freedom that can be used to tune the filter.

5.2.2 Band Stop Filter

Another example of a simple tunable device is that of a band stop filter, realized by employing capacitive posts [16]. Even a single pin that partially penetrates the inside of the waveguide can be used to implement the band stop characteristic [16]. The center frequency can be tuned by adjusting the penetration ratio h/b of the pin, where h is the internal penetration length of the pin

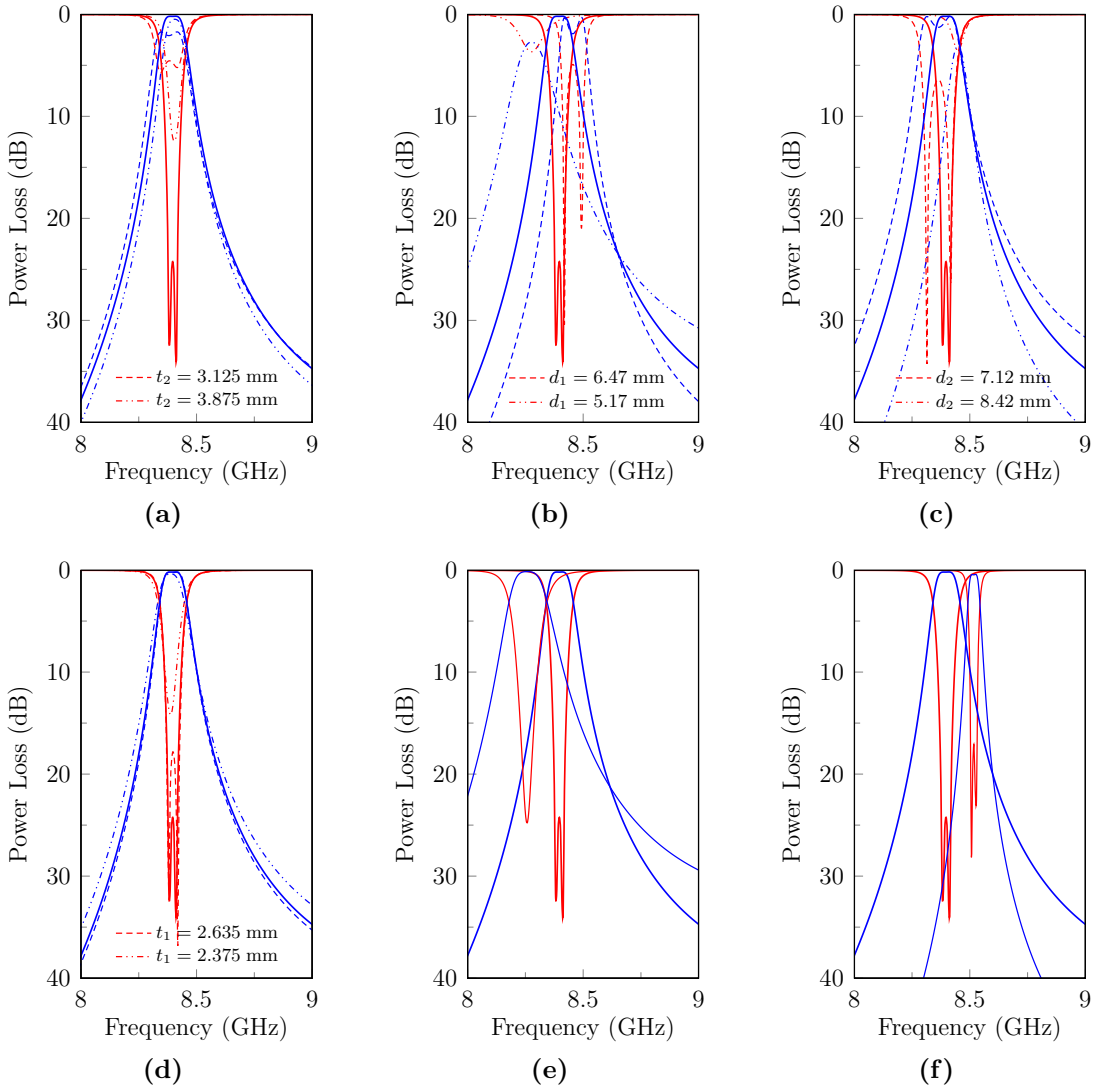


Figure 5.6: Numerical simulation results of transmission (blue curves) and reflection (red curves) power loss characteristics for various parametric studies. Thick lines correspond to the values shown in Table 5.1: (e) $d_1 = 5.17$ mm, $d_2 = 7.12$ mm and (f) $d_1 = 6.47$ mm, $d_2 = 8.42$ mm.

(the smaller the ratio, the higher the tuned frequency), as can be seen in Fig. 5.7.

5.3 Manufactured Proof-of-Concept Demonstrators

5.3.1 Band Pass Filter

A prototype of the 2-pole tunable filter, described in Section II, has been fabricated. A single 0.5 mm thick perforated aluminum sheet having periodically arranged holes; (with diameter $2\,r = 0.5$ mm, in triangular lattice and with 1 mm periodicity) has been wrapped around a standard WR-90 rectangular waveguide filler, as shown in Fig. 5.8(a). The longitudinal gap along the length of the waveguide was sealed with a narrow strip of conductive aluminum tape. The joint was placed in the center of the broad wall of the waveguide (where the electric field is at a maximum for the fundamental mode), in order to ensure a good electrical connection at the critical locations

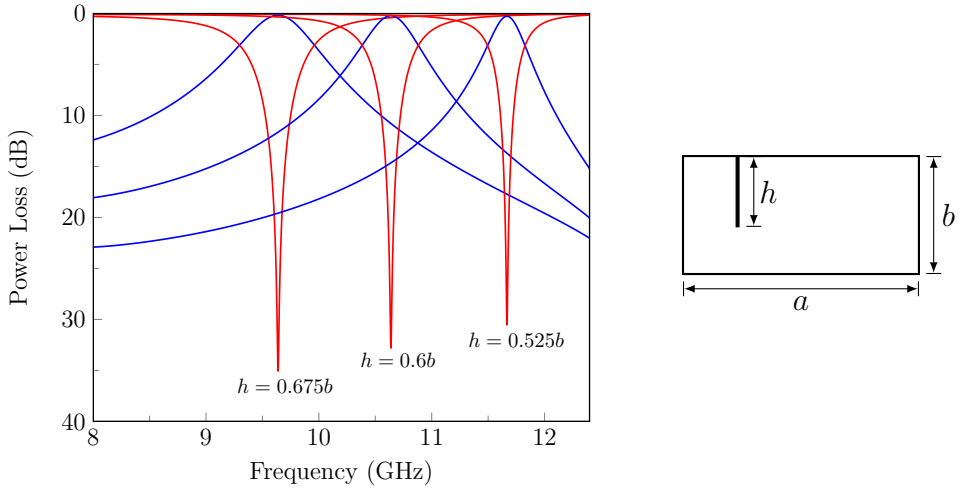


Figure 5.7: Left: Numerical simulation results of transmission (blue curves) and reflection (red curves) power loss characteristics for various penetration ratio values. Right: Cross-sectional view.

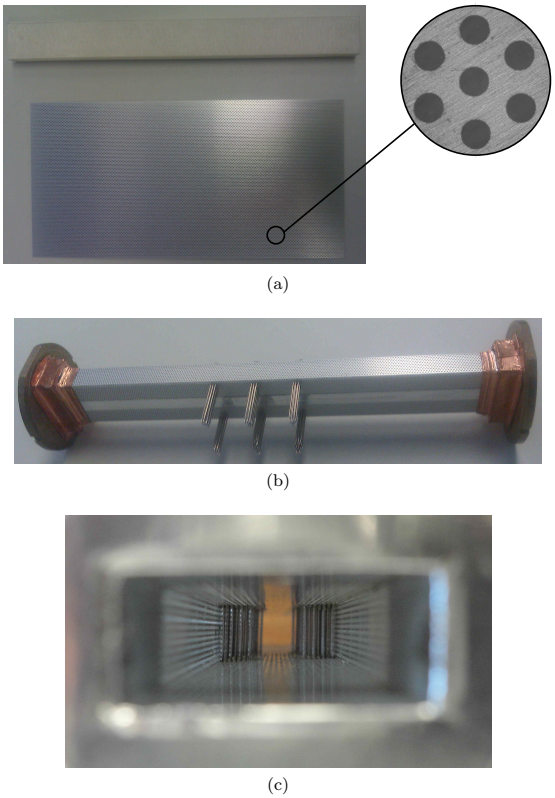


Figure 5.8: (a) Above: modified WR-90 dielectric filler (used as a temporary former) and below: flat 20×10 cm^2 perforated aluminum sheet (before assembly), (b) underside of the prototype filter (where the aluminum tape, protruding pins and standard WR-90 flanges can be seen) and (c) transverse view through the filter (showing the pin blocks and metasurfaces on all four walls running along the entire length of the 20 cm long rectangular waveguide).

where the electric field is zero. Next, 0.5 mm diameter stainless steel pins are inserted through the rectangular waveguide, in order to form the pin blocks for the inductive irises, as shown in Fig.

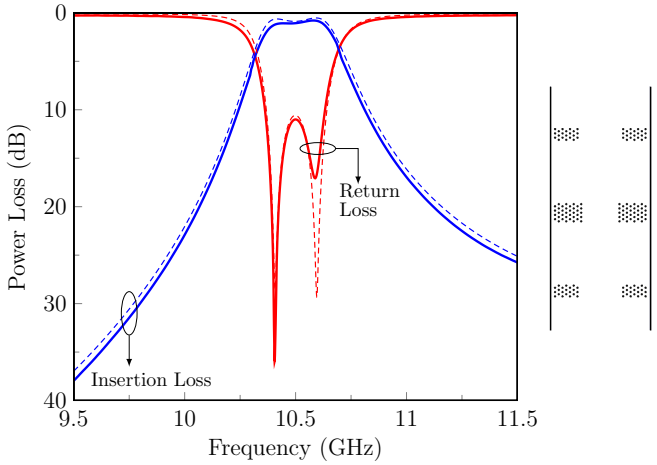


Figure 5.9: Left: Chebyshev filter responses. Solid lines: measured results. Dashed lines: full-wave numerical simulation results using CST MWS. Right: individual pin arrangement with $L = L_1 = L_2 = 14.5$ mm.

5.8(b) and 5.8(c); after tuning, the pins are secured in place with conductive epoxy glue.

Measurements were undertaken at the UK's National Physical Laboratory, using a vector network analyzer (VNA) having a pair of WR-90 waveguide test ports and associated traceable calibration standards, for accurate S-parameter measurements across the 8.2 to 12.4 GHz frequency range. Thru-Reflect (short)-Line (TRL) calibration [20] establishes the measurement reference planes at the waveguide test ports. The calibration was performed using an external calibration algorithm, employing a seven-term error-correction routine [21]. The complete measurement set-up (i.e., VNA, primary standards and calibration algorithm) is referred to as the NPL Primary Impedance Microwave Measurement System (PIMMS) [22, 23], and represents the UK's primary national standard system for S-parameter measurements. PIMMS also determines the uncertainty in the S-parameter measurements. This is achieved following internationally agreed guidelines [24], with minor modifications to accommodate the complex-valued (i.e., vector) nature of the S-parameter measurands [25]. For measurements in WR-90 waveguide, uncertainties of the linear magnitude of transmission coefficients typically range from 0.0003 to 0.0005 for a nominal transmission of 0.1 (i.e., 20 dB) in this waveguide band. Similarly, uncertainties for measurements of the linear magnitude of reflection coefficients typically range from 0.001 to 0.003 for low reflecting devices.

As can be seen in Fig. 5.9, a 2^{nd} order Chebyshev filter response, having two return loss zeros, is obtain when $d_1 = d_3 = 6.4$ mm, $d_2 = 7.3$ mm, $t_1 = t_3 = 3$ mm and $t_2 = 4.5$ mm, whereas Fig. 5.10 shows the filter tuned to have a Butterworth type response. This can be achieved by changing the inductive coupling elements (i.e., changing the number and location of pins). Here, for example, $d_1 = d_2 = 6.5$ mm, $d_3 = 4.6$ mm and $t_1 = t_2 = t_3 = 3$ mm. The agreement between simulated and measured results is excellent in both cases, with only small discrepancies being attributed to manufacturing tolerances on the specified dimensions. The 1.4 % shift in frequency can be easily corrected by a small increase in $L = L_1 = L_2 = 15$ mm.

It is interesting to note that the in-band insertion losses for both filters are approximately 0.5 dB in X-band, which includes the use of non-ideal metals (i.e., lossy aluminium for the holey metasurfaces and stainless steel for the pin blocks) and the additional contributions from the two superfluous 13.1 cm long aluminium holey metasurface feed lines; clearly indicating that this technology is inherently low loss. Obviously, the insertion loss performance for these filters can be improved by using copper (instead of both aluminum and stainless steel) and removing the long feed lines.

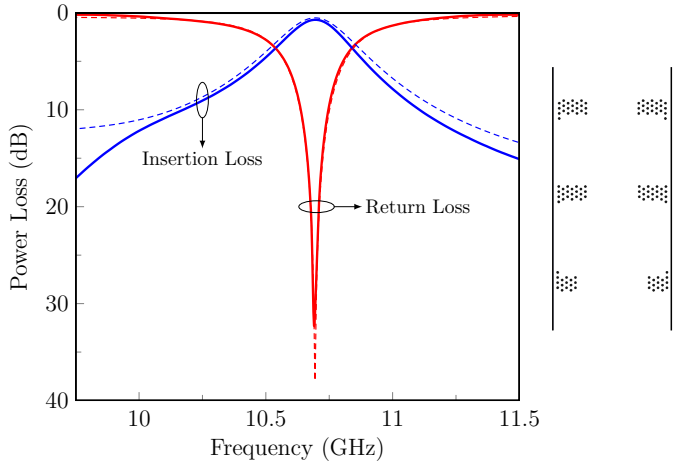


Figure 5.10: Left: Butterworth filter responses. Solid lines: measured results. Dashed lines: full-wave numerical simulation results using CST MWS. Right: individual pin arrangement with $L = L_1 = L_2 = 14.8$ mm.

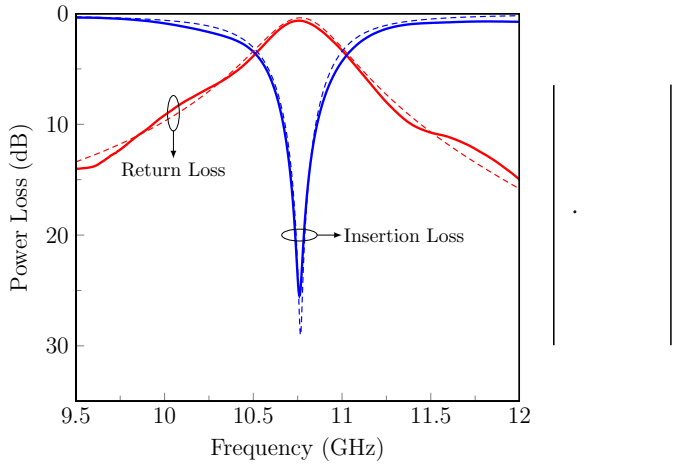


Figure 5.11: Left: Single capacitive post pin band stop filter responses. Solid lines: measured results. Dashed lines: full-wave numerical simulation results using CST MWS. Right: single pin having a penetration ratio $h/b = 0.59$ and 3.7 mm offset from center.

5.3.2 Band Stop Filter

Next, a prototype of a simple single-pole band stop filter is fabricated by inserting a single pin partially inside an unperturbed rectangular waveguide, as described previously. The pin is located off center [16]. The response of this device is shown in Fig. 5.11, where the agreement between simulated and measured results is again excellent. The peak value of in-band return loss is approximately 0.6 dB.

5.3.3 Single Resonator

Taking advantage of the structure's flexible arrangement for tunability, a single cavity resonator has been created by placing two double-rows of pins across the transverse width of the waveguide, separated by a distance $L = 15.3$ mm. Thus, the textbook value for the lossless resonant frequency of the dominant fundamental TE_{101} mode can be approximated by the well-known expression $f_{101} = \frac{c}{2\pi}\sqrt{(\pi/a)^2 + (\pi/L)^2}$. In order to increase the coupling efficiency, the middle pin of each

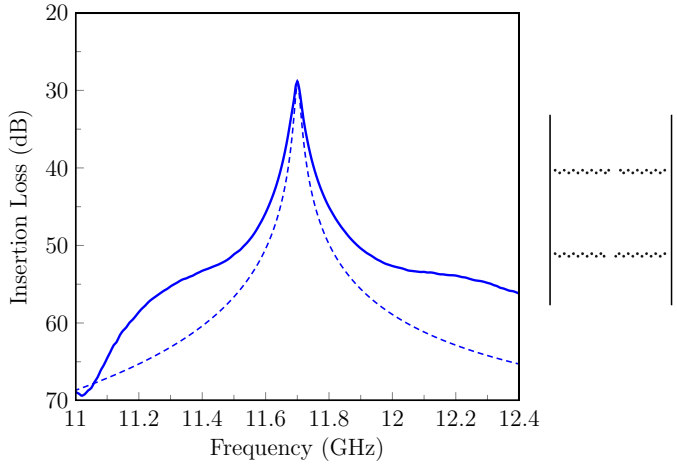


Figure 5.12: Left: Cavity resonator insertion loss responses. Solid lines: measured results. Dashed lines: full-wave numerical simulation results using CST MWS. Right: pin arrangement with internal spatial dimensions of $a \times b \times L = 23 \times 10 \times 15.3$ mm^3.

Table 5.2: Loaded and unloaded quality factors for the cavity shown in Fig. 5.12.

	Simulated	**Measured**
Unloaded $Q_{\mathrm{u}}(f_0)$	698	419
Loaded $Q_{\mathrm{L}}(f_0)$	677	402

row is removed. Further pins can be removed, in order to obtain stronger coupling, but at the expense of decreasing the loaded quality factor. On the other hand, the loaded quality factor is increased if none of the pins are removed (i.e., weaker coupling). The simulated and measured responses for this simple resonant structure are shown in Fig. 5.12, where any discrepancy between simulated and measured values is due to the poor repeatability of our simple prototype.

The loaded quality factor $Q_{\mathrm{L}}(f_0)$ can be obtained from the transmission coefficient, either using the -3 dB bandwidth (i.e., $Q_{\mathrm{L}}(f_0) = \Delta f / f_0$, where Δf and f_0 are the -3 dB bandwidth and the resonant frequency, respectively) or from the insertion phase frequency response by

$$Q_{\mathrm{L}}(f_0) = \frac{f_0}{2} \frac{\partial \angle S_{21}(f)}{\partial f} \bigg|_{f=f_0} \tag{5.1}$$

Both definitions are equivalent for large Q_{L} and give the same result (within a small numerical margin of error). The unloaded quality factor $Q_{\mathrm{u}}(f_0)$ can be calculated by taking into account the loading of the cavity from

$$Q_{\mathrm{u}}(f_0) = \frac{Q_{\mathrm{L}}(f_0)}{1 - |S_{21}(f_0)|} \tag{5.2}$$

The results for both $Q_{\mathrm{L}}(f_0)$ and $Q_{\mathrm{u}}(f_0)$ are given in Table 5.2. As can be seen, there is a difference between simulated and measured results for such high Q-factor resonators. This is mainly because of pin misalignment with our simple prototypes (since there are only two rows of pins). However, when the unloaded quality factor is compared with classical waveguide resonators (i.e., fixed structures having no tuning ability), there is a reduction in performance. This is because tunability comes at the cost of increased losses both via radiation through the holes and power leakage through the rows of pins (i.e., power that does not contribute to the resonance). Fortunately, these losses can be dramatically reduced by: (1) decreasing the size of the holes (e.g., using more

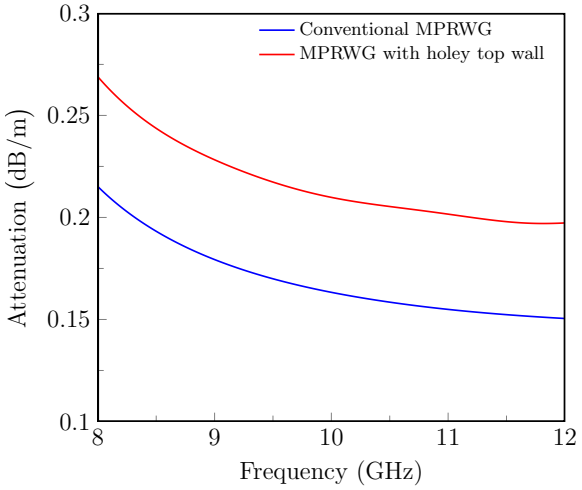


Figure 5.13: Numerical simulation results of attenuation per guided wavelength in X-band for a conventional aluminum ($\sigma_0 = 3.56 \cdot 10^7$ S/m) WR-90 rectangular waveguide and one whose top wall is replaced by the proposed holey metasurface having dimensions given in Table 5.1.

sophisticated machining technology), (2) having only a small section of the waveguide patterned with such holes and (3) increasing the pin density.

5.4 Extraction of Attenuation Constant

When evaluating the power losses in structures with discontinuities using full-wave simulations, one has to be careful with the interpretation of the results generated. For example, a standard approach to analyze the performance of waveguides is by exciting them with a waveguide port placed at each end. This approach calculates the attenuation constant and the S-parameters for the device modeled. However, the attenuation constant may report lower losses when compared to those reported by S_{21}. The inconsistency in the results is due to the way the software calculates the propagation constant (and hence the attenuation constant). The propagation constant is evaluated at the face at which a port is assigned with a 2D eigenmode solver being employed to calculate the supported modes by the structure. As a result, this approach may yield incorrect results when the port is assigned to a face with discontinuities. More accurate results can be obtained from the S-parameters, as described here. For a generic passive system the energy conservation states that the incident power P_{inc} has to be equal with the summation of the reflected (due to impedance mismatching) and transmitted power P_{ref} and P_{tr}, respectively and the power being lost P_{loss} (i.e., dissipated as heat or radiated). Thus, $P_{\text{inc}} = P_{\text{ref}} + P_{\text{tr}} + P_{\text{loss}}$. Now, from the definition of the S-Parameters for a two-port network one gets $\dfrac{P_{\text{ref}}}{P_{\text{inc}}} \equiv |S_{11}|^2$ and $\dfrac{P_{\text{tr}}}{P_{\text{inc}}} \equiv |S_{21}|^2$, whereas using well-known perturbation methods the power transmitted from a point located at z_1 to z_2 is given by

$$P_{\text{tr}}(z_1) = P_{\text{tr}}(z_2) e^{-2\alpha(z_2 - z_1)} \tag{5.3}$$

In our case, for single mode propagation and assuming that the power enters the structure at z_1 and exits at z_2, having traveled a distance $L = z_2 - z_1$, (5.3) can be solved for the attenuation constant α as follows (for negligible reflections)

$$\alpha = -\frac{10}{L}\left[\log|S_{21}|^2 - \log\left(1 - |S_{11}|^2\right)\right] = -\frac{20}{L}\log|S_{21}| \qquad \text{in [dB/L]} \tag{5.4}$$

5.5 Discussion

The holey metasurface can be described as an effective medium, using homogenization concepts, having an effective conductivity σ_{eff} dictated by a filling factor; being naturally lower than the bulk dc conductivity σ_0 of conventional solid walls (i.e., $\sigma_{\text{eff}} < \sigma_0$). Although such a structure can expect to have slightly higher losses, due to the small amount of radiation through the holes, when compared with a conventional MPRWG, the losses can be dramatically reduced.

Fig. 5.13 shows the attenuation of the proposed waveguide having a metasurface on the whole of its top wall (without any pins) and a conventional MPRWG. In practice, the losses can be reduced almost back to the levels of the conventional MPRWG by covering the remaining holes with a conductive adhesive metal foil after tuning with simple physical or automated actuation mechanisms.

5.6 Conclusion

A new and generic enabling technology for realizing rectangular waveguide-based tunable components and circuits, which combines 2D and 3D metamaterials (holey metasurfaces and pin blocks, respectively), has been demonstrated. Two classical filter implementations have been demonstrated. The first employs tunable inductive iris to retune from the Chebyshev to Butterworth approximations for a 2-pole band pass filter; while the second employs a capacitive post to achieve a band stop filter characteristic having a single-pole Butterworth approximation.

The parametric study has shown robustness to the restriction of pin location and manufacturing tolerances. Moreover, with its large degrees of tuning freedom, which lends itself to automation, this technology can achieve high levels of functionality. Moreover, the measured low loss performances of the experimental filters, as well as the high Q-factors for a single resonator, given the non-ideal lossy metals used, clearly demonstrate that this new metamaterials technology can provide a low cost solution for tunable and reconfigurable architectures.

The proposed technology may find many applications that are not just limited to high performance filters that have restrictions on manufacturing tolerances [26, 27]. Many types of discontinuity can be easily introduced by inserting pins either fully or partially into the rectangular waveguide and in all three orthogonal planes. For example, tunable ridged waveguides is one possible application. Moreover, the post-wall SIW, with its diverse array of component and circuits, including all the examples illustrated in Fig. 1, is a natural application of this technology, as the sidewall vias can be replaced by tunable pin arrays with block actuators.

Finally, potentially new applications for this permeable enabling technology include lightweight and forced-air/cryogenically-cooled subsystems, gas/vapor/humidity/pressure/light sensors, optoelectronic and even real-time tunable/reconfigurable components, circuits and subsystems. Here, a resonance or series of resonances can be implemented and the resulting frequency detuning and reduction in quality factors can be detected, giving valuable information on the particular parameter under test.

It is interesting to note that compared to conventional filters with fixed apertures and tuning screws, the proposed method offers the opportunity to realize a more diverse range of devices and hence, with one reconfigurable architecture the implementation of a broad range of passive components (not restricted to filters) is possible.

References

[1] S. Lucyszyn, Q. H. Wang and I. D. Robertson, "0.1 THz rectangular waveguide on GaAs semi-insulating substrate", *IEE Electron. Lett.*, vol. 31, no. 9, pp. 721-722, Apr. 1995

[2] S. Lucyszyn, D. Budimir, Q. H. Wang and I. D. Robertson, "Design of compact monolithic dielectric-filled metal-pipe rectangular waveguides for millimetre-wave applications", *IEE Proc. - Microw. Antennas Propag.*, vol. 143, no. 5, pp. 451-453, Oct. 1996

[3] K. Wu, "Integration and interconnect techniques of planar and nonplanar structures for microwave and millimeter-wave circuits current status and future trend", *Asia Pacific Microwave Conference*, pp. 411-416, 2001

[4] . S. Lucyszyn and Y. Zhou, "Reconfigurable Terahertz Integrated Architecture (RETINA)", *33rd International Conference on Infrared, Millimeter, and Terahertz Waves*, Pasadena, USA, Sep. 2008

[5] Y. Zhou and S. Lucyszyn, "Modelling of reconfigurable terahertz integrated architecture (RETINA) SIW structures", *PIER*, vol. 105, pp. 71-92, Jun. 2010

[6] K. Herbertz and S. Lucyszyn, "Electromagnetic bandgap filter with single-cell monolithic microwave integrated circuit-tuneable defect", *IET Microw. Antennas Propag.*, vol. 4, no. 8, pp. 1123-1131, Aug. 2010

[7] W. Rotman, "Plasma simulation by artificial dielectrics and parallel-plate media", *IRE Trans. Antennas Propag.*, vol. 10, pp. 82-95, Jan. 1962

[8] M. G. Silveirinha, "Nonlocal homogenization model for a periodic array of ε-negative rods", *Phys. Rev. E*, vol. 73, p. 046612, Apr. 2006

[9] M. G. Silveirinha and C. A. Fernandes, "Transverse-average field approach for the characterization of thin metamaterial slabs", *Phys. Rev. E*, vol. 75, p. 036613, May 2007

[10] S. I. Maslovski and M. G. Silveirinha, "Nonlocal permittivity from a quasistatic model for a class of wire media", *Phys. Rev. B*, vol. 80, p. 245101, Dec. 2009

[11] D. Ramaccia, F. Bilotti and A. Toscano, "Analytical model of metasurface consisting of a regular array of sub-wavelength circular holes in a metal sheet", *PIER M*, vol. 18, pp. 209-219, 2011

[12] D. Ramaccia, G. Bellaveglia and R. L. Forti, "Inductive tri-band double element FSS for space applications", *PIER C*, vol. 18, pp. 87-101, 2011

[13] Y. Zhai, Q. Wang, Z. Wang and X. X. Gao, "The design of an iris filter at 37.5 GHz", *Global Symposium on Millimeter Waves 2008*, pp. 348-350

[14] S. Li, J. Fu, X. Wu, "Analysis of high-power rectangular waveguide filter with capacitive coupling iris for satellite", *APPEEC*, 2009

[15] R. Gesche and N. Loechel, "Two cylindrical obstacles in a rectangular waveguide–resonances and filter applications", *IEEE Trans. Microw. Theory Techn.*, vol. 37, no. 6, pp. 962-968, Jun. 1989

[16] U. Rosenberg and S. Amari, "A novel band-reject element for pseudoelliptic bandstop filters", *IEEE Trans. Microw. Theory Techn.*, vol. 55, no. 4, pp. 742-746, Apr. 2007

[17] http://www.guidedwavetech.com/wgchoose.htm

[18] R. E. Collin, "Field theory of guided waves", 2nd ed., *IEEE Press*, 1991

[19] C. A. Balanis, "Advanced engineering electromagnetics", *Wiley*, 1989

[20] G. F. Engen and C. A. Hoer, "Thru-Reflect-Line: An improved technique for calibrating the dual six port automatic network analyser", *IEEE Trans. Microw. Theory Techn.*, vol. 27, no. 12, pp. 987-993, Dec. 1979

[21] A. Rumiantsev and N. M. Ridler, "VNA calibration", *IEEE Microw. Mag.*, vol. 9, no. 3, pp. 86-99, Jun. 2008

[22] N. M. Ridler, "A review of existing national measurement standards for RF and microwave impedance parameters in the UK", *IEE Colloquium Digest*, no. 99/008, pp. 6/1-6/6, Feb. 1999

[23] N. M. Ridler, "News in RF impedance measurement", *XXVII General Assembly of the International Union of Radio Science (URSI)*, Maastricht, Aug. 2002

[24] ISO/IEC Guide 98-3:2008, "Uncertainty of Measurement – Part 3: Guide to the expression of the Uncertainty in Measurement (GUM:1995)", *International Organization for Standardization*

[25] N. M. Ridler and M. J. Salter, "An approach to the treatment of uncertainty in complex S-parameter measurements", *Metrologia*, vol. 39, no. 3, pp. 295-302, Jun. 2002

[26] C. Chrisostomidis and S. Lucyszyn, "On the theory of chained-function filters", *IEEE Trans. Microw. Theory Techn.*, vol. 53, no. 10, pp. 3142-3151. Oct. 2005

[27] C. Chrisostomidis and S. Lucyszyn, "Seed function combination selection for chained function filters", *IET Microw. Antennas Propag.*, vol. 4, no. 6, pp. 799-807, Jun. 2010

Chapter 6

Reconfigurable "Voodoo" Waveguide for Single Element Vector Network Analyzer Verification

Following the concept presented in Chapter 5, a novel simple metamaterial inspired approach to the verification process for vector network analyzer (VNA) waveguide calibration is investigated here, using a single reconfigurable component verification kit. Conventional techniques require multiple verification components and these only exist commercially for operation up to 110 GHz. At millimeter-wave frequencies, the use of multiple components can lead to significant errors due to imperfections in waveguide flange misalignments during the multiple component connections. The reconfigurable component has been designed so that its electrical properties can be changed quickly to a broad range of known values, without introducing additional errors due to flange misalignment. Once connected, the component can be reconfigured to introduce relative changes in the reflected and transmitted signals. For millimeter-wave metrology, where mechanical precision is of paramount importance, this single-component verification approach represents an attractive solution. A proof-of-concept verification process is described, based on hardware implementation, simulations and validation measurements using standard WR-15 waveguide (50-75 GHz).

6.1 Introduction

The exponential growth in the commercial exploitation of the millimeter-wave frequency range [1–5] requires continual improvements in metrology. One important piece of measurement equipment is the vector network analyzer (VNA), which must be first calibrated before any device under test measurements can be performed. However, of equal importance, is the calibration verification process. In rectangular waveguide, the measurement setup (i.e. calibration and its verification) is a relatively slow manual process, when compared to rapid automated radio frequency on-wafer approaches [6]. Being a manual process, requiring multiple matings of rectangular waveguide flanges, mechanical misalignments can introduce errors in verification measurements [7], which become more pronounced as frequency increases into the millimeter-wave frequency range. Thus, the ability of these devices to act as independent, transferable, verification components will be significantly compromised at these higher frequencies due to interactions between multiple random misalignment errors, including those due to the inevitable imperfections in different end-users' test ports. Errors in verification measurements could lead to a false conclusion concerning the quality of the calibration, which in turn may lead to an unnecessary and time-consuming re-calibration.

In addition to calibration kits, millimeter-wave instrumentation manufacturers can also pro-

vide independent verification kits. However, in rectangular waveguide, verification kits are only commercially available for operation up to 110 GHz [8, 9]. A typical waveguide verification kit contains four distinct components: two fixed attenuators (e.g., 20 and 50 dB), a standard low loss thru section and a half-height impedance mismatch section. The thru and half-height sections can be accurately characterized by classical electromagnetic theory, while the fixed attenuators must be pre-characterized through traceable measurements. The quality of the verification components can be subsequently checked against the performance of the associated models, to ensure that the known electrical behaviour is maintained.

With conventional verification kits, components are permanently fixed, i.e. their electrical behaviour cannot be changed once they have been connected to the VNA. On the other hand, PIN diodes [10] and RF MEMS switches can be used for implementing an electronically reconfigurable verification kit. However, PIN diode circuits suffer from poor performance and are much more difficult to integrate at higher millimeter and sub-millimeter wave frequencies. RF MEMS switches can perform better, but still suffer from the problem of electromagnetic interactions with the biasing arrays and also introduce a large cost overhead.

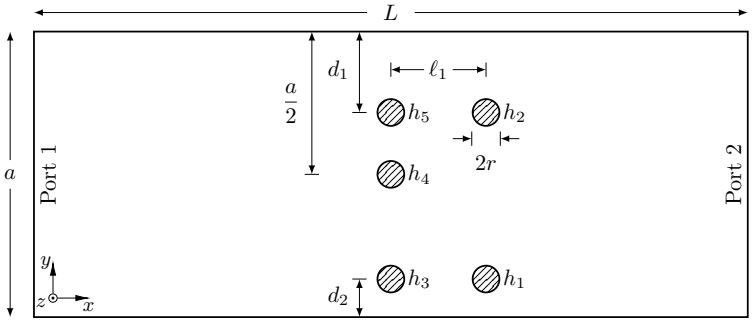
A single-component verification kit, consisting of a reconfigurable section of rectangular waveguide that can introduce a broad range of known values in the voltage-wave reflection and transmission coefficients, represents a novel simple approach.

One approach to creating a reconfigurable waveguide section is to pattern its broad walls with holes, so that metal pins can be inserted through the complete waveguide section. The process of inserting pins into an object, in order to cause a change to occur, is reminiscent of the mythological practices associated with voodoo. In the case of voodoo, pins are inserted into a "voodoo doll" in order to invoke a change in a person represented by the doll. In our case, pins are inserted into a section of waveguide in order to invoke a change in the electromagnetic characteristics of the waveguide. We therefore use the term "voodoo-waveguide" to describe this type of electromagnetic waveguide device. These pins will perturb the electromagnetic behaviour within the waveguide section, giving rise to known changes in reflection and transmission coefficients.

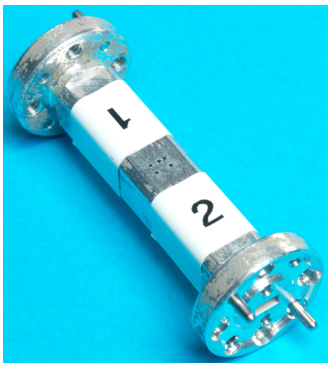
This chapter describes a reconfigurable "voodoo-waveguide" structure, realized in WR-15 waveguide (50-75 GHz). This millimeter-wave band was chosen because structures can be easily machined without the need for using more expensive micromachining technologies [11]. In addition, the voodoo-waveguide structure has been accurately characterized over the complete band. A proof-of-concept verification process is then described, based on the hardware implementation, full-wave numerical simulations and validation measurements. It has been demonstrated that this new approach to calibration verification can quickly reveal whether a calibrated VNA is operating within expected performance metrics.

6.2 Reconfigurable Voodoo-Waveguide Structure

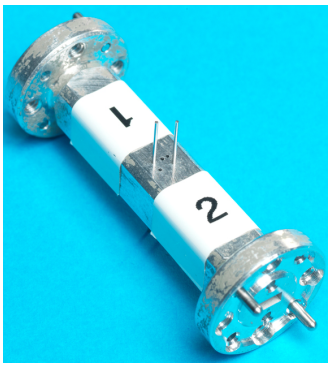
The design of the reconfigurable voodoo-waveguide structure is shown in Fig. 6.1, having five pins/holes to demonstrate the single-component verification concept. This device can easily be derived from the tunable waveguide circuits presented previously by covering most of the holes while leaving only a few blank at the desired locations. Details of the drilled pattern of holes, including their orientation with respect to the port identification numbers, are shown in Fig. 6.1(a). The holes are made by electrical discharge machining, using a computer-controlled process. A spark from a copper rod placed in close proximity to the aluminum waveguide surface repeatedly vaporizes a small part of the waveguide near the copper rod. The vertical line of holes h_3, h_4 and h_5, is nominally midway between the waveguide end ports. Fig. 6.1(b) and (c) show the finished air-filled metal-pipe rectangular waveguide, having internal aperture dimensions $a \times b = 3.76 \times 1.88$ mm^2



(a)



(b)



(c)

Figure 6.1: Reconfigurable voodoo-waveguide structure. (a) Design plan view. The shaded areas represent the position of the holes (nominal dimensions are $L = 50$ mm, $d_1 = 1$ mm, $d_2 = 0.5$ mm, $\ell_1 = 1.5$ mm and $r = 0.25$ mm). (b) Machined structure with no pins inserted and (c) machined structure with two pins inserted all the way through.

(corresponding to WR-15 [12]), with symmetrical holes drilled on both broad walls. Through the holes, high speed steel cylindrical pins can penetrate though the waveguide walls.

For example, with reference to Fig. 6.1(a), hole h_4 is placed at the center of the waveguide (along both the x- and y-directions), where the electric field is at a maximum for the fundamental TE^x_{10} mode, resulting in the highest level of interaction when a pin is inserted. Similarly, h_3 and h_5 are located in-line with h_4 (along the y-direction), with an offset d_2 and d_1 from the adjacent side walls, respectively. As a result, different levels of interference can be achieved to create known changes in the reflection and transmission coefficients. Additionally, holes h_1 and h_2 are in-line with h_3 and h_5 (along the x-direction), respectively, to provide phase offsets. With five holes there are 32 discrete combinations that can be selected, giving a wide range of verification measurements this is in contrast to the 4 possible states offered by commercial verification kits. For convenience, all pins have the same diameter of 500 µm, which needs to match the size of the holes, so that there is good electrical contact and no leakage of electromagnetic radiation.

For simplicity, the waveguide is only operated in its fundamental TE^x_{10} mode (with E_z, H_x, and H_y being non-zero), so that all higher-order modes are cut-off. With the pins placed vertically (i.e., parallel to the electric field E_z) currents are induced along the pins, resulting in a strong interaction with propagating fields. This would not be the case if the pins were placed horizontally. Simple single and double pin discontinuities have been studied analytically [13, 14].

As an example, the reflection and transmission characteristics of the reconfigurable voodoo-waveguide structure incorporating two pins, is shown in Fig. 6.2 for two different pin combinations. Polar plot responses exhibit a spiral frequency response (for both reflection and transmission

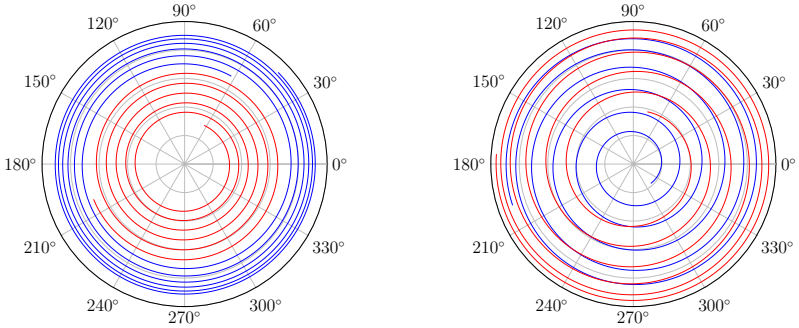


Figure 6.2: Reflection (blue curve) and transmission (red curve) characteristics for the reconfigurable voodoo-waveguide structure with pins filling the holes (a) h_1 and h_2, and (b) h_1 and h_5.

coefficients), which is unique to the reconfigurable voodoo structure. This single-component verification kit should be sufficient for most practical applications. Having values spread out across most of the S-parameter planes provides a comprehensive verification for the VNA's reflection and transmission measurements, as will be discussed in detail in the following sections.

6.3 Experimental Validation

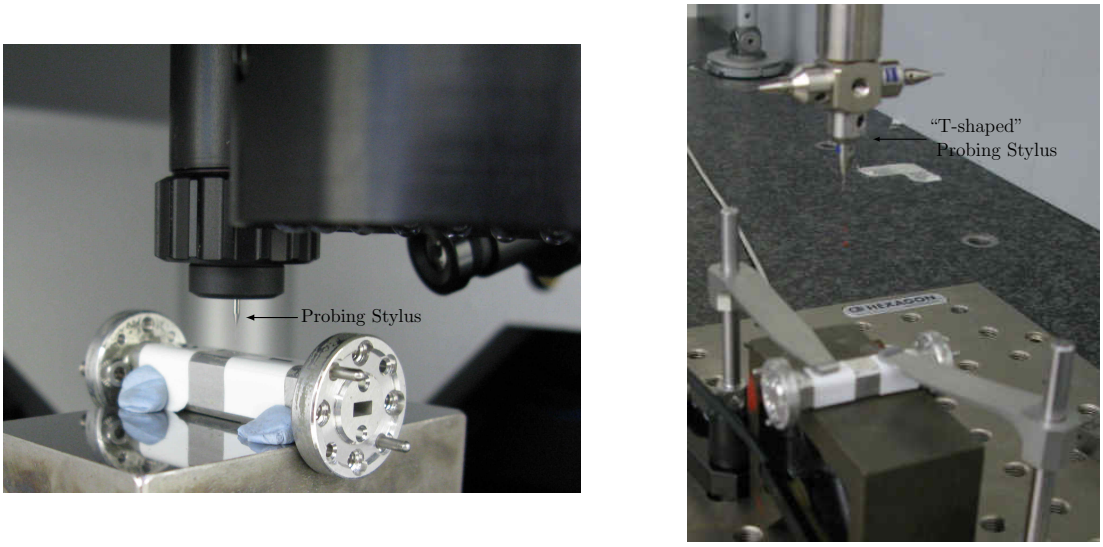
6.3.1 Dimensional Measurements

In order to accurately characterize the electrical behaviour of the reconfigurable voodoo-waveguide structure, at (sub)millimeter-wave frequencies, it is important to know the positions of the pin insertion holes at the micrometer level of accuracy.

The position of the pin insertion holes, with respect to waveguide datum features, was determined using a Coordinate Measuring Machine (CMM) at the UK's National Physical Laboratory. The intra-hole positions were determined using a Zeiss F25 smallcomponent CMM, fitted with a 125 µm diameter ball-ended probing stylus, as shown in Fig. 6.3(a).

The x-y surface of each hole was contacted at 16 different locations and a Gaussian best-fit circle fitted to the measurement data. A first local co-ordinate system (CS1) was set up using the center of h_4 as the origin, and the center location of the other four holes were established with respect to this evaluated feature. The position of h_4, with respect to the waveguide end faces (the port end planes) and outer side walls, was also determined. Because the pattern of holes is non-symmetric, the ports are labeled 1 and 2, to avoid any ambiguity in their identification. All measurements were repeated five times, as part of the process of determining the repeatability of the measurements.

The position of the waveguide's inner side walls, with respect to the outer side walls, was determined using a Zeiss Universal Precision Measuring Center (UPMC) CMM fitted with a "T-shaped" stylus array; each stylus having a 600 µm diameter ball-ended tip, as shown in Fig. 6.3(b). In this case, a second local co-ordinate system (CS2) was set up using designated waveguide datum features; this was then used as the global coordinate system. The Port 1 aperture was defined as the $x = 0$ plane, and one internal side wall defined as the $y = 0$ plane, as indicated in Fig.6.1(a), with the origin at $x = y = 0$. The latter is designated as the wall adjacent to holes h_1 and h_3. Because it was not possible to make contact with the inside of any side wall, along the length of the waveguide, 24 points corresponding to the inside of this side wall were determined at each end of the waveguide with Gaussian best-fit planes fitted to the data. A mean plane was constructed from



(a) **(b)**

Figure 6.3: Experimental setup for determining the hole positions.

Table 6.1: Hole locations (in mm) with respect to the origin of CS2.

	h_1	h_2	h_3	h_4	h_5	Port 2
x	26.428	26.449	24.940	24.955	24.940	49.979
y	0.465	2.713	0.459	1.835	2.713	—
$2r$	0.501	0.514	0.507	0.520	0.509	—

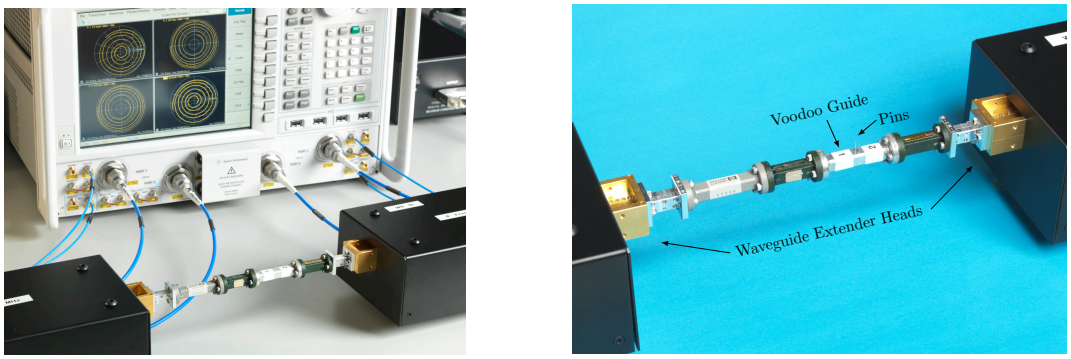
the part planes at both ends to define the $y = 0$ plane. The external position of the side wall, with respect to the $y = 0$ plane, was then determined. Finally, the center coordinates of all holes were transposed and evaluated in CS2. Again, measurements were repeated 5 times, to determine the repeatability of the measurements.

The coordinates of the hole-centers, with respect to coordinate system CS2, are given in Table 6.1, together with the location of the Port 1/Port 2 apertures (i.e., the overall length of the reconfigurable voodoo-waveguide structure). The measurement uncertainty of the data is estimated to be ± 0.25 µm, for the intra-hole positions, and ± 250 µm for the center co-ordinates of h_4. The larger uncertainty, in the latter case, is due primarily to the lower accuracy of the UPMC CMM. The holes were only measured from the top side of the waveguide, with the assumption that there is perfect symmetry between the top and bottom sides, such that the pins stand perfectly vertical.

6.3.2 Microwave Measurements Methodology

The electrical measurements were also made at the UK's National Physical Laboratory, using an Agilent Technologies PNA-X and a pair of Virginia Diodes Inc. waveguide extender heads. These extender heads are fitted with standard WR-15 waveguide test ports [12] and enable the VNA to make measurements across the full frequency range of interest (50-75 GHz), as shown in Fig. 6.4.

Traceable calibration standards were used for accurate S parameter measurements, with reference planes at the waveguide test ports; by performing a Thru-Reflect-Line (TRL) calibration [15]. This calibration employed WR-15 waveguide standards: Thru connection (T); a flush short-circuit connected, in turn, to each test port (R); and a quarter-wavelength delay line section of waveguide (L). The calibration was performed using an in-house calibration algorithm, employing a seven-term error-



(a) (b)

Figure 6.4: Experimental setup for measuring the frequency response of the reconfigurable voodoo-waveguide structure.

correction routine [16]. The overall set-up (i.e., VNA, primary standards and calibration algorithm) is referred to as the NPL Primary Impedance Microwave Measurement System (PIMMS) [17, 18]; this being the UK's primary national standard system for S-parameter measurements. The realization of this system for millimeter-wave waveguide measurements has been previously described [19].

PIMMS also determines the uncertainty in the S-parameter measurements. This is achieved following internationally agreed guidelines [20], with minor modifications to accommodate the complex-valued (i.e., vector) nature of the S-parameter measurands [21]. Uncertainties using PIMMS for measurements of the linear magnitude of transmission coefficients range typically from 0.001 to 0.002 [17] for a nominal transmission of 0.1 (i.e., 20 dB) in this waveguide band. Similarly, uncertainties for measurements of the linear magnitude of reflection coefficients range typically from 0.005 to 0.006 [17] for low reflecting devices in this waveguide band.

6.3.3 Microwave Measurements

The reflection and transmission coefficients of the reconfigurable voodoo-waveguide structure were first measured and compared with full-wave numerical simulations using the commercial software package CST Microwave Studio [22]. With our design, which has 32 different pin combinations, not all combinations had sufficiently distinct and useful characteristics and hence only some of the most illustrative combinations are shown in Figs. 6.5 to 6.8. The maximum observed difference between model and measurements is 4% for the reflection coefficient and 6% for the transmission coefficient, respectively.

As can be seen, the reconfigurable nature of the structure allows a diverse range of reflection and transmission values. The same behaviour is also observed as spirals in the measurement complex planes, as shown in Fig. 6.2. This diverse range has the advantage that most parts of the S-parameter complex planes can be verified and, hence, more detailed information about the quality of calibration can be obtained. This contrasts with the behaviour of most commercial verification kit components (i.e., attenuators and waveguide sections) that only provide relatively flat magnitude frequency responses (corresponding to circles in the measurement complex planes).

In order to verify the repeatability of the measured responses, four independent measurement sets were taken on two different days, with the VNA being re-calibrated before each measurement set. In assessing the performance of the proposed voodoo-waveguide structure, various metrics can be used. To some extent, the choice of metric would depend on the particular application and requirement of a given end-user. For example, we present here the average error between different

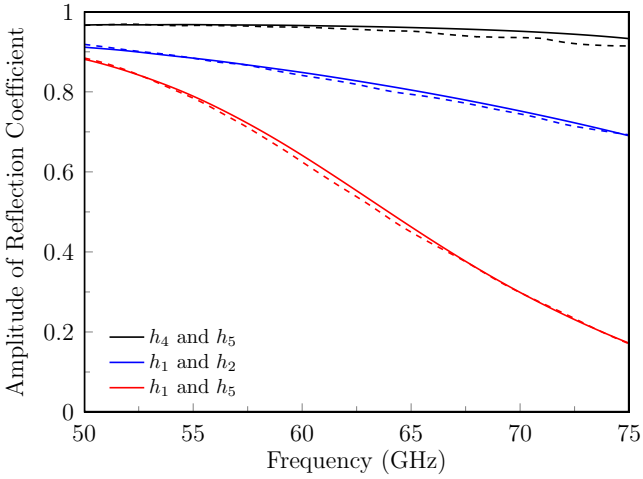


Figure 6.5: Amplitude of reflection coefficient for various pins configurations. Solid lines represent the simulated response and dashed lines the measured response.

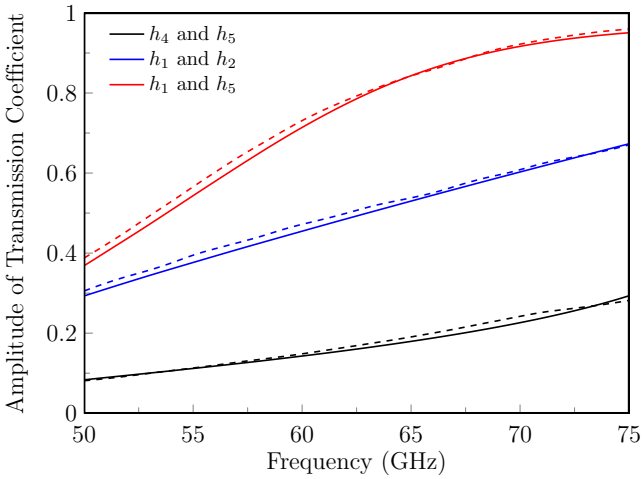


Figure 6.6: Amplitude of transmission coefficient for various pins configurations. Solid lines represent the simulated response and dashed lines the measured response.

sets S_{ij}^{e} which can be easily calculated using the Euclidean norm as

$$S_{ij}^{\mathrm{e}} = \frac{\left\| \mathbf{S}_{ij}^{n} - \mathbf{S}_{ij}^{k} \right\|_2}{\left\| \mathbf{S}_{ij}^{k} \right\|_2} \cdot 100\% \tag{6.1}$$

with $\mathbf{S}_{ij}^{n}$ and $\mathbf{S}_{ij}^{k}$ being two random measured sets for the S_{ij} parameter matrix, with data sets $n \neq k \in \{1, ..., 4\}$, resulting in S_{ij}^{e} of about 1.5%. This suggests that the measurements are very repeatable and relatively insensitive to small variations in both the general waveguide experimental setup (i.e., due to flange misalignments) and component tolerances (i.e., pin misalignments). The small discrepancies for this low millimeter-wave frequency band can be attributed primarily to these misalignments and also random sources of error (e.g., VNA system noise).

Similarly, the measured results are compared with the simulation results, using the Euclidean

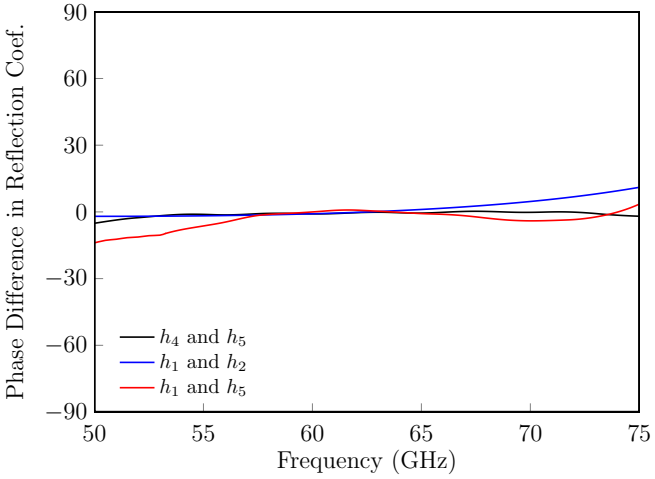


Figure 6.7: Phase difference between numerical simulations and measurements of reflection coefficient for various pin configurations.

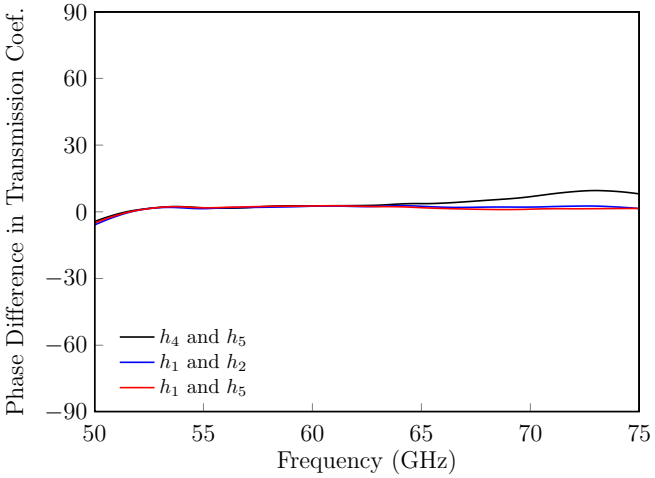


Figure 6.8: Phase difference between numerical simulations and measurements of transmission coefficient for various pin configurations.

norm, and an average error S_{ij}^{e} is obtained from

$$S_{ij}^{\mathrm{e}} = \frac{\left\| \mathbf{S}_{ij}^{\mathrm{s}} - \mathbf{S}_{ij}^{\mathrm{m}} \right\|_2}{\left\| \mathbf{S}_{ij}^{\mathrm{m}} \right\|_2} \cdot 100\% \tag{6.2}$$

where $\mathbf{S}_{ij}^{\mathrm{s}}$ and $\mathbf{S}_{ij}^{\mathrm{m}}$ are the simulated and measured S_{ij}-parameter matrices, respectively. Here, the simulation results act as references, since they are free from flange/pin misalignment errors that may affect the measurements. For example, the average error across frequency in the reflection coefficient for the three configurations shown in Figs. 6.5 and 6.7 is less than approximately 2% (this error increases with decreasing reflection). On the other hand, the average error across frequency in the transmission coefficient shown in Figs. 6.6 and 6.8 is less than approximately 5% (this error decreases with increasing transmission). The higher percentage errors for both reflection and transmission are only due to the small absolute errors that become more significant when measuring small values. Indeed, it is interesting to note that the largest errors are for the lowest curves in Figs. 6.5 and 6.6, which correspond to small absolute values. Thus, this does not change the fact that good agreement is observed between simulation and measured results.

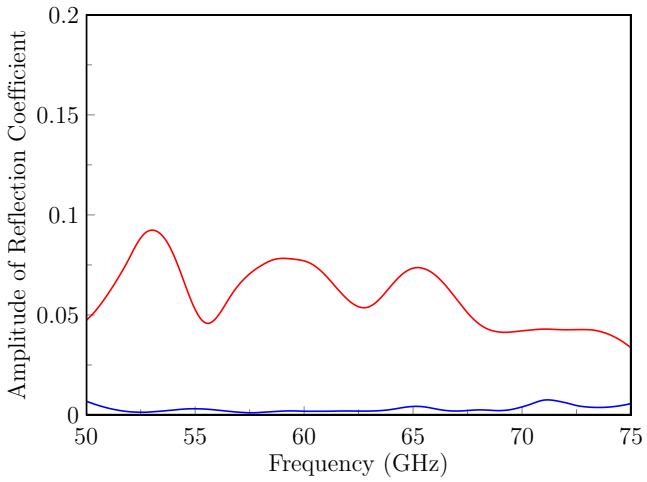


Figure 6.9: Measured responses for a well-matched load standard (blue curve) and a poorly-matched load standard (red curve).

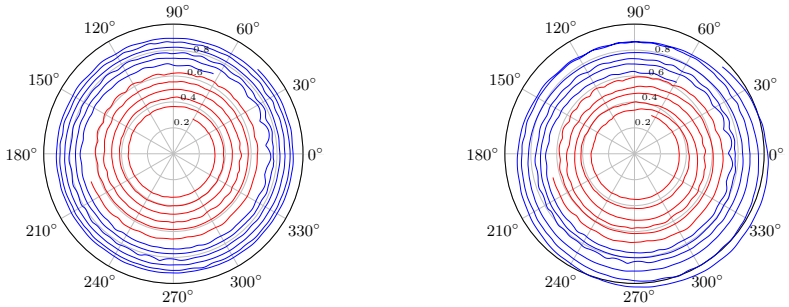
Table 6.2: Average error in reflection and transmission coefficients for good/poor calibration.

	Reflection Coefficient			**Transmission Coefficient**		
	h_1 and h_2	h_1 and h_5	h_4 and h_5	h_1 and h_2	h_1 and h_5	h_4 and h_5
Good Cal.	1.2%	2.1%	2.1%	1.7%	1%	4.5%
Poor Cal.	4.9%	10%	5.4%	5.9%	7.6%	7.6%

6.3.4 Calibration Verification Proof-of-Concept

Having characterized the proposed reconfigurable voodoo-waveguide structure, it is now possible to demonstrate its value as a single-component verification kit. With TRL calibration and the use of PIMMS, it is difficult to deliberately adjust the quality of a given calibration. Therefore, the widely used Short/Offset-short/Load/Thru (SOLT) calibration method was used to enable a deliberately poor calibration to be introduced into the investigation. With waveguides the SOLT calibration is performed using three known loads. Usually, a high quality well-matched load standard can produce a linear reflection coefficient magnitude of less than 0.01 (corresponding to a return loss of 40 dB), at millimeter-wave frequencies, as shown in Fig. 6.9.

After performing a good calibration, using a well-matched load standard, the reconfigurable voodoo-waveguide structure was connected to the VNA test ports, resulting in polar plots for both the reflection and transmission measurements shown in Fig. 6.10(a). Next, a deliberately poor calibration was performed using a load standard having a significant impedance mismatch (i.e., with a linear reflection coefficient of between 0.05 and 0.1, as shown in Fig. 6.9, corresponding to a worst-case return loss of 20 dB), to produce a calibration that is unacceptable for most practical applications. This is a typical scenario when a standard may have been poorly treated during its working life time, and its level of performance degradation may not be obvious to the user. The single-component voodoo-waveguide verification kit is then re-connected and its reflection and transmission measurements plotted in Fig. 6.10(b). A visual inspection of the polar plots in Fig. 6.10(a) and 6.10(b) clearly shows abnormal behaviour (e.g., the magnitude of the reflection coefficient exceeding unity), consistent with a poor calibration. This clearly indicates that the calibration being verified is of unacceptable quality. Furthermore, the quality of the calibration can also be studied quantitatively (e.g., by calculating the average error between simulations and measurements)



(a) (b)

Figure 6.10: Reflection (blue curve) and transmission (red) characteristics when (a) a good SOLT calibration is performed and (b) when a poor SOLT calibration is performed (i.e., using an "ill-conditioned" matched load). The plots correspond to the case where h_1 and h_2 are filled with pins.

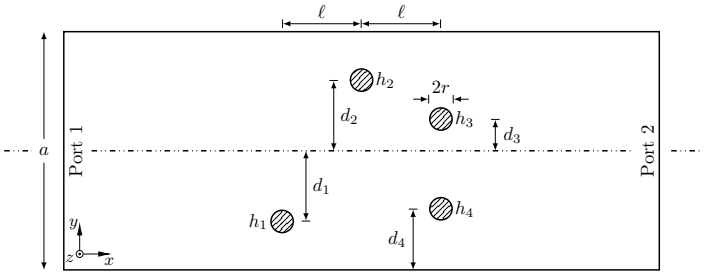


Figure 6.11: Illustration of the proposed WR-10 verification device. The shaded areas represent the position of the holes. The nominal dimensions are: $d_1 = d_2 = 750$ µm, $d_3 = 250$ µm, $d_4 = 650$ µm, $\ell = 750$ µm, $2r = 500$ µm

across frequency, as shown in Table 6.2. The percentage error for different pin configurations clearly reveals the calibration quality, thus successfully demonstrating the proof-of-concept for this single-component verification kit.

6.4 WR-10 Waveguide Design

The previous analysis can be easily applied to realize single-component verification kits at higher frequencies. For example, WR-10 waveguide verification device design is shown in Fig. 6.11. Here, the pins radius is kept the constant and equal to $r = 0.25$ mm, as in the WR-15 verification component. This emphasizes the fact that there are many degrees of freedom in the design and that the holes/pins do not have to be necessarily scaled for neighboring frequency bands. The modeled frequency responses are shown in Fig. 6.12 for various pin configurations, where the diverse range of values in the transmission and reflection coefficients are obvious. This has been done due to limitations in the manufacturing technique used

6.5 Discussion and Conclusion

A novel simple approach in the verification process for vector network analyzer waveguide calibration has been reported, using a single-component verification kit. The strength of the proposed reconfigurable voodoo-waveguide structure is that it can easily be transformed from having a very

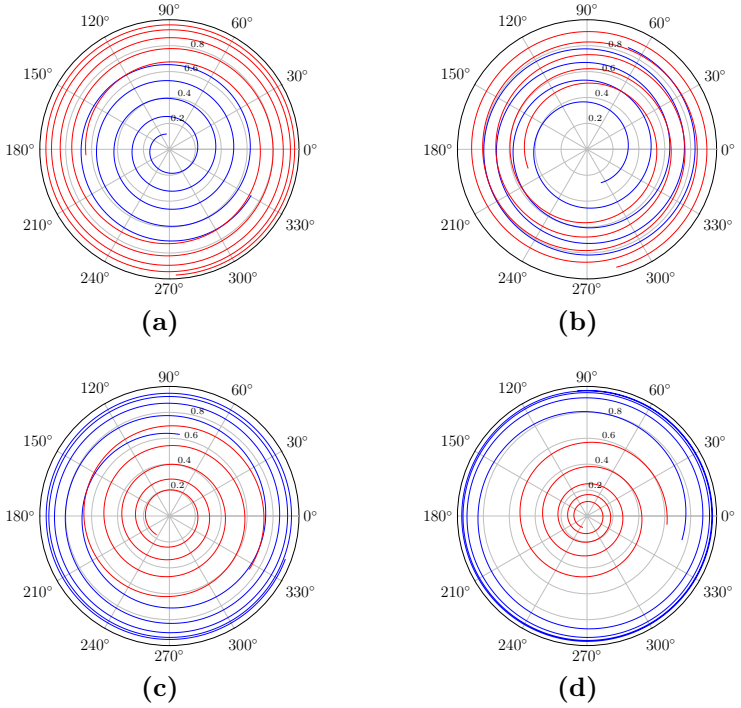


Figure 6.12: Reflection (blue curve) and transmission (red curve) response in the WR-10 waveguide band (75 to 110 GHz) when (a) h_2, (b) h_4 (c) h_1 and h_2 and (d) h_2 and h_3 are filled with pins.

good impedance match (when all pins are removed) to varying degrees of mismatch (by inserting different combinations of pins). Furthermore, the different pin combinations also provide varying degrees of attenuation (i.e., higher levels of attenuation are achieved when more pins are introduced). Therefore, there is a wide dynamic range of operation in both the reflection and transmission coefficient domains. It must be emphasized that the primary goal of this work is to provide an alternative method for VNA verification at high millimeter-wave frequencies rather than a calibration method.

Conventional multi-component commercial waveguide verification kits are currently only available at frequencies up to 110 GHz. If such kits are made available at higher frequencies then the necessary multiple flange connections will make them susceptible to measurement errors due to the inevitable mechanical misalignments of the waveguide interfaces. In contrast, a single-component verification kit will inherently exhibit smaller errors at higher frequencies, while its reconfigurability offers a broader selection of known electrical characteristics. Moreover, the time taken to reconfigure the compact verification kit is significantly reduced.

For millimeter-wave metrology, where mechanical precision is of paramount importance, this single-component verification approach represents an attractive solution. For example, the rectangular waveguide verification kit could be implemented using radio frequency microelectromechanical systems technology [11], possibly using paraffin wax microactuator technology [23, 24].

A proof-of-concept verification process has been described, based on hardware implementation, simulations and validation measurements using standard WR-15 waveguide (50-75 GHz). While a relatively low millimeter-wave band has been used here, for convenience, this approach is inherently suited for VNAs operating at millimeter- and submillimeter-wave frequencies, where flange misalignment errors can dominate. This will open up new opportunities for verifying the latest generation of VNAs that operate in waveguide at millimeter- and submillimeter-wave frequencies (to 1.1 THz).

References

[1] J. D. Albrecht, M. J. Rosker, H. B. Wallace and T. H. Chang, "THz Electronics Projects at DARPA: Transistors, TMICs and Amplifiers", *Proc. IEEE Int. Microw. Symp.*, pp. 1118-1121, May 2010

[2] R. Appleby and R. N. Anderton, "Millimeter-Wave and Submillimeter-Wave Imaging for Security and Surveillance", *Proc. IEEE*, vol. 95, no. 8, pp. 1683-1690, Aug. 2007

[3] B. Thomas, B. Alderman, D. Matheson and P. de Maagt, "A Combined 380 GHz Mixer/Doubler Circuit Based on Planar Schottky Diodes", *IEEE Microw. Wireless Compon. Lett.*, vol. 18, no. 5, pp. 353-355, May 2008

[4] L. Samoska, W. R. Deal, G. Chattopadhyay, D. Pukala, A. Fung, T. Gaier, M. Soria, V. Radisic, X. Mei and R. Lai, "A Submillimeter-Wave HEMT Amplifier Module with Integrated Waveguide Transitions Operating Above 300 GHz", *IEEE Trans. Microw. Theory Techn.*, vo. 56, no. 6, pp. 1380-1388, Jun. 2008

[5] Oleson Microwave Labs (OML), "Frequency Extension Source Modules to Extend Signal Capability from 50 to 325 GHz", *Microw. J.*, vol. 47, no. 3, pp. 124-134, Mar. 2004

[6] S. Lucyszyn, "RFIC and MMIC measurement techniques", *Chapter 11, pp. 217-262, "Microwave Measurements"*, 3rd ed., R. Collier and D. Skinner (Editors), IET, London, Oct. 2007

[7] D. Williams, "500 GHz750 GHz Rectangular-Waveguide Vector-Network-Analyzer Calibrations", *IEEE Trans. Terahertz Sci. Technol.*, vol. 1, no. 2, pp. 364 - 376, Nov. 2011

[8] Maury Microwave, "Two-port Standard Sets", Technical Data Sheet 3A-322A, Apr. 1998. (Available online: http://maurymw.com/pdf/datasheets/3A-322A.pdf)

[9] Agilent Technologies, "11645A R, Q, U, V, W Waveguide Verification Kits User's and Service Guide", Part Number 11645-90013, Nov. 2004

[10] M. Fallahpour, M. A. Baumgartner, A. Kothari, M. T. Ghasr, D. Pommerenke, R. Zoughi, "Compact Ka-Band One-Port Vector Reflectometer Using a Wideband Electronically Controlled Phase Shifter"', *IEEE Trans. Instrum. Meas.*, vol. 61, no. 10, pp. 2807-2816, Oct. 2012

[11] S. Lucyszyn, "Advanced RF MEMS", *Cambridge University Press*, Cambridge, Aug. 2010

[12] MIL-DTL-85/3C, "Waveguides, rigid, rectangular (millimetre wavelength)", Oct. 2005

[13] R. Gesche and N. Loechel, "Scattering by a lossy dielectric cylinder in a rectangular waveguide", *IEEE Trans. Microw. Theory Techn.*, vol. 36, no. 1, pp. 137-144, Jan. 1988

[14] R. Gesche and N. Loechel, "Two cylindrical obstacles in a rectangular waveguideresonances and filter applications", *IEEE Trans. Microw. Theory Techn.*, vol. 37, no. 6, pp. 962-968, Jun. 1989

[15] G. F. Engen and C. A. Hoer, "Thru-Reflect-Line: An improved technique for calibrating the dual six-port automatic network analyser", *IEEE Trans. Microw. Theory Techn.*, vol. 27, no. 12, pp. 987-993, Dec. 1979

[16] A. Rumiantsev and N. M. Ridler, "VNA calibration", *IEEE Microw. Mag.*, vol. 9, no. 3, pp. 86-99, Jun. 2008

[17] N. M. Ridler, "A review of existing national measurement standards for RF and microwave impedance parameters in the UK", *IEE Colloquium Digest*, .no 99/008, pp. 6/1-6/6, Feb. 1999

[18] N. M. Ridler, "News in RF impedance measurement", *XXVIIth General Assembly of the International Union of Radio Science (URSI)*, The Netherlands, Aug. 2002

[19] G. J. French and N. M. Ridler, "A primary national standard for millimetric waveguide S-parameter measurements", *Microwave Engineering Europe*, pp. 29-32, Oct. 1999

[20] ISO/IEC Guide 98-3:2008, "Uncertainty of Measurement – Part 3: Guide to the expression of the Uncertainty in Measurement (GUM:1995)", *International Organization for Standardization*

[21] N. M. Ridler and M. J. Salter, "An approach to the treatment of uncertainty in complex S-parameter measurements", *Metrologia*, vol. 39, no. 3, pp. 295-302, Jun. 2002

[22] www.cst.com/

[23] J. S. Lee and S. Lucyszyn, "A micromachined refreshable Braille cell", *J. Microelectromech. Syst.*, vol. 14, no. 4, pp. 673-682, Aug. 2005

[24] J.-Y. Choi, J. Ruan, F. Coccetti and S. Lucyszyn, "Three-dimensional RF MEMS switch for power applications"', *IEEE Trans. Ind. Electron.*, vol. 56, no. 4, pp. 1031-1039, Apr. 2009

Chapter 7

Lossy Spherical Cavity Resonators for Stress-testing Eigenmode Solvers

In order to model coupling between lossy elements in metamaterial structures, it is essential to have accurate models describing the resonant behaviour of simple structures that collectively may form such metamaterials. Moreover, it is essential that numerical simulation tools provide accurate results for arbitrary structures. This is important since full-wave solvers are often the only approach to verifying the behaviour of metamaterials. For this reason, the simplest structure is studied with a view to stress-testing commercial eigenmode solvers. In this chapter, the electromagnetic analysis of lossy metal-walled spherical cavity resonators is given from first principles,. Exact analytical results, acting as a benchmark reference standard, are compared to those generated independently by two commercial, industry-standard, full-wave numerical simulation modeling software packages (HFSS™ and COMSOL); both employing the finite-element method. Unlike perturbation techniques, appropriate only for low loss scenarios (i.e. walls having high intrinsic conductivities), there are no inherent loss limitations in our analysis. When the wall transforms from being a perfect electrical conductor (PEC) to free space, as its intrinsic conductivity decreases from infinity to zero, it is found that the eigenmode solvers with both software packages increasingly fail; this has profound implications on their usefulness for the modeling of arbitrary 3D lossy structures having even the simplest of geometries. With both software packages, all possible modeling strategies have been investigated and their associated limitations identified. Moreover, a plane-wave approximation model is proposed that accurately predicts the numerical simulation results for the finite conductivity boundary and layered impedance boundary conditions; this provides an analytical means for accurately quantifying the weakness of the numerical eigenmode solvers. It is also found that, when using the accurate impedance boundary condition, a priori knowledge of the resonance frequency and the wave impedance at the boundary is required, otherwise it will result in a total failure to predict the eigenfrequencies for arbitrary 3D structures having lossy metal walls. For completeness, a generic lumped-element *RLC* equivalent circuit model is given that exactly describes the cavity behavior as its wall transforms from being a PEC to free space. In addition, the long-standing ambiguity associated with defining unloaded quality factors with lossy resonators is resolved. Together, a deeper insight into the behavior of lossy spherical cavity resonators and commercial eigenmode solvers is given for the first time.

7.1 Introduction

Electromagnetic cavity resonators having electrically conducting walls have been exploited for well over seven decades [1–3], because of their ability to produce sharp spectral resonances – much

sharper than their lumped-element counterparts. Their ability to store electromagnetic energy with very low dissipative losses, from sub-microwave [4] to optical [5] frequencies, has made them an essential component in many systems.

In general, it is highly desirable to have low-loss electromagnetic resonators (e.g., to implement high-performance impedance matching networks and filters). However, there are many examples where lossy resonant structures exist; requiring a more rigorous approach to the modeling of their behavior. Examples include: (1) surface plasmon polaritons, found in nature and engineered [6]; (2) heavy time-domain damping of unwanted resonances (e.g., in DC biasing networks) and even control systems; (3) implementation of ultra wideband frequency-domain networks (e.g. antennas, phase shifters and filter found in ultra-high speed telecommunications and radar systems); (4) unexpected box-mode resonances with low-cost plastic/organic packaging of high frequency devices; and (5) certain metamaterial structures.

Clearly, there is an inherent need for the accurate numerical simulation of arbitrary 3D structures, regardless of the levels of associated material losses. An illustrative example is that of metamaterials of infinite extent an area that has received great interest in recent years where full-wave numerical simulations often provide the only realistic option to study their behavior (e.g., [7]).

While structures with "good electrical conductors" can be easily modeled with excellent accuracy, this is not straightforward when low conductivity materials are modeled, as will be shown later. To this end, the stress-testing of commercial electromagnetic full-wave simulation software packages is of critical importance to both the academic community and industry; as previously undertaken for the modeling of electrically-thin metal-walled structures [8] and those intended for use at terahertz frequencies [9]. To this end, a traceable benchmark structure (mathematically defined by an exact analytical model) is required, to compare its results with those from numerical simulations, with a view to quantifying levels of accuracy. With numerical electromagnetic field solvers intended for arbitrary 3D structures, the spherical cavity resonator represents an ideal benchmark structure. This is because, unlike lossy metal-walled rectangular cavity resonators, it does not suffer from the effects of diffraction; thus, able to provide an exact analytical solution for arbitrary levels of loss.

Low loss performance with metal-walled cavities is achieved with the use of "good electrical conductors". Fortunately, in this case, the analysis can be greatly simplified with the use of approximate solutions (e.g., perturbation techniques); this is well documented in many works (e.g., Slater [10]), but their validity is limited to low losses. A more general approach for the modeling of metal-walled cavities was reported by Hadidi and Hamid, for cylindrical resonators with lossy end walls, although their work still requires the use of approximations [11]. However, the exact analytical formulation for the generic case of a dielectric sphere inside another dielectric of infinite thickness was given by Gastine *et al.* [12]. This exact analytical model was then only used to investigate the modal behavior of ideal lossless homogeneous dielectric spheres in free space. After an exhaustive literature survey, the modeling of lossy metal-walled spherical cavity resonators could not be found. For this reason, the general modeling of low quality factor metal-walled spherical cavity resonators is studied, for the first time, with a view to gaining new insight into their behaviour and to perform stress-testing of commercial arbitrary 3D eigenmode solvers (by the introduction of arbitrary lossy metal walls).

7.2 Analytical Formulation

The electromagnetic fields within a spherical cavity are first expanded into normal waveguide modes. As is well known, the fields within the cavity can be decomposed into two families; namely transverse electric (TE) and transverse magnetic (TM). In our case, radially propagating waves with both families are of interest and, hence, so are the associated modes that are transverse with

respect to the radial direction. In the general case of an inhomogeneous dielectric-filled cavity (along the radial direction) the modes are neither pure TE nor pure TM, but a superposition of both. One way to obtain the field distributions for each family is with the use of the Hertz vector potentials. A thorough study of this method is beyond the scope of this work and can be found in classical electromagnetics textbooks [13, 14]; only a brief outline is given here, for completeness. The steady-state time-harmonic fields inside the cavity volume can be written (using a temporal dependence of $e^{j\omega t}$) as

$$\mathbf{E} = \mathbf{E}_{\mathrm{TE}} + \mathbf{E}_{\mathrm{TM}} = -j\omega\mu_{\mathrm{d}}\nabla\times\mathbf{\Pi}_{\mathrm{h}} + \nabla\times\nabla\times\mathbf{\Pi}_{\mathrm{e}} \tag{7.1}$$

$$\mathbf{H} = \mathbf{H}_{\mathrm{TE}} + \mathbf{H}_{\mathrm{TM}} = \nabla\times\nabla\times\mathbf{\Pi}_{\mathrm{h}} + j\omega\varepsilon_{\mathrm{d}}\nabla\times\mathbf{\Pi}_{\mathrm{e}} \tag{7.2}$$

where $\mathbf{\Pi}_{\mathrm{e}}$ and $\mathbf{\Pi}_{\mathrm{h}}$ are the electric-type and magnetic-type Hertz vector potentials, respectively, having the form of $\mathbf{\Pi}_{\mathrm{e,h}} = \psi\mathbf{u}_r$, with with ψ being a scalar function and $\mathbf{u}_r$ the unit normal vector along the radial r-direction. The expression for ψ can be obtained by solving the scalar Helmholtz equation $(\nabla^2 + k_{\mathrm{d}}^2)\psi/r = 0$ in spherical coordinates as

$$\psi = \frac{A}{j\omega\mu_{\mathrm{d}}\varepsilon_{\mathrm{d}}} k_{\mathrm{d}} r j_n(k_{\mathrm{d}}r) P_n^m(\cos\theta)\Big[B\cos(m\phi) + C\sin(m\phi)\Big] \tag{7.3}$$

within the cavity filler, μ_{d} and ε_{d} are the intrinsic permeability and permittivity, respectively, the wavenumber $k_{\mathrm{d}} = \omega\sqrt{\mu_{\mathrm{d}}\varepsilon_{\mathrm{d}}}$, ω is the angular frequency, r is the radial coordinate and A, B, C are mode-dependent normalization constants. The rest of the symbols have their usual meaning, with j_n being the spherical Bessel functions of the first kind, $P_n(\cos\theta)$ the Legendre polynomials and m, n corresponding to the variations along the azimuthal angle ϕ and polar angle θ, respectively.

The TE modes can be obtained from a magnetic-type Hertzian potential directed along the radial direction (i.e., $\mathbf{\Pi}_{\mathrm{e}} = 0$). In this case the field distributions are given by

$$\mathbf{E}_{\mathrm{TE}} = j\omega\mu_{\mathrm{d}}\left[0,\ -\frac{1}{r\sin\theta}\frac{\partial\psi}{\partial\phi}\mathbf{u}_\theta,\ \frac{1}{r}\frac{\partial\psi}{\partial\theta}\mathbf{u}_\phi\right] \tag{7.4}$$

$$\mathbf{H}_{\mathrm{TE}} = \left[\left(\frac{\partial^2}{\partial r^2} + k_{\mathrm{d}}^2\right)j\omega\mu_{\mathrm{d}}\varepsilon_{\mathrm{d}}\psi\mathbf{u}_r,\ \frac{1}{r}\frac{\partial^2\psi}{\partial r\partial\theta}\mathbf{u}_\theta,\ \frac{1}{r\sin\theta}\frac{\partial^2\psi}{\partial r\partial\phi}\mathbf{u}_\phi\right] \tag{7.5}$$

Similarly, the fields for the TM modes are obtained from an electric-type Hertzian potential directed along the radial direction (i.e., $\mathbf{\Pi}_{\mathrm{h}} = 0$). Thus, the electromagnetic fields can be written as

$$\mathbf{H}_{\mathrm{TM}} = j\omega\varepsilon_{\mathrm{d}}\left[0,\ \frac{1}{r\sin\theta}\frac{\partial\psi}{\partial\phi}\mathbf{u}_\theta,\ -\frac{1}{r}\frac{\partial\psi}{\partial\theta}\mathbf{u}_\phi\right] \tag{7.6}$$

$$\mathbf{E}_{\mathrm{TM}} = \left[\left(\frac{\partial^2}{\partial r^2} + k_{\mathrm{d}}^2\right)j\omega\mu_{\mathrm{d}}\varepsilon_{\mathrm{d}}\psi\mathbf{u}_r,\ \frac{1}{r}\frac{\partial^2\psi}{\partial r\partial\theta}\mathbf{u}_\theta,\ \frac{1}{r\sin\theta}\frac{\partial^2\psi}{\partial r\partial\phi}\mathbf{u}_\phi\right] \tag{7.7}$$

For TE modes with $n, p \neq 0$:

$$\mathbf{E}_{\parallel,\mathrm{TE}} = \frac{A}{\varepsilon_{\mathrm{d}}}k_{\mathrm{d}}j_n(k_{\mathrm{d}}r)\begin{bmatrix}\dfrac{mP_n^m(\cos\theta)}{\sin\theta}\Big(B\sin(m\phi) - C\cos(m\phi)\Big)\mathbf{u}_\theta \\ \dfrac{dP_n^m(\cos\theta)}{d\theta}\Big(B\cos(m\phi) + C\sin(m\phi)\Big)\mathbf{u}_\phi\end{bmatrix} \tag{7.8}$$

$$\mathbf{H}_{\parallel,\mathrm{TE}} = \frac{Ak_{\mathrm{d}}}{j\omega\mu_{\mathrm{d}}\varepsilon_{\mathrm{d}}r}\frac{d}{dr}\Big[j_n(k_{\mathrm{d}}r)\Big]\begin{bmatrix}\dfrac{dP_n^m(\cos\theta)}{d\theta}\Big(B\cos(m\phi) + C\sin(m\phi)\Big)\mathbf{u}_\theta \\ \dfrac{m}{\sin\theta}\dfrac{dP_n^m(\cos\theta)}{d\theta}\Big(-B\sin(m\phi) + C\cos(m\phi)\Big)\mathbf{u}_\phi\end{bmatrix} \tag{7.9}$$

For TM modes with $n, p \neq 0$:

$$\mathbf{H}_{\parallel,\mathrm{TM}} = -\frac{A}{\mu_\mathrm{d}} k_\mathrm{d} j_n(k_\mathrm{d} r) \begin{bmatrix} \dfrac{m P_n^m(\cos\theta)}{\sin\theta}\Big(B\sin(m\phi) - C\cos(m\phi)\Big)\mathbf{u}_\theta \\ \dfrac{dP_n^m(\cos\theta)}{d\theta}\Big(B\cos(m\phi) + C\sin(m\phi)\Big)\mathbf{u}_\phi \end{bmatrix} \tag{7.10}$$

$$\mathbf{E}_{\parallel,\mathrm{TM}} = \frac{Ak_\mathrm{d}}{j\omega\mu_\mathrm{d}\varepsilon_\mathrm{d} r}\frac{d}{dr}\Big[j_n(k_\mathrm{d} r)\Big] \begin{bmatrix} \dfrac{dP_n^m(\cos\theta)}{d\theta}\Big(B\cos(m\phi) + C\sin(m\phi)\Big)\mathbf{u}_\theta \\ \dfrac{m}{\sin\theta}\dfrac{dP_n^m(\cos\theta)}{d\theta}\Big(-B\sin(m\phi) + C\cos(m\phi)\Big)\mathbf{u}_\phi \end{bmatrix} \tag{7.11}$$

It is straightforward to write the field components that are parallel to the surface of the wall, as in (7.8)-(7.11). Similarly, the fields in the surrounding wall medium are given by replacing the spherical Bessel function with the spherical Hankel function of the second kind [12]. The transverse wave impedance Z_w is defined as

$$Z_\mathrm{w} = \frac{E_\theta}{H_\phi} \tag{7.12}$$

In order to obtain an unambiguous solution, the field components must satisfy the appropriate boundary conditions at the surface of the cavity wall (i.e., the tangential fields must be continuous at the wall surface); the transverse wave impedance must also be continuous across the wall interface. After some algebraic manipulations and using the relationship $f_n'(x) = f_{n-1}(x) - \dfrac{n+1}{x} f_n(x)$, where $f_n(x)$ is either the spherical Bessel function or Hankel function and the prime represents differentiation with respect to the argument, the following transcendental equation is obtained for the $\mathrm{TM}_{\mathrm{mnp}}$ modes (which can be solved numerically following a similar approach as described in Chapter 3.).

$$\eta_\mathrm{d}\left[\frac{j_{n-1}(k_\mathrm{d}R_a)}{j_n(k_\mathrm{d}R_a)} - \frac{n}{k_\mathrm{d}R_a}\right] - \eta_\mathrm{c}\left[\frac{h_{n-1}^{(2)}(k_\mathrm{c}R_a)}{h_n^{(2)}(k_\mathrm{c}R_a)} - \frac{n}{k_\mathrm{c}R_a}\right] = 0 \tag{7.13}$$

where $j_n(x)$ and $h_n^{(2)}(x)$ are the n^{th}-order spherical Bessel function of the first kind and Hankel function of the second kind, respectively. Also, R_a is the radius of the cavity, $\eta_\mathrm{d} = \sqrt{\mu_\mathrm{d}/\varepsilon_\mathrm{d}}$ and $\eta_\mathrm{c} = \sqrt{\mu_\mathrm{c}/\varepsilon_\mathrm{c}}$ are the intrinsic impedances of the spherical cavity's internal dielectric filler and infinitely thick conducting wall materials, respectively, $k_\mathrm{d} = \omega_0\sqrt{\mu_\mathrm{d}\varepsilon_\mathrm{d}}$, $k_\mathrm{c} = \omega_0\sqrt{\mu_\mathrm{c}\varepsilon_\mathrm{c}}$ and $\omega_0 = \omega_0' + j\omega_0''$ is the complex angular resonance frequency (or eigenfrequency). Also for the conducting wall material, μ_c and $\varepsilon_\mathrm{c} = \varepsilon_0\left(\varepsilon_{\mathrm{r}\infty} - j\,\dfrac{\sigma_\mathrm{c}}{\omega_0\varepsilon_0}\right)$ are the effective permeability and effective permittivity, respectively, where ε_0 is the permittivity of free space and σ_c is the intrinsic conductivity. In this work, for convenience, we set $\mu_\mathrm{c} = \mu_0$ (permeability of free space), $\varepsilon_{\mathrm{r}\infty} = 1$ and $\sigma_\mathrm{c} = \sigma_0$ (bulk DC conductivity). This classical skin-effect approach for non-magnetic materials gives accurate results for the frequencies of interest (i.e. below *ca.* 1 THz). However, other material frequency dispersion models can also be easily employed [9, 15].

For simplicity, and without any loss of generality, we focus our analysis on a dielectric-filled spherical cavity, where the two mode families are decoupled; operating in the dominant TM_{011} mode (i.e., $m = 0$, $n = p = 1$, where p is associated with the variations along the radial direction), although any other mode could also be studied. Moreover, we restrict our interest to mono-mode operation, in order to clearly illustrate physical behavior, i.e. without introducing additional complications from multi-mode effects. With the TM_{011} mode, the only non-zero components are E_r, E_θ and H_ϕ.

Now, (7.13) can be solved numerically for ω_0. In general, the eigenfrequencies are complex-valued because of the presence of losses associated with the wall material. In the special case where the walls are lossless (i.e., perfect electrical conductors with $\eta_\mathrm{c} = 0$, then (7.13) reduces to the standard

textbook expression

$$j_1(k_{\mathrm{I}}R_a) + j_1'(k_I R_a)kR_a = 0 \tag{7.14}$$

with the lowest resonant frequency given by $k_I R_a = 2.74370$ or equivalently by $\omega_{\mathrm{I}} = \dfrac{2.74370}{R_a\sqrt{\mu_{\mathrm{d}}\varepsilon_{\mathrm{d}}}}$, where ω_{I} is the ideal angular resonance frequency.

By introducing a non-zero surface reactance, the undamped (or driven) angular resonance frequency $|\omega_0|$ (normally associated with the steady-state frequency domain) is reduced from its ω_{I} value. Moreover, the further introduction of a non-zero surface resistance results in further frequency detuning; in general, shifting the actual angular resonance frequency down from $|\omega_0|$ to the damped (or undriven) angular resonance frequency ω_0'[9] (normally associated with the transient time domain).

Once the complex eigenfrequency is obtained from (7.13), the unloaded quality factor of the resonator can be calculated from the standard definition

$$Q_{\mathrm{u}}(\omega, t) = \omega\frac{W(t)}{P_{\mathrm{loss}}(t)} \tag{7.15}$$

where $W(t)$ and $P_{\mathrm{loss}}(t)$ are the instantaneous energy stored inside the cavity's volume V and power dissipated and radiated at resonance, respectively, and ω is the resonance frequency (yet to be defined unambiguously). At resonance, the sum total energy can be stored in either the electric or magnetic field. Thus, one obtains

$$W = \frac{1}{2}\iiint_V \mathbf{D}(\mathbf{r},t)\cdot\mathbf{E}(\mathbf{r},t)dV = \frac{1}{2}\iiint_V \varepsilon_{\mathrm{d}}\,|\,\mathbf{E}(\mathbf{r},t)\,|^{\,2}dV = \frac{1}{2}\varepsilon_{\mathrm{d}}e^{-2\omega_0'' t}\iiint_V |\,\mathbf{E}(\mathbf{r})\,|^{\,2}dV \tag{7.16}$$

since the electric field is expressed as

$$\mathbf{E}(\mathbf{r},t) = \mathbf{E}_0(\mathbf{r})e^{j\omega_0 t} = \mathbf{E}_0(\mathbf{r})e^{-\omega_0'' t}e^{j\omega_0' t} \tag{7.17}$$

From the principle of energy conservation, the power lost equals the rate at which stored energy is dissipated as heat (i.e., ohmic losses) and radiated. Therefore,

$$P_{\mathrm{loss}} = -\frac{dW}{dt} = \varepsilon_{\mathrm{d}}\omega_0'' e^{-2\omega_0'' t}\iiint_V |\,\mathbf{E}(\mathbf{r})\,|^{\,2}dV \tag{7.18}$$

Combining (7.15)-(7.18), it follows that the time dependency is lost when determining the unloaded quality factor, as

$$Q_{\mathrm{u}}(\omega) = \frac{\omega}{2\omega_0''} \tag{7.19}$$

Now, the following question arises: at what angular frequency ω should the unloaded quality factor be evaluated? With low loss resonant structures this is a trivial question, since $|\omega_0| \simeq \omega_0'$. However, with lossy resonant structures, it is important to make the correct distinction. In the case where the driving source effectively compensates for all losses, the undamped angular resonance frequency is of interest and it is only meaningful to calculate the unloaded quality factor at ω_0. Alternatively, for the case where there is no driving source, the damped angular resonance frequency is of interest and the unloaded quality factor should only be evaluated at ω_0'. This follows directly from (7.17), where the oscillatory term is at ω_0'. A more detailed discussion of this point will be given later, where an equivalent circuit model is presented, and it will be shown how $Q_{\mathrm{u}}(\omega_0')$ can be calculated from $Q_{\mathrm{u}}(|\omega_0|)$.

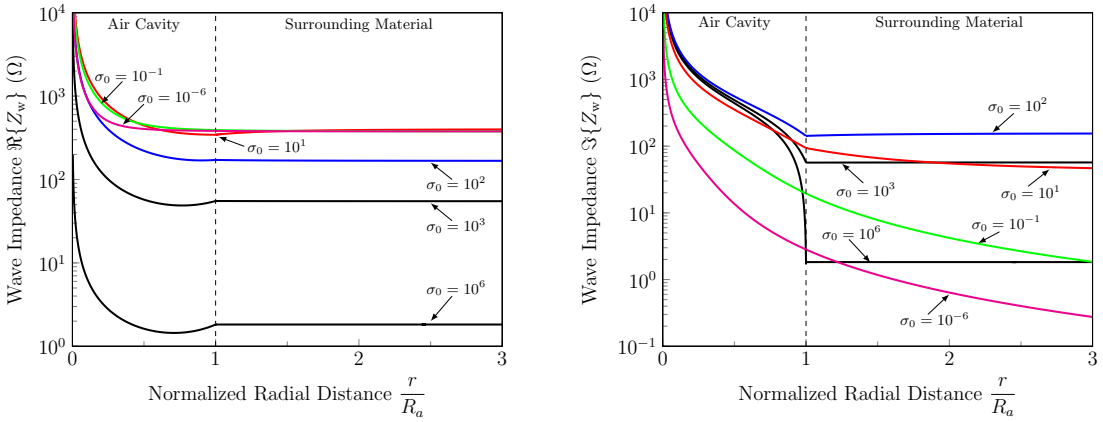


Figure 7.1: Wave impedance for the fundamental TM_{011} mode for an air-filled spherical cavity having a 150 µm radius with various wall conductivities: (a) real part and (b) imaginary part.

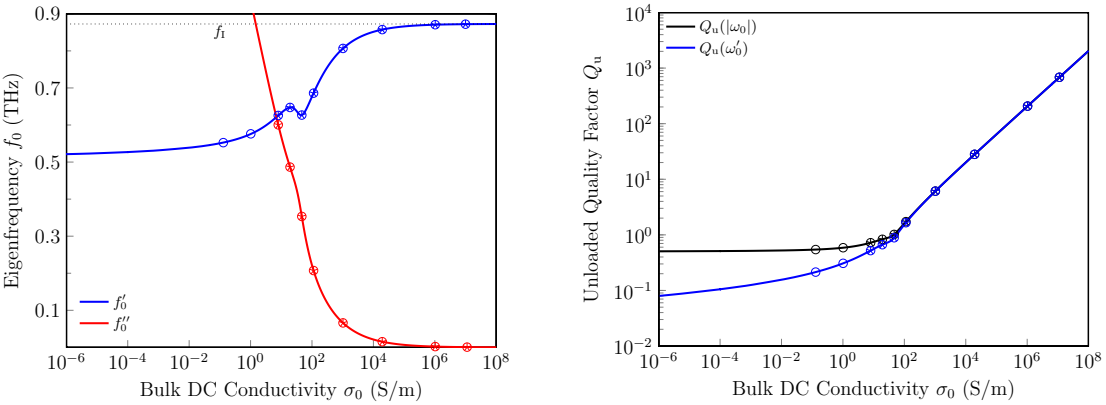


Figure 7.2: (a) Eigenfrequency for the fundamental TM_{011} mode for an air-filled spherical cavity having a 150 µm radius and (b) associated unloaded quality factors. Solid lines: Exact analytical results. Discrete symbols: numerical results obtained from commercial full-wave solvers (circles: HFSS^{TM} and stars: COMSOL).

7.3 Modeling Approaches Results and Discussion

7.3.1 Exact Analytical Results

The previous analysis is general and describes the behavior of a spherical cavity resonator made of arbitrary materials (both the filler and wall). Using (7.12), the wave impedance against radial distance for various intrinsic values of bulk DC wall conductivity with an air-filled spherical cavity having an arbitrary radius $R_a = 150$ µm is shown in Fig. 7.1.

Also, (7.13) can be used as a suitable benchmark reference standard to assess the performance of eigenmode solvers intended for arbitrary 3D structures. For the same resonator structure, the complex eigenfrequency $f_0 = f_0' + jf_0''$ and associated unloaded quality factors for intrinsic values of bulk DC wall conductivity of $10^{-6} \leqslant \sigma_0$ (S/m) $\leqslant 10^{8}$, which effectively represents the transformation of the wall from being a PEC to free space, are shown in Fig. 7.2. Moreover, the modal field

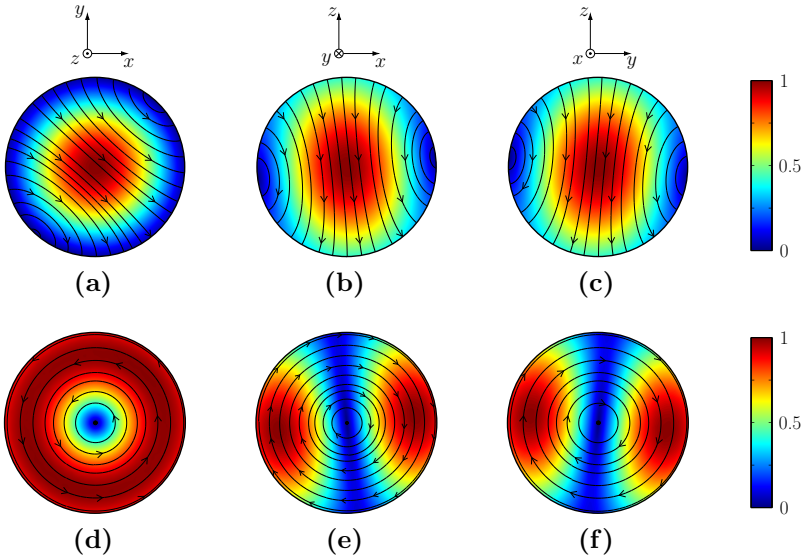


Figure 7.3: Normalized field patterns for the TM_{011} mode for an air-filled spherical cavity having a 150 µm radius in the ideal case where $\sigma_0 \to \infty$. Electric field in (a) x-y, (b) x-z and (c) y-z plane. Magnetic field in (d) x-y, (e) x-z and (f) y-z plane.

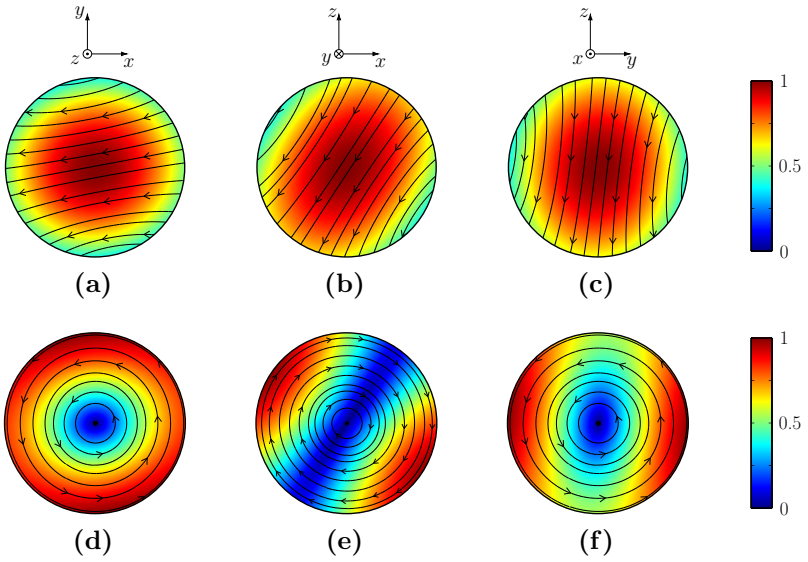


Figure 7.4: Normalized field patterns for the TM_{011} mode for an air-filled spherical cavity having a 150 µm radius with $\sigma_0 = 100$ S/m. Electric field in (a) x-y, (b) x-z and (c) y-z plane. Magnetic field in (d) x-y, (e) x-z and (f) y-z plane.

distributions for a PEC-walled cavity and a cavity with arbitrary wall conductivity $\sigma_0 = 100$ S/m are shown in Figs. 7.3 and 7.4, respectively.

It is worth mentioning that, with resonance frequencies below the wall material's relaxation frequency $f_\tau = \dfrac{1}{2\pi\tau}$, where τ is the phenomenological scattering relaxation time, Drude relaxation effects can be ignored[9, 15]. Indeed the resonance frequencies for the air-filled cavity being considered here (having $R_a = 150$ µm and $f_I = 0.873$ THz) has $|f_0| < f_\tau$, as seen in Table 7.1 for three arbitrary conductors.

Table 7.1: Relaxation frequencies for various conducting wall materials at room temperature [16, 17] with the exact results.

Conductor	σ_0 (S/m)	τ (ps)	f_τ (THz)	f_0 (THz)
gold	$4.1 \cdot 10^7$	27.135	5.87	0.872
ITO	$\sim 8 \cdot 10^5$	12.6	12.6	0.870
carbon	$\sim 10^3$	120	1.3	0.809

7.3.2 Analytical Plane-wave Approximation

In general, when simulating a structure having arbitrary materials, there are two approaches to defining its walls. The first one is to physically draw each material region as a 3D object and then assign its bulk material parameters. Alternatively, the 3D regions can be replaced by a surface boundary condition, where the appropriate material parameters are entered. A detailed study for low loss metal structures can be found in[9]. However, both of these approaches have weaknesses with low conductivity materials. For example, with the former approach, as wall conductivity decreases thicker walls are required to achieve a skin depth thickness. Therefore, the wall thickness is a limiting factor and it has been found that when the intrinsic bulk DC conductivity of the wall is $\lesssim 50$ (S/m), the eigenmode solver does not converge on a solution. On the other hand, when the wall conductivity is $\gtrsim 10^5$ (S/m), the computational resources and time required to mesh and solve inside the metal wall are impractical. As a result, this former approach can only be used within a relatively narrow conductivity range.

For this reason, surface boundary conditions can be employed, for many applications, as a more efficient modeling approach; in extreme cases this is the only approach available. For example, with HFSS™ (version 13) [18], there are three different boundary conditions available: Finite Conductivity Boundary (FCB), Layered Impedance Boundary (LIB) and Impedance Boundary (IB). With the first two, the user enters bulk material parameters (e.g., $mu_\mathrm{r} \rightarrow \mu_\mathrm{c}/\mu_0$, $\varepsilon_\mathrm{r} \rightarrow \varepsilon_{\mathrm{r}\infty}$, $\sigma \rightarrow \sigma_\mathrm{c}$, for the wall (similar to the solid object definition), whereas with IB the value of the complex surface impedance Z_s has to be entered (which must be known a priori). Similarly, with COMSOL (version 4.3a) [19], either the FCB, LIB or IB conditions can be met by the suitable manipulation of the following formulation

$$Z_\mathrm{s} = \sqrt{\frac{\mu_0\mu_\mathrm{r}}{\varepsilon_0\varepsilon_\mathrm{r} - j\dfrac{\sigma}{\omega}}} \tag{7.20}$$

With HFSS™ (with the exception of IB) and COMSOL, the boundary conditions rely purely on the wall's bulk material parameters; suggesting that an approximation model can be derived to accurately predict the results generated by the solvers. It has been found that this can be achieved using (7.10)-(7.11), by simply equating the wave impedance Z_w at the wall interface (i.e., at $r = R_a$) to the wall's intrinsic impedance $\eta_\mathrm{c} = \sqrt{\dfrac{j\omega\mu_0}{\sigma_0 + j\omega\varepsilon_0}} = Z_\mathrm{s} = R_\mathrm{s} + jX_\mathrm{s}$, using the Leontovich surface impedance boundary condition

$$\mathbf{E} \times \mathbf{u}_r \Big|_{r=R_a} = Z_\mathrm{s}\big(\mathbf{u}_r \times \mathbf{H}\big) \times \mathbf{u}_r \Big|_{r=R_a} \tag{7.21}$$

In general, the wave impedance at the interface at $r = R_a$ can be written as

$$Z_\mathrm{w}\Big|_{r=R_a} = \frac{E_\theta}{H_\phi}\Big|_{r=R_a} = j\eta_\mathrm{c}\left[\frac{h_{n-1}^{(2)}(k_\mathrm{c}R_a)}{h_n^{(2)}(k_\mathrm{c}R_a)} - \frac{n}{k_\mathrm{c}R_a}\right] \tag{7.22}$$

and thus, with the relationship $\lim_{x\to\infty} h_n^{(2)} = j^{n+1}\frac{e^{-jx}}{x}$, the following analytical plane-wave approximation (where $|k_c R_a| \to \infty$), for (7.13) and (7.22), is proposed and it will be shown that this model accurately predicts the results for both commercial eigenmode solvers. From (7.13), the characteristic equation for the plane-wave approximation for the TM_{011} mode is given by

$$\eta_d \left[\frac{j_0(k_d R_a)}{j_1(k_d R_a)} - \frac{1}{k_d R_a} \right] - j\eta_c = 0 \tag{7.23}$$

Similarly, from (7.22), the wave impedance at the boundary for the plane-wave approximation for the TM_{011} mode has the following asymptotic behaviour

$$\lim_{|k_c R_a|\to\infty} \left\{ Z_w \Big|_{r=R_a} \right\} = j\eta_c \lim_{|k_c R_a|\to\infty} \left\{ \frac{h_0^{(2)}(k_c R_a)}{h_1^{(2)}(k_c R_a)} - \frac{1}{k_c R_a} \right\} = \eta_c \tag{7.24}$$

7.3.3 Plane-wave Approximation and FCB/LIB Results

With the FCB condition in HFSS™, as explained in the software Technical Notes, the displacement current term is neglected; thus, $Z_s = R_0(1+j)$, with surface resistance $R_0 = \sqrt{\frac{\omega\mu_0}{2\sigma_0}}$[9, 15]. While, with COMSOL, this model is obtained by setting $\mu_r = 1$, $\varepsilon_r = 0$ and $\sigma = \sigma_0$. This approach is only valid for "good electrical conductors" and it will be seen that this has no physical meaning when conducting wall losses are high. This gross assumption is, however, the most widely used with perturbation methods [20]. Nevertheless, this classical skin-effect model that excludes the displacement current term will be used to determine eigenfrequencies as a means to validate our analytical plane-wave approximation model. To this end, Figs. 7.5 and 7.6 show the eigenfrequencies and associated percentage error, respectively, against intrinsic wall conductivity. Although the results for low conductivity values lack physical meaning, this approach highlights the validity of our approximated model.

Next, the classical skin-effect model that includes both conduction and displacement current terms is considered; thus, $R_s \neq X_s$. With HFSS™ this is obtained using the LIB condition, whereas with COMSOL this is the default boundary by setting $\mu_r = 1$, $\varepsilon_r = 1$ and $\sigma = \sigma_0$. As seen in Fig. 7.7, this approach results in a cut-off value for the conductivity σ_{0c}, below which the TM_{011} mode is not predicted to be supported. However, this is an artifact of the analytical plane-wave approximation and surface impedance models used. Therefore, this approach cannot generate any eigenfrequencies when the wall conductivity is lower that the cut-off value. The corresponding percentage errors for this approach is shown in Fig. 7.8.

The unloaded quality factors at the driven and undriven resonance frequencies are shown in Fig. 7.9. It is worth noting that the eigenmode solver in COMSOL can only report values of $Q_u(\omega_0') = \frac{\omega_0'}{2\omega_0''} > 0.5$, which corresponds to $Q_u(|\omega_0|) = \frac{|\omega_0|}{2\omega_0''} > \frac{1}{\sqrt{2}}$, regardless of the modeling approach.

The reason for the weaknesses when using both FCB and LIB conditions is that the wave impedance inherently depends on the geometry (since Z_w is a function of R_a) and, therefore, their accuracy is limited by this; geometry is not taken into account by the input parameters μ_r, ε_r and σ. For example, when observing the wave impedance along the radial distance, as shown in Fig. 7.1, it is clear that only for sufficiently high wall conductivities is the wave impedance constant within the wall and, hence, can be approximated by its intrinsic impedance.

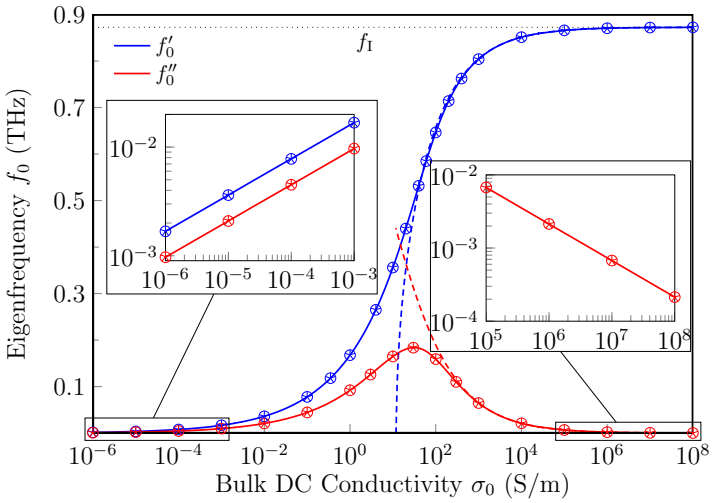


Figure 7.5: Resonant frequency for the fundamental TM_{011} mode for an air-filled spherical cavity having a 150 µm radius using $Z_s = R_0(1 + j)$. Solid lines: Analytical results. Discrete symbols: Numerical results obtained with a full-wave solver (circles: HFSS™ and stars: COMSOL). The results from perturbation method are also shown with dashed lines.

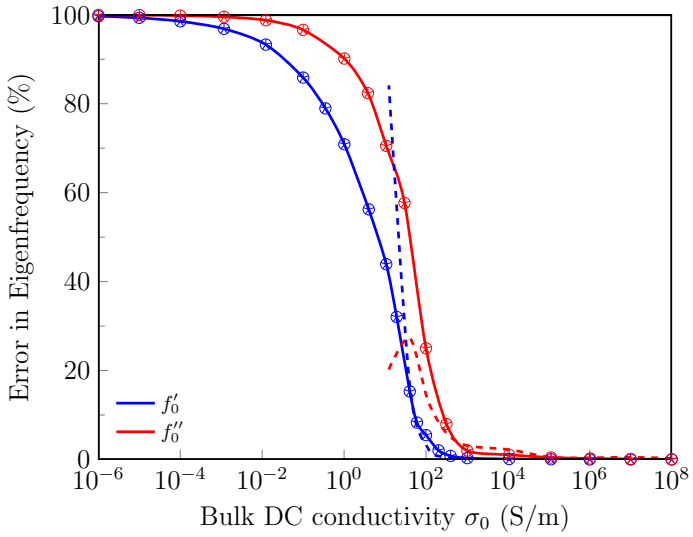


Figure 7.6: Percentage errors for eigenfrequencies using the FCB condition (circles: HFSS™ and stars: COMSOL). The error from perturbation method is also shown with dashed lines.

7.3.4 Exact Analytical and IB Results

With HFSS™, the IB condition allows the user to enter the complex surface impedance. This generally gives very accurate results, as shown in Fig. 7.2. It is interesting to see that f_0' does not decrease monotonically with decreasing intrinsic conductivity; there is a dip seen in Fig. 7.2(a) that corresponds to the peak seen in Fig. 7.1(b) in the imaginary part or the wave impedance at ~ 46 S/m. Moreover, $|f_0|$ can exceed f_I in a very low quality factor environment, with a physical interpretation that is best observed in the time domain for such a highly damped condition.

Unfortunately, with HFSS™, the IB condition fails with very low intrinsic conductivity values of $\lesssim 0.1$ S/m, where the solver cannot converge onto any solution. Similarly, with COMSOL, the

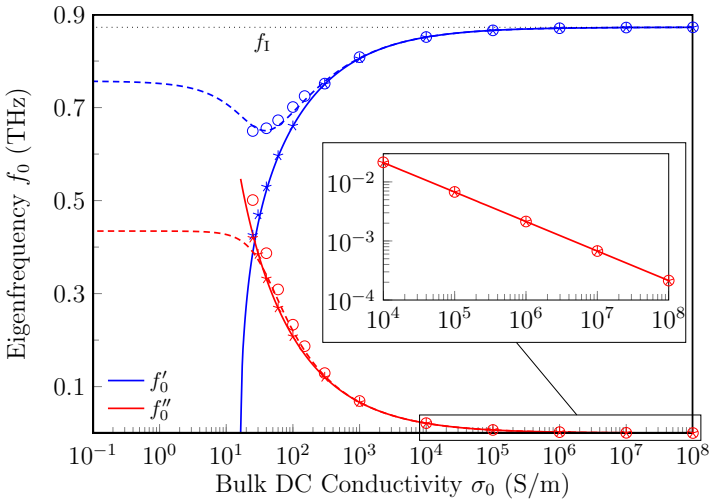


Figure 7.7: Resonant frequency for the fundamental TM_{011} mode for an air-filled spherical cavity having a 150 µm radius using $Z_s = R_s + jX_s$. Solid lines: Analytical results. Discrete symbols: Numerical results obtained with a full-wave solver (circles: HFSS™ and stars: COMSOL). The results from perturbation method are also shown with dashed lines.

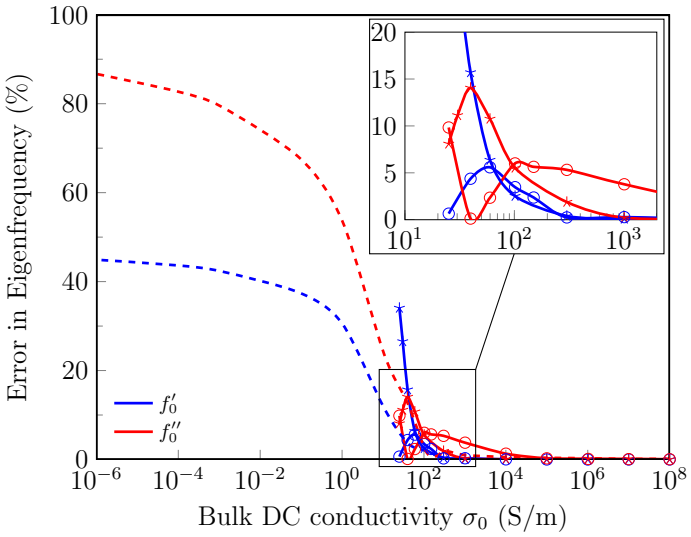


Figure 7.8: Percentage errors for eigenfrequencies using the LIB condition (circles: HFSS™ and stars: COMSOL). The error from perturbation method is also shown with dashed lines.

user has to take into account (7.20) and define the material parameters so that (7.20) has a value equal to Z_w (by forcing $\mu_r \to Z_w^2/\mu_0$, $\varepsilon_r \to \varepsilon_0$ and $\sigma \to 0$). Again, the solver cannot converge when $Q_u(\omega_0') \leqslant 0.5$.

Moreover, with both HFSS™ and COMSOL solvers, a priori knowledge of the resonance frequency and the wave impedance at the boundary (i.e., the exact analytic expression given by (7.22)) is required, otherwise it will result in a total failure to predict the eigenfrequencies for arbitrary 3D structures having lossy metal walls.

For completeness, results using the perturbation method are included and obtained using the following formulation [21]

$$X_s(|\omega_0|) - 2\Gamma\,(\omega_I - |\omega_0|) = 0 \tag{7.25}$$

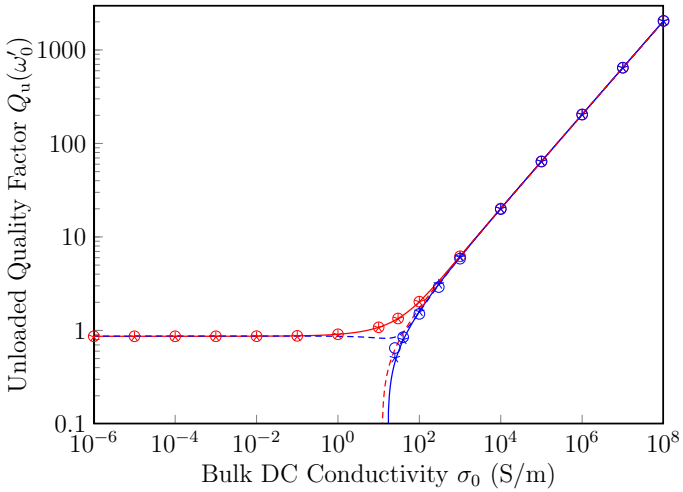


Figure 7.9: Unloaded quality factor $Q_u(\omega_0')$ for the fundamental TM_{011} mode for an air-filled spherical cavity having a 150 µm radiususing $Z_s = R_0(1+j)$ (red) and $Z_s = R_s + jX_s$ (blue), respectively. Solid lines: Analytical results. Discrete symbols: Numerical results obtained with a full-wave solver (circles: HFSS™ and stars: COMSOL). The results from perturbation method are also shown with dashed lines.

$$\Gamma = \mu_0 \frac{\iiint_V \mathbf{H} \cdot \mathbf{H}^* dV}{\iint_S \mathbf{H}_t \cdot \mathbf{H}_t^* dS} \tag{7.26}$$

$$Q_u(|\omega_0|) \simeq \frac{|\omega_0|\Gamma}{R_s(|\omega_0|)} \tag{7.27}$$

where suffix "t" represents the field components tangential to the surface of the wall and S the inner surface area of the wall.

When comparing the results from all the various approaches, it is clear that they all approximate to the exact analytical solution in the low loss region (i.e., "good electrical conductor"' behavior). However, as the wall losses increase, they gradually diverge.

7.4 Equivalent Circuit Modeling

For a more meaningful insight, it may be convenient to interpret a cavity resonator with a lumped-element *RLC* equivalent circuit model. This is particularly useful for characterizing resonators without the need for performing electromagnetic calculations.

The cavity resonator can be regarded as an elementary resonant circuit, as shown in Fig. 7.10(a), where the inductor and capacitor depend on the cavity filler (i.e., μ_d, ε_d), cavity size (e.g., internal cavity volume $V = 4\pi R_a^3/3$) and wall material (i.e., μ_w, ε_w, σ_w). All these parameters implicitly affect the complex resonant frequency ω_0, as [22]

$$\omega_0 = \frac{1}{\sqrt{L_{eff} C_{eff}}} \tag{7.28}$$

$$L_{eff} = \mu_d V k_d^2 \tag{7.29}$$

$$C_{eff} = \frac{\varepsilon_d}{V k_d^4} \tag{7.30}$$

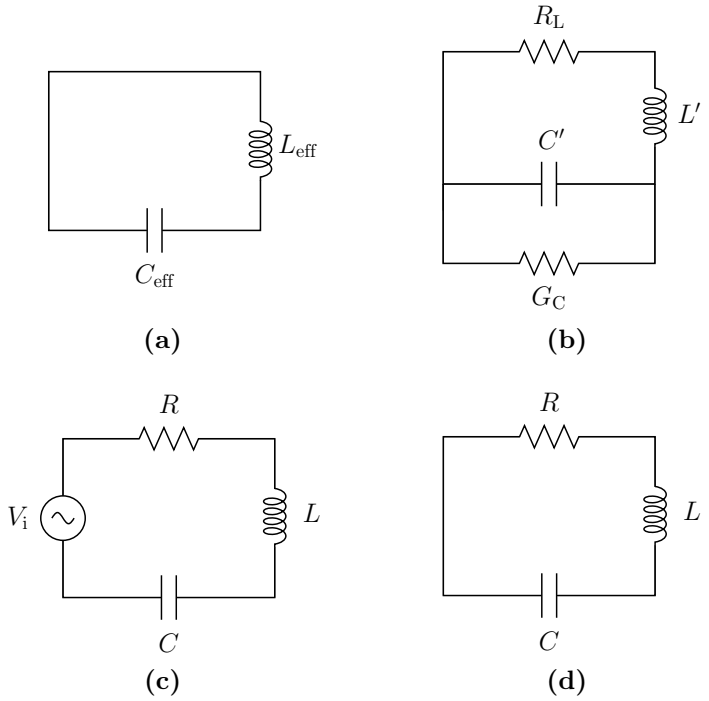


Figure 7.10: Lumped element RLC equivalent circuit models for the fundamental TM_{011} mode. (a) Elementary resonant circuit with complex effective inductance and capacitance, (b) resonant circuit after replacing the complex effective components with equivalent real components, (c) driven RLC circuit and (d) undriven RLC circuit.

where, for an air-filled spherical cavity, one obtains

$$L' = \mu_0 V \frac{\left(\omega_0'^2 - \omega_0''^2\right)}{c^2} \tag{7.31}$$

$$L'' = \mu_0 V \frac{2\omega_0'\omega_0''}{c^2} \tag{7.32}$$

$$C' = \frac{\varepsilon_0}{V} \frac{c^4}{|\omega_0|^8} \left[\left(\omega_0'^2 - \omega_0''^2\right)^2 - \left(2\omega_0'\omega_0''\right)^2 \right] \tag{7.33}$$

$$C'' = \frac{\varepsilon_0}{V} \frac{4c^4\omega_0'\omega_0''(\omega_0''^2 - \omega_0'^2)}{|\omega_0|^8} \tag{7.34}$$

As can be seen that all parameters depend explicitly on both the real and imaginary parts of the complex eigenfrequency and implicitly on the bulk DC conductivity of the wall (since it also affects the complex eigenfrequency).

Although the resonant circuit in Fig. 7.10(a) fully describes the behaviour of the cavity at resonance it does not offer any meaningful physical insight, because of the complex nature of the effective inductance and capacitance. Purely real components can be employed, as shown in Fig. 7.10(b), having values derived using the following transformations

$$Z_{\text{series}} = j|\omega_0|L_{\text{ef}} = R_{\text{L}} + j|\omega_0|L' \tag{7.35}$$

$$Y_{\text{shunt}} = j|\omega_0|C_{\text{ef}} = G_{\text{C}} + j|\omega_0|C' \tag{7.36}$$

where $R_{\text{L}} = -|\omega_0|L''$ and $G_{\text{C}} = -|\omega_0|C''$. Usually, it is more traditional to represent resonators as equivalent RLC networks, as shown in Fig. 7.10(c), where the driving source automatically

compensates for the combined losses (represented solely by R) and, thus, the resonance frequency is purely real in this lossless scenario. Moreover, with driven resonant circuits, the resistance R does not contribute to the detuning of the resonance frequency. This topology is widely used when characterizing tuned circuits, by measuring $|\omega_0|$ and $Q_{\mathrm{u}} = \dfrac{|\omega_0|L}{R}$ in the frequency domain. As a result, using (7.21) with $\omega = |\omega_0|$ the equivalent circuit components, all having positive values, can be expressed as

$$L = |L_{\mathrm{eff}}| = \frac{\mu_0 V |\omega_0|^2}{c^2} \tag{7.37}$$

$$C = |C_{\mathrm{eff}}| = \frac{\varepsilon_0 c^4}{V|\omega_0|^4} \tag{7.38}$$

$$R = 2\omega_0'' L = \frac{2V\omega_0''|\omega_0|^2}{\varepsilon_0 c^4} \tag{7.39}$$

While Fig. 7.10(c) is practical, it does not provide information about the real and imaginary parts of the complex eigenfrequency. By removing the sinusoidal driving source and replacing it with a Dirac impulse generator, time-domain measurements would reveal the complex eigenfrequency as defined in (7.19), since the resonator naturally oscillates at its damped frequency ω_0' with an exponential decay that is governed by the imaginary part of its eigenvalue ω_0''. Alternatively, if the undamped resonance frequency and associated unloaded quality factor $Q_{\mathrm{u}}(|\omega_0|)$ are known, one can calculate the complex resonant frequency and associated quality factor at the damped resonant frequency as follows

$$\left.\begin{aligned} \omega_0'' &= \frac{|\omega_0|}{2Q_{\mathrm{u}}(|\omega_0|)} \\ \omega_0' &= \sqrt{|\omega_0|^2 - \omega_0''^2} \end{aligned}\right\} \Rightarrow Q_{\mathrm{u}}(\omega_0') = \frac{\omega_0'}{2\omega_0''} \tag{7.40}$$

After some algebraic manipulations, the following can be obtained that interrelates both unloaded quality factors

$$Q_{\mathrm{u}}(\omega_0') = \sqrt{Q_{\mathrm{u}}^2(|\omega_0|) - \left(\frac{1}{2}\right)^2} \tag{7.41}$$

7.5 Conclusion

From first principles, the electromagnetic analysis of lossy metal-walled spherical cavity resonators has been given for the first time. Exact analytical results, acting as a benchmark reference standard, are used to stress test two industry-standard commercial eigenmode solvers (by the introduction of arbitrary lossy metal walls). Unlike perturbation techniques, appropriate only for low loss scenarios, there are no inherent loss limitations in our analysis. When the wall transforms from being a PEC to free space, it is found that the eigenmode solvers with both software packages increasingly fail; this has profound implications on their usefulness for the modeling of arbitrary 3D lossy structures having even the simplest of geometries. With both software packages, all possible modeling strategies have been investigated and their associated limitations identified.

In addition, a plane-wave approximation model has been proposed that accurately predicts the numerical simulation results for the FCB and LIB conditions; this provides an analytical means for accurately quantifying the weakness of the numerical eigenmode solvers. It is also found that, when using the accurate IB condition, a priori knowledge of the resonance frequency and the wave impedance at the boundary is required, otherwise it will result in a total failure to predict the eigenfrequencies for arbitrary 3D structures having lossy metal walls.

For completeness, a generic lumped-element RLC equivalent circuit model has been given that exactly describes the cavity behavior as its wall transforms from being a PEC to free space. In addition, the long-standing ambiguity associated with defining unloaded quality factors with lossy resonators has been resolved. Together, a deeper insight into the behavior of lossy spherical cavity resonators and commercial eigenmode solvers is given for the first time.

References

[1] W. W. Hansen, "A type of electrical resonator", *J. Appl. Phys.*, vol. 9, no. 10, pp. 654-663, Oct. 1938

[2] W. L. Barrow, W. W. Mieher, "Natural oscillations of electrical cavity resonators", *IRE Proc.*, vol. 28, no. 4, pp. 184-191, Apr. 1940

[3] S. Gallagher, W. J. Gallagher, "The spherical resonator", *IEEE Trans. Nucl. Sci.*, vol. NS-32, no. 5, 2980-2982, Oct. 1985

[4] N. Nepal, Y. K. Kim, Y. S. Bae, I. S. Ko, M. H. Cho, W. Namkung, "Design study on standing-wave linear accelerator", *IEEE Proc. PAC*, vol. 4, pp. 2802-2804, Jun. 2001

[5] G. Shvets, "Optical polarizer/isolator based on a rectangular waveguide with helical grooves", *Appl. Phys. Lett.*, vol. 89, no. 14, p. 141127, Oct. 2006

[6] S. A. Maier "Plasmonics: Fundamentals and Applications", *Springer*, 2007

[7] S. Papantonis, S. Lucyszyn and E. Shamonina, "Dispersion effects in Fakir's bed of nails metamaterial waveguides", *J. Appl. Phys.*, vol. 115, no. 5, p. 054903, Feb. 2014

[8] J. Y. Choi and S. Lucyszyn, "HFSS™ modelling anomalies with electrically thin-walled metal-pipe rectangular waveguide simulations", *10th IEEE High Freq. Postgrad. Student Colloq.*, pp. 95-98, Sep. 2005

[9] E. Episkopou, S. Papantonis, W. J. Otter and S. Lucyszyn, "Defining material parameters in commercial EM solvers for arbitrary metal-based THz structures", *IEEE Trans. Terahertz Sci. Technol.*, vol. 2, no. 4, pp. 513-524, Sep. 2012

[10] J. C. Slater, "Microwave electronics", *Rev. Mod. Phys.*, vol. 18, vo. 4, pp. 441-512, Oct. 1946

[11] A. Hadidi and M. Hamid, "Analysis of a cylindrical cavity resonator with absorbing wall", *Int. J. Electronics*, vol. 63, no. 3, pp. 435-442, Mar. 1987

[12] M. Gastine, L. Courtois and J. L. Dormain, "Electromagnetic resonances of free dielectric spheres", *IEEE Trans. Microw. Theory Techn.*, vol. 15, no. 12, pp. 694-700, Dec. 1967

[13] R. E. Collin, "Field theory of guided waves"', 2nd ed., *IEEE Press*, 1991

[14] C. A. Balanis, "Advanced engineering electromagnetics"', *Wiley*, 1989

[15] S. Lucyszyn and Y. Zhou "Engineering approach to modelling frequency dispersion within normal metals at room temperature for THz applications", *PIER*, vol. 101, pp. 257-275, 2010

[16] Y. Zhou and S. Lucyszyn, "Modelling of reconfigurable terahertz integrated architecture (RETINA) SIW structures", *PIER*, vol. 105, pp. 71-92, Jun. 2010

[17] J. Jiang, R. Saito, A. Grueneis, G. Dresselhaus and M. S. Dresselhaus, "Electron-photon interaction and relaxation time in graphite", *Chem. Phys. Lett.*, vol. 392, pp. 383-389, 2004

[18] http://www.ansys.com/products/hf/hfss/

[19] http://www.comsol.com/

[20] D. M. Pozar, "Microwave Engineering", 2nd ed., *Wiley*, 1998

[21] Y. Zhou and S. Lucyszyn, "HFSS™ modelling anomalies with THz metal-pipe rectangular waveguide structures at room temperature", *PIERS*, vol. 5, no. 3, pp. 201-211, 2009

[22] C. G. Montgomery, R. H. Dicke, E. M. Purcell "Principles of microwave circuits", ch. 7, *McGraw-Hill*, 1948

Chapter 8

Conclusions and Future Work

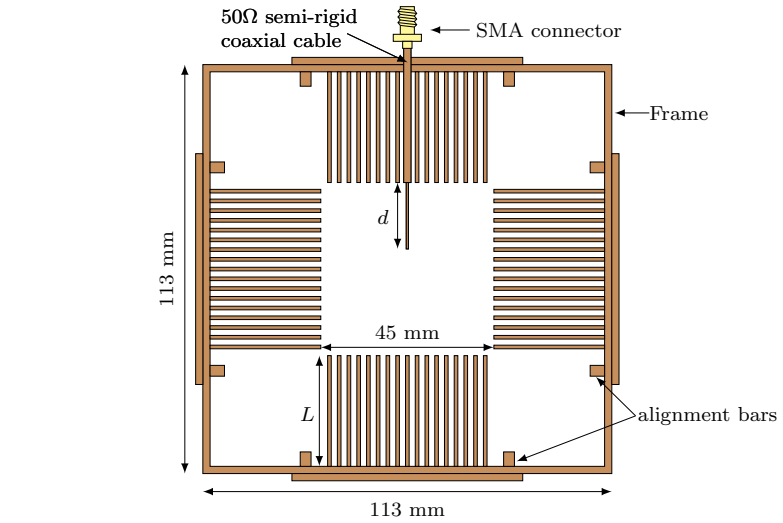
In this thesis, the implementation of passive electromagnetic components with the use of the "Fakir's bed of nails" metamaterial have been studied in detail by means of analytical techniques, full-wave simulations and experimental verification. Where appropriate, existing analytical models have been expanded to describe the behaviour of more complicated practical devices. Furthermore, potentially new applications have been investigated with emphasis given on exploring the advantages offered by reconfigurable devices.

Specifically, the propagation characteristics in parallel-plate waveguides with both plates being realized by the Fakir's bed of nails have been studied thoroughly. Also, the response at optical frequencies of an infinite chain of nanopins (aligned along their axis) has been explained in terms of coupled surface plasmon polaritons. This structure is a modification of the "Fakir's bed of nails"; the pins are aligned along their axis to form a 1D periodic structure. Additionally, the implementation of reconfigurable waveguide components using the "Fakir's bed of nails" has been demonstrated with the realization of tunable waveguide iris filters. Based on this approach, a novel method to verify waveguide measuring systems is proposed employing a single reconfigurable device. Finally, considering the importance of full-wave simulation software, particularly for studying metamaterials, a stress-testing analysis of commercial solvers is undertaken with lossy spherical cavity resonators acting as benchmark reference structures. This study can be of great interest when coupled lossy structures are modeled.

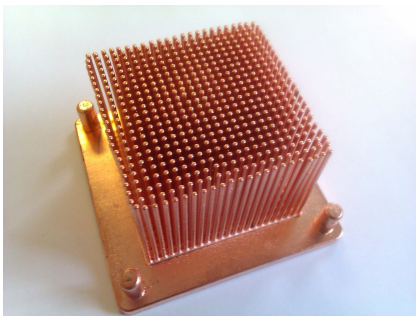
The starting point for deriving the analytical model of components formed by the bed of nails has already been presented in Chapters 2 and 3. These results can be expanded to cover other devices as well (i.e., rectangular waveguides and/or cavity resonators). Moreover, the power losses with such metamaterial structures can be investigated and incorporated in the analytical model. This will enable a comparison with conventional components in terms of power losses and hence the following hypothesis can be investigated: A new ground plane (at the top of the pins) with less power losses can be engineered since the original surface area of the ground plane, as shown in Fig. 2.1, is reduced to that which includes the total surface area of the pins. Thus the overall surface power density is reduced and hence the power dissipated in the metal is reduced.

Next, prototype devices realized by the Fakir's bed of nails can be manufactured so that their behaviour is experimentally validated. Prototypes can be manufactured at different frequency ranges (e.g., microwaves and/or terahertz) employing various techniques such as hot embossing or clean-room microfabrication processes.

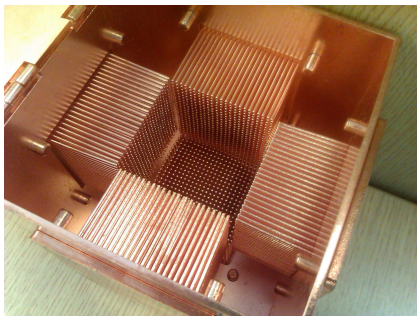
For example, a rectangular cavity resonator with its walls replaced by the Fakir's bed of nails (resembling an "iron maiden" cavity) has been fabricated, as shown in Fig. 8.1. The resonator is very similar to the waveguide presented in Chapter 3. The resonator has internal spatial dimensions $45 \times 45 \times 45$ mm^3 which correspond to an ideal resonant frequency of approximately 4.7 GHz and



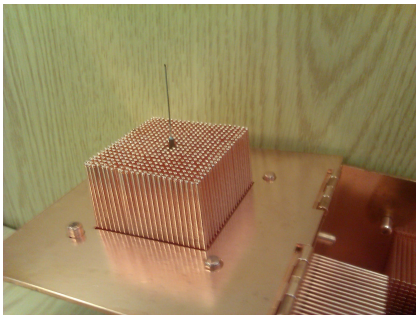
(a)



(b)



(c)



(d)



(e)

Figure 8.1: Fabricated cavity resonator realized by the Fakir's bed of nails. (a) Side view illustration, (b) a single cavity wall, (c) top view of the assembled resonator, (d) feeding probe of the cavity and (e) fully assembled resonator.

the length of the pins is 32 mm, corresponding to $\lambda/2$ at 4.6875 GHz. Furthermore, the periodicity of the lattice is 2 mm and the diameter of the pins is $2r_0 = 1$ mm. However, the resonator needs to be properly assembled in order to achieve good electrical conductivity at the interconnection points. For example, the pin walls can be soldered on the frame but because the pin consist of a dielectric material plated with copper it is quite likely to melt the dielectric underneath the copper. Thus, the structure can collapse and lose its shape. On top of this, the calibration is not straightforward as the highly artificial environment within the cavity dictates that the most appropriate reference plane for the measurements is at top bed of nails/air interface, as shown in Fig. 8.1(a). For this

reason, specially designed semi-rigid coax calibration standards were manufactured. It should be noticed that the skin depth at 4.7 GHz is approximately 0.96 µm and the minimum thickness of the electroformed copper that has been deposited is 50 µm. Practically, this means that copper can be treated as bulk material since it is much thicker than 5 skin depths.

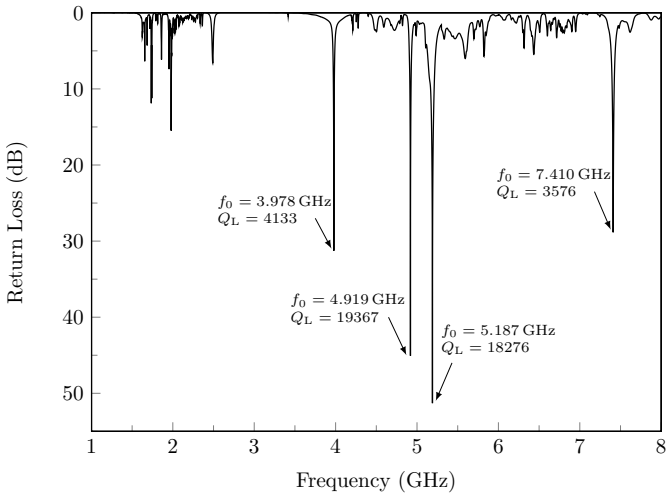


Figure 8.2: Measured return loss for the iron maiden cavity shown in Fig. 8.1.

Preliminary measurements of the cavity have shown that the structure is capable of producing sharp resonances, as shown in Fig. 8.2. As can be seen, there are several resonances corresponding to different modes. However, the mode identification is not straightforward and further analysis is required in order to characterize these modes. This is because, as explained previously, the Fakir's bed of nails has extraordinary properties only for TM polarization and hence, the mode patterns in such a cavity are more complicated than with conventional metal-walled cavity resonators. Additionally, the feeding probe perturbs the fields within the cavity and thus, the end modes are a mixture of multiple modes.

The loaded quality-factor Q_L can be calculated using the well-known expression $Q_L = \dfrac{f_0}{\Delta f}$, where Δf corresponds to the half power bandwidth (i.e., -3dB criterion). The unloaded Q_u-factor can then be calculated using QZERO software [1]and at 5.187 GHz is equal to 19613. For comparison, it should be mentioned that the calculated loaded and unloaded quality factor for a classical rectangular cavity resonator having identical internal spatial dimensions is 14975 and 15565, respectively which suggests that the "iron maiden" cavity has a much higher quality factor. However, the results are not stable nor reproducible and hence further investigations are required. It should be underlined that good electrical (conducting) connection between the different parts of the cavity is required and that physical contact is not enough to produce accurate results. Another parameter that highly affects the performance is the positioning of the walls. The behaviour of the cavity seems to be sensitive to small variations in the position of the walls. For example, the distance between the pins of adjacent walls has a major impact on the performance of the device. For this reason high precision micrometers need to be attached to the walls to control their position.

Following the results of Chapter 4, coupling in 2D and even 3D arrays of nanopins or other structures can be studied analytically or numerically or experimentally. This will also reveal potentially new applications to the realization of metasurfaces and their use for imaging/sensing devices.

Furthermore, based on the findings of Chapter 5, an equivalent circuit model describing the performance of the components presented therein can be introduced. Various types of sensors can

be studied, as proposed in Chapter 5, including bio-applications with the use of microfluidics within pillars. Also, an automated control mechanism for positioning the pins can be investigated, with MEMS technology being a strong candidate.

Exploring further the novel approach presented in Chapter 6, single-component verification kits can be manufactured at high millimeter and terahertz frequencies, where currently are not any commercially available. This is an open challenge as existing manufacturing methods pose certain limitations on the minimum dimensions that can be reliably made.

Finally, from the study presented in Chapter 7, an equivalent circuit model could be derived to take into account the surface impedance of the cavity walls. This approach would eliminate the need for complicated electromagnetic analysis since the resonant behaviour of the cavity can be determined solely by the equivalent circuit model. Moreover, by expanding the results presented in this work, coupling with an array of lossy cavities resonators can be investigated. This may help to better understand coupling mechanisms in metamaterials and plasmonic nanostructures, where usually their constituents are resonant elements.

In general, the components investigated in this thesis from an electromagnetic perspective, can also be studied in terms of their thermal behaviour. Specifically, the holey metasurface introduced in Chapter 5, could be used for improved cooling in temperature sensitive systems, whereas the bed of nails structure could be used as an efficient heat sink.

References

[1] D. Kajfez, "Q factor measurements using MATLAB", *Artech House*, 2011